

GAS PHASE ION ENERGETIC STUDIES VIA  
PHOTOELECTRON IMAGING AND  
ENERGY RESOLVED MASS SPECTROMETRY

by

CARRIE JO MICHELLE PRUITT

DANIEL J. GOEBBERT, COMMITTEE CHAIR

DAVID A. DIXON

SILAS C. BLACKSTOCK

MARTIN G. BAKKER

NATHAN I. HAMMER

A DISSERTATION

Submitted in partial fulfillment of the requirements  
for the degree of Doctor of Philosophy  
in the Department of Chemistry  
in the Graduate School of  
The University of Alabama

TUSCALOOSA, ALABAMA

2015

Copyright Carrie Jo Michelle Pruitt 2015  
ALL RIGHTS RESERVED

## ABSTRACT

Nitro containing compounds are well known energetic materials widely used in explosives. The shock sensitivity of nitro containing explosives has been linked to energetic properties such as bond dissociation energies, heats of formations, and molecular electronegativities. Measuring the energetic properties of nitro containing compounds can aide in the development and deployment of these materials, as well as influence practices in safe handling and use. The primary focus of this dissertation is investigating the energetic properties of nitro containing molecules using two experimental gas phase techniques.

The first part of this dissertation describes experiments carried out on a homebuilt negative ion photoelectron imaging spectrometer. A detailed description of the construction of this instrument is described in this dissertation. Two studies included in this dissertation highlight the utility of photoelectron imaging. The first photoelectron imaging study was conducted on the  $\text{CH}^-$  molecule. The results from this work allowed for the determination of fundamental properties such as the electron binding energy associated with two separate electronic transitions corresponding to electron detachment from the  $1\pi$  and  $3\sigma$  orbitals of  $\text{CH}^-$ . In addition to this, analysis of the photoelectron angular distributions revealed evidence for a temporary excited state of  $\text{CH}^-$  previously undetected.

The second photoelectron imaging study focused on nitromethane anion and the dimer, trimer, and hydrated monomer cluster anions. In this work, vertical detachment energies, estimated electron affinities, and solvation energies for each cluster anion were identified from the photoelectron spectra. Theoretical calculations were used to predict cluster structures with

calculated detachment energies in agreement with the experimental values. This work suggests the nitromethane clusters are formed by a single anion solvated by additional neutral molecules held together by O $\cdots$ C-H interactions.

The later part of this dissertation describes collision induced dissociation and energy resolved mass spectrometry experiments using a commercial triple quadrupole mass spectrometer. Fragmentation pathways in copper nitrate cluster anions, nitrotoluene radical anions, and deprotonated nitrophenols anions as well as dissociation energies were determined from these studies. Dissociation energies were determined from threshold measurements where the apparent cross section of a fragment was measured as a function of the collision cell voltage. The values obtained from these works can be used in the negative ion thermochemical cycle to provide information on corresponding neutral species and are potential useful in the field of energetic materials.

## DEDICATION

In memory of my father, Mike Pruitt.

To my wonderful mother, Mitzie Pruitt.

and Dr. Les Pesterfield and Alica Pesterfield

## LIST OF ABBREVIATIONS AND SYMBOLS

"	inch
%v/v	percent volume ratio
(g)	gas
(U)	unrestricted
*	excited state
°	degree
$^1\Delta$	singlet delta electronic state
2-D	two dimensional
$^2\Pi$	doublet pi electronic state
3-D	three dimensional
$^3\Sigma^-$	triplet sigma minus electronic state
$^4\Delta$	quartet delta electronic state
$^4\Sigma^-$	quartet sigma minus electronic state
a	proportionality constant
A	generic atom
Å	Angstrom
AB	generic molecule
AB <sup>-</sup>	generic molecular anion
AC	alternating current

ADE	adiabatic detachment energy
APCI	atmospheric pressure chemical ionization
aug-cc-pVDZ	augmented - correlation-consistent-polarized-valence only double zeta basis set
aug-cc-pVTZ	augmented- correlation-consistent-polarized-valence only triple zeta basis set
$A\varepsilon$	scaled electron kinetic energy
B	generic atom
$B$	proportionality constant
B3LYP	Becke-Lee-Yang-Parr exchange correlation functional
BASEX	basis set expansion program
BDE	bond dissociation energy
BNC	bayonet naval connector
CCD	charge coupled device
CCSD	coupled-cluster singles and doubles Method
CCSD(T)	coupled-cluster singles, doubles, and triples Method
CF	conflate
CID	collision induced dissociation
$\text{cm}^{-1}$	wavenumber
$D_0$	dissociation energy
DC	direct current
DFT	density functional theory
DP	diffusion pump
$dr$	difference in radial position
$E_0$	threshold energy

EA	electron affinity
eBE	electron binding energy
$E_{\text{cm}}$	center-of-mass energy
$E_i$	internal energy
eKE	electron kinetic energy
eKE <sub>cal</sub>	electron kinetic energy of calibration species
$E_{\text{lab}}$	collision energy in the lab frame
ERMS	energy resolved mass spectrometry
ESI	electrospray ionization
eV	electron volt
eV <sub>lab</sub>	collision energy in the lab frame in electron volts
$f$	fractional $p$ orbital character
$g_i$	fraction of ions with internal energy $E_i$
HPLC	high performance liquid chromatography
hr	hour
$h\nu$	photon energy
HV	high voltage
Hz	hertz
$I(\theta)$	intensity as a function of theta
IEEE	Institute of Electrical and Electronics Engineers
K	temperature in Kelvin
keV	kiloelectron volt
KTP	potassium titanyl phosphate - KTiOPO <sub>4</sub>

kV	kilovolt
kΩ	kiloohm
l	liter
<i>l</i>	atomic angular momentum quantum number
L1	electrostatic lens set 1
L2	electrostatic lens set 2
L3	electrostatic lens set 3
L4	electrostatic lens 4
<i>m</i>	mass of the target gas
M	mass of the precursor ion
m/z	mass-to-charge ratio
m <sup>3</sup>	cubic meter
m <sub>1</sub> /z	mass to charge ratio for molecule 1
m <sub>2</sub> /z	mass to charge ratio for molecule 2
mA	microamps
MCP	microchannel plate
MHz	megahertz
min	minute
mJ	millijoule
mL	milliliter
mM	millimolar
mm	millimeter
μL	microliter

$\mu$ -metal	mu metal
$\mu\text{m}$	micrometer
MP2	second order Møller-Plesset method
ms	microsecond
M $\Omega$	mega ohm
n	adjustable parameter
NB	nitrobenzene
Nd:YAG	neodymium-doped Yttrium Aluminium Garnet; Nd:Y <sub>3</sub> Al <sub>5</sub> O <sub>12</sub>
nm	nano meter
NP	neutral nitrophenols
NPA	natural population analysis
NP-H <sup>-</sup>	deprotonated nitrophenols
ns	nano second
NT	nitrotoluene
OFHC	oxygen-free high conductivity copper
OPO	optical parametric oscillator
P(eKE)	electron velocity distribution as a function of electron kinetic energy
P(r)	electron velocity distribution as a function of radial position
P43	Gd <sub>2</sub> O <sub>2</sub> S:Tb
PAD	photoelectron angular distribution
PBE0	Perdew-Burke-Ernzerhof exchange-correlation functional
PEEK	polyether ether ketone plastic
PES	photoelectron spectroscopy

pF	picoFarads
pKa	acid dissociation constant
psi	pounds per square inch
Q	radical species
Q1	quadrupole 1
Q1MS	quadrupole 1 mass spectrometry
Q2	octapole
Q3	quadrupole 3
<i>r</i>	radial position
R	aromatic ring
RC	resistor-capacitor circuit
<i>r</i> <sub>cal</sub>	radial position of calibration species
RF	Radio frequency
RRKM	Rice-Ramsperger-Kassel-Marcus theory
S <sup>2</sup>	total spin
SHOMO	Singly highest occupied molecular orbital
t	time
T <sub>0</sub>	leading trigger pulse
t <sub>0</sub>	initial time-of-flight constant
t <sub>1</sub>	time of flight for anion 1
t <sub>2</sub>	time of flight for anion 2
TMP	turbomolecular pump
TNB	1,3,5-trinitrobenzene

TNT	2,4,6-trinitrotoluene
TOF-MS	time-of-flight mass spectrometry
TTL	transistor-transistor logic
V	volt
$v$	velocity
$v''$	excited vibrational state
$v'$	ground vibrational state
$V_{\text{ANODE}}$	voltage anode
$V_{\text{cal}}$	velocity of calibration species
VDE	vertical detachment energy
$V_{\text{INPUT}}$	voltage input
VMI	velocity map imaging
$V_{\text{OUTPUT}}$	voltage output
W	Watt
$X$	ground vibrational state term
$\beta$	anisotropy parameter
$\Delta\text{DE}$	difference in detachment energies
$\varepsilon$	electric field vector
$\theta$	polar angle
$\pi$	pi orbital
$\pi^*$	anti-bonding pi orbital
$\sigma$	sigma orbital
$\sigma_0$	intensity scaling factor

$\sigma_l$  cross section of  $l$ th partial wave  
 $\sigma_{\text{tot}}$  total photodetachment cross section

## ACKNOWLEDGMENTS

I would like to thank the Department of Chemistry at The University of Alabama, the Graduate Council Fellowship and the GAANN fellowship selection committees for footing the bill for my doctorate degree. A big thank you goes to the amazing technical staff at our college electronic (Danny and Billy) and machine (Mike, Joe, and David) shops. Without the hard work and skill of these individuals the research described in this this dissertation would not have been possible. Specifically, I owe Billy a tremendous amount of thanks for never kicking me out of his shop, teaching me how to make coax cables, and for providing some wonderful conversations about Star Wars and Marvel Comics. I would also like to thank Drs. Shane Street, Marco Bonizzoni, and Greg Szulczweski for the role they played in my education at The University of Alabama. Additional thanks are owed to my dissertation committee for their time and numerous contributions to my education.

I would like to thank Ms. Judy Carnes and Mr. Gary Meredith for instilling in me a deep love of learning from a very early age. Mr. Greg Grey, Mr. Jeff Prewitt (my other older brother), and Mr. Howard White have my deepest appreciation for providing mentorship, motivation, and direction. The wisdom of these outstanding men influences every important decision in my life. A significant amount of gratitude is also owed to Dr. Donald Butler, Mr. & Mrs. Stover, Mr. & Mrs. Henderson for helping shape the way I experience the world. Gratitude is especially given to Dr. Pat Powell, Mrs. Suzanne Powell, and Mr. Chris Shumate for a similar reason. Thanks are also required for my amazing friends: Alie Mallet, Ashley Jolly, Bradley Smith, Michele Stover, Rachael Albury, Adams Reilly, Jerad Watson, and Steve Rogers. These are the most supportive

and wonderful friends any individual could encounter. I am very grateful to my research group for their friendship, encouragement, and trips to Moe's. Specifically, Dr. Dan Goebbert, my adviser, is deserving of a great amount of gratitude, respect, and possible saint hood. Through his guidance, which I did not always appreciate, I have learned how to "figure out how to figure it out". The skills and life lessons I have learned from Dr. Goebbert will forever impact my life.

I would also like to acknowledge Drs. Jeremy Maddox, Darwin Dahl, and Stuart Burris for their wonderful instruction and mentorship at Western Kentucky University. Words cannot possibly explain the gratitude and love I have for Ms. Alicia Pesterfield and Dr. Les Pesterfield, my chemistry parents.

Lastly, thanks are given to my family for their continued support in my life and wisdom. Specifically I would like to thank my older siblings, Jason and Amber, for making sure I was strong enough to stand up for and take care of myself. I did not always agree with their methods, but I cannot argue with the results. My grandmother, Geneva, Aunt Sandy, Aunt Nean, and Uncle Bobby have also made many valuable contributions to my life. Most importantly, my deepest gratitude goes to my mom and dad, Mitzie and Mike Pruitt. I appreciate the sacrifices and encouragement they have provided on my behalf my entire life.

## CONTENTS

ABSTRACT.....	ii
DEDICATION.....	iv
LIST OF ABBREVIATIONS AND SYMBOLS.....	v
ACKNOWLEDGMENTS.....	xiii
LIST OF TABLES.....	xix
LIST OF FIGURES.....	xxi
CHAPTER 1: INTRODUCTION.....	1
1.1 Nitro Containing Energetic Materials.....	1
1.2 Energetic Properties.....	3
1.3 Experimental Measurements of Energetic Properties.....	5
1.3.1 Photoelectron Spectroscopy.....	5
1.3.2 Energy Resolved Mass Spectrometry.....	6
1.4 Dissertation Overview.....	7
CHAPTER 2: EXPERIMENTAL SETUP AND DATA ANALYSIS.....	9
2.1 Overview of Negative Ion Photoelectron Imaging Spectrometer.....	9
2.2 Vacuum Hardware.....	11
2.3 Ion Sources.....	13
2.4 Time-of-Flight Mass Spectrometer.....	14
2.5 Laser System.....	19
2.6 Velocity Map Imaging Assembly.....	20

2.7	Triggering Sequence.....	23
2.8	Analysis of Photoelectron Images.....	25
2.9	Mass Spectrometry.....	29
2.9.1	Experimental Overview.....	29
2.9.2	Instrumental Overview.....	29
2.9.3	Ion Sources.....	31
2.9.4	Analyzer Assembly.....	34
2.10	Modes of Operation.....	36
2.10.1	Q1MS.....	36
2.10.2	Collision Induced Dissociation.....	36
2.10.3	Energy Resolved Mass Spectrometry.....	36
CHAPTER 3: PHOTOELECTRON ANGULAR DISTRIBUTIONS OF CH <sup>-</sup> .....		38
3.1	Introduction.....	38
3.2	Methods.....	39
3.3	Results and Discussion.....	39
3.3.1	Photoelectron Spectra.....	39
3.3.2	Photoelectron Angular Distributions.....	42
3.4	Conclusions.....	53
CHAPTER 4: PHOTOELECTRON IMAGING OF NITROMETHANE CLUSTER ANIONS.....		54
4.1	Introduction.....	54
4.2	Methods.....	56
4.3	Results and Discussion.....	57
4.3.1	Photoelectron Images and Spectra.....	57

4.3.2	Structure Calculations.....	61
4.3.3	Vertical Detachment and Adiabatic Detachment Energies.....	65
4.3.4	Cluster Structure – Experiment and Theory.....	66
4.3.5	Ion Solvation Energies.....	69
4.4	Conclusions.....	71
CHAPTER 5: C-N DISSOCIATION ENERGIES OF NITROBENZENE AND NITROTOLUENE RADICAL ANIONS AND NEUTRALS.....		72
5.1	Introduction.....	72
5.2	Methods.....	77
5.3	Threshold Modeling.....	78
5.4	Results and Discussion.....	79
5.4.1	Collision Induced Dissociation.....	79
5.4.2	Anion Dissociation Energies.....	81
5.4.3	Neutral Dissociation Energies.....	83
5.4.4	Theoretical Comparison.....	84
5.4.5	Electron Detachment.....	86
5.5	Conclusions.....	86
CHAPTER 6: FRAGMENTATION OF DEPROTONATED NITROPHENOL ANIONS.....		88
6.1	Introduction.....	88
6.2	Methods.....	89
6.3	Results and Discussion.....	90
6.3.1	Collision Induced Dissociation.....	90
6.3.2	Energy Resolved Mass Spectrometry.....	92
6.3.3	Theoretical Calculations.....	94

6.3.4	Experimental and Theoretical Comparison	99
6.3.5	Analysis of C-N Dissociation Energies	101
6.4	Conclusions	106
CHAPTER 7: THE DECOMPOSITION OF COPPER NITRATE CLUSTER ANIONS		107
7.1	Introduction	107
7.2	Methods	108
7.3	Results	109
7.3.1	Mass Spectra	109
7.3.2	Collision Induced Dissociation	111
7.3.3	Energy Resolved Mass Spectrometry	113
7.4	Discussion	115
7.4.1	Cluster Fragmentation	115
7.4.2	Optimized Structures	120
7.4.3	Energetics	123
7.4.4	Metal Oxidation State	125
7.5	Conclusions	128
CHAPTER 8: CONCLUSIONS		130
8.1	Summary of Dissertation	130
8.2	Conclusions from Photoelectron Imaging Studies	130
8.3	Conclusions from Mass Spectrometry Studies	132
REFERENCES		134

## LIST OF TABLES

Table 2.1: Power and energy measurements for pulsed Nd:YAG laser used in photoelectron imaging experiments.....	19
Table 3.1: Allowed free-electron symmetries for detachment from $\Psi_{bound}$ orbital with $\Sigma^+$ character within the $C_{\infty v}$ point group.....	44
Table 3.2: Allowed free-electron symmetries for detachment from $\Psi_{bound}$ orbital with $\Pi$ character within the $C_{\infty v}$ point group.....	45
Table 4.1: Comparison between experimental and theoretical vertical detachment energies (VDEs), adiabatic detachment energies (ADEs), and differences in detachment energies ( $\Delta$ DEs) for each cluster structure. ....	68
Table 4.2: Solvation energies for the nitromethane clusters.....	71
Table 5.1: Experimental thermochemical values measured and used in this work.....	76
Table 5.2: Experimental and theoretical values for the dissociation energies, $D_0$ , (eV) of nitrobenzene (NB) and nitrotoluene (NT) isomers.....	85
Table 5.3: Calculated electron affinities, EA, (eV), for nitrobenzene, nitrotoluene isomers, and nitrogen dioxide.....	85
Table 6.1: Theoretical dissociation energies for the elimination of $\text{NO}_2^-$ from neutral nitrophenols (NP), deprotonated nitrophenols ( $\text{NP-H}^-$ ), and nitrobenzene (NB) or nitrotoluene (NT) neutrals and anions calculated at the B3LYP/aug-cc-pVDZ level of theory.....	103

Table 6.2: Electron affinities of nitrotoluene (NT), nitrophenoxyl radicals (NP-H) and NO <sub>2</sub> .....	106
Table 7.1: Calculated energy differences (including zero-point energy corrections) for dissociation reactions of copper nitrate anions at the B3LYP/6-311+G(3df) level of theory.....	124
Table 7.2: Calculated charges and electron configurations for copper atoms at the B3LYP/6-311+G(3df) level of theory using a natural population analysis.....	124
Table 7.3: Summary of the decomposition reactions of copper nitrate anion clusters and the oxidation state of the metal in the reactant and product according to theoretical calculations.....	128

## LIST OF FIGURES

Figure 1.1: Schematic potential energy curves showing the definitions of thermochemical quantities extracted from photoelectron spectra (inset on the top right). The electron affinity, also known as the adiabatic detachment energy, is described by the blue pathway. The vertical detachment energy is described by the red pathway.....	4
Figure 1.2: Negative ion thermochemical cycle illustrating the relationship between bond dissociation energies ( $D_0$ ) and electron affinities (EA) of a generic molecule (AB) and its corresponding anion ( $AB^-$ ). .....	5
Figure 2.1: Instrumental schematic of the negative ion photoelectron imaging spectrometer used in Chapters 3 – 4. Figure made by Mr. Bradley Smith (The University of Alabama). .....	10
Figure 2.2: Schematic drawing of the vacuum chamber housing the negative ion photoelectron imaging spectrometer. A 10” diffusion pump is used to evacuate the vacuum chamber. Turbo molecule pumps are used to achieve ultra-high vacuum conditions. ....	12
Figure 2.3: Circuit diagram of the bias network for the ion detector. A regulated -200 V voltage drop between the $V_{ANODE}$ and $V_{OUTPUT}$ is regulated by the Zener diode. Two 2200 pF capacitors in parallel provide the 4400 pF capacitance. This blocks the HV DC component of the anode, allowing the AC component to travel to the preamplifier.....	17
Figure 2.4: Time-of-Flight scale mass spectrum obtained using the negative ion photoelectron imaging spectrometer. ....	18
Figure 2.5: Mass-to-Charge scale mass spectrum. The spectrum in Figure 2.4 was converted to the mass-to-charge scale using Eqs. (2.5) and (2.6). ....	18

Figure 2.6: Circuit diagram of the bias network with gated gain for the imaging detector. Voltage is applied to the first MCP plate using the $V_{\text{INPUT}}$ . Additional voltage is applied to the output of the second MCP using $V_{\text{OUTPUT}}$ . Approximately 6.5 kV is applied to the P43 screen. ....	22
Figure 2.7: Triggering sequence for the photoelectron imaging experiment. Delay times representative of experimental values are listed. The timing sequence is initiated by the IOTA ONE valve driver, $T_0$ . Channels A – G are controlled by the digital delay generator. ....	24
Figure 2.8: Photoelectron image of (A) $\text{O}^-$ taken at 532 nm and (B) reconstruction of projected image completed using the BASEX program. The blue arrow indicates the laser polarization axis. ....	25
Figure 2.9: (A) Reconstructed image of $\text{O}^-$ taken at 532 nm. (B) Photoelectron spectrum obtained from the reconstructed image. Intensity is plotted as a function of electron binding energy. (C) Photoelectron angular distribution for $\text{O}^-$ . The black diamonds correspond to experimental data. The red line is a fit to Eq. (2.11). The anisotropy parameter ( $\beta$ ) was determined using Eq. (2.11). ....	28
Figure 2.12: Instrumental schematic of the triple quadrupole mass spectrometer (Finnigan TSQ-7000) used in Chapters 5 – 7. ....	30
Figure 2.13: Schematic of electrospray ionization (ESI) source utilized in Chapter 7. ....	32
Figure 2.14: Schematic of the mechanism of anion formation for the ESI source. ....	32
Figure 2.15: Schematic of the atmospheric pressure chemical ionization (APCI) source used in Chapters 5 and 6. ....	33
Figure 2.16: Schematic of anion formation mechanism using the APCI source. ....	34
Figure 2.17: Analyzer assembly for triple quadrupole mass spectrometer. Q1 and Q3 are quadrupole mass analyzers. Q2 is an octapole collision cell. Electrostatic lenses are labeled L1, L2, L3, and L4. ....	35

Figure 3.1: Representative photoelectron image and photoelectron spectrum of CH <sup>-</sup> measured at 532 nm. Anion orbitals from B3LYP/aug-cc-pVTZ calculations show orbitals electrons are ejected from to yield each electronic state. The energy scale is the electron binding energy obtained by subtracting the electron kinetic energy from the photon energy according to Eq. (1.4) .....	41
Figure 3.2: Photoelectron angular distributions as a function of electron kinetic energy for the <sup>2</sup> Π ← <sup>3</sup> Σ <sup>-</sup> (red diamonds) and <sup>4</sup> Σ ← <sup>3</sup> Σ <sup>-</sup> (blue dots) transitions. The solid lines are fits to each data set using Eq. 3.5. The fractional <i>p</i> character is <i>f</i> = 0.95 for the <sup>2</sup> Π ← <sup>3</sup> Σ <sup>-</sup> transition and <i>f</i> = 0.99 for the <sup>4</sup> Σ ← <sup>3</sup> Σ <sup>-</sup> data but considered unreliable.....	42
Figure 3.3: Schematic electronic energy diagram illustrating the mechanism for anion excitation and electron auto-detachment from the excited state of CH <sup>-</sup> . The corresponding electronic structure diagrams for each state is indicated by the red arrow, and the only low-lying neutral state allowed by electron auto-detachment is the <sup>4</sup> Σ <sup>-</sup> excited state of CH, as indicated by the red circle.....	52
Figure 4.1: Raw (left) and reconstructed (right) photoelectron images for the nitromethane (a) monomer, (b) dimer, (c) trimer, (d) hydrated monomer anion recorded at 355 nm. The laser polarization axis is vertical in the plane of the figure.....	58
Figure 4.2: Photoelectron spectra of nitromethane anion (a) monomer, (b) dimer, (c) trimer, and (d) hydrated monomer. The energy scale is the electron binding energy (eBE) obtained by subtracting the electron kinetic energy from the photon energy. The vertical detachment energies are listed above the blue arrows. The estimated electron affinities, EA <sub>est</sub> , are listed above the red arrows in italics.....	59
Figure 4.3: Optimized structures and SOMO for the nitromethane anion and neutral at the (U)B3LYP/aug-cc-pVDZ level of theory. Distances are given in Å. C-NO <sub>2</sub> dihedral angles are also reported.....	61
Figure 4.4: Optimized structures and SOMO for the hydrated nitromethane anion and neutral at the (U)B3LYP/aug-cc-pVDZ level of theory. Distances are given in Å. C-NO <sub>2</sub> dihedral angles are also reported.....	62

Figure 4.5: Optimized structures and SOMO for the nitromethane dimer cluster anion and neutral at the (U)B3LYP/aug-cc-pVDZ level of theory. Distances are given in Å. C-NO <sub>2</sub> dihedral angles are also reported.	63
Figure 4.6: Optimized structures and SOMO for the nitromethane trimer cluster anion and neutral at the (U)B3LYP/aug-cc-pVDZ level of theory. Distances are given in Å. C-NO <sub>2</sub> dihedral angles are also reported.	64
Figure 4.7: Schematic potential energy diagram illustrating the approach used to approximate solvation energies in this work.	70
Figure 5.1: Dissociation reactions for <i>o</i> -nitrotoluene: (1) C-N homolysis, (2) NO <sub>2</sub> /ONO rearrangement, and (3) C-H attack.	73
Figure 5.2: Schematic potential energy diagram for nitrobenzene and nitrobenzene radical anion C-N bond cleavage. D <sub>0</sub> corresponds to the dissociation energy of the neutral or anion. EA is the electron affinity of nitrobenzene and NO <sub>2</sub> .	75
Figure 5.3: CID spectra collected at 30 eV <sub>lab</sub> collision energy for (a) nitrobenzene, (b) <i>o</i> -nitrotoluene, (c) <i>m</i> -nitrotoluene, and (d) <i>p</i> -nitrotoluene.	80
Figure 5.4: ERMS spectra for the formation of NO <sub>2</sub> <sup>-</sup> from (A) nitrobenzene, (B) <i>o</i> -nitrotoluene, (c) <i>m</i> -nitrotoluene, and (d) <i>p</i> -nitrotoluene as a function of collision energy. The solid lines correspond to the convoluted fit and the dashed lines to the unconvoluted fits using Eq. (5.2).	82
Figure 6.1: Collision induced dissociation spectra of (A) <i>o</i> -nitrophenoxide, (B) <i>m</i> -nitrophenoxide, (C) <i>p</i> -nitrophenoxide at 20 eV <sub>lab</sub> collision energy with 0.250 mTorr Ar collision gas.	91
Figure 6.2: Energy resolved mass spectra for the fragmentation of (A) <i>o</i> -nitrophenoxide, (B) <i>m</i> -nitrophenoxide, (C) <i>p</i> -nitrophenoxide. The collision energy has been converted to center-of-mass frame using Eq. (2.1).	93

Figure 6.3:	Calculated potential energy diagram for the dissociation of <i>o</i> -Nitrophenoxide anion at the B3LYP/aug-cc-pVDZ level of theory. The cyan pathway corresponds to loss of NO <sub>2</sub> <sup>•</sup> . The black pathway corresponds to loss of NO <sub>2</sub> <sup>-</sup> . The red pathway corresponds to the rearrangement of the nitro group followed by the loss of NO <sup>•</sup> . Minor fragmentation pathways are reported in magenta and blue. ....	96
Figure 6.4:	Calculated potential energy diagram for the dissociation of <i>m</i> -Nitrophenoxide anion at the B3LYP/aug-cc-pVDZ level of theory. The cyan pathway corresponds to loss of NO <sub>2</sub> <sup>•</sup> . The black pathway corresponds to loss of NO <sub>2</sub> <sup>-</sup> . The red pathway corresponds to the rearrangement of the nitro group followed by the loss of NO <sup>•</sup> . ....	97
Figure 6.5:	Calculated potential energy diagram for the dissociation of <i>p</i> -Nitrophenoxide anion at the B3LYP/aug-cc-pVDZ level of theory. The cyan pathway corresponds to loss of NO <sub>2</sub> <sup>•</sup> . The black pathway corresponds to loss of NO <sub>2</sub> <sup>-</sup> . The red pathway corresponds to the rearrangement of the nitro group followed by the loss of NO <sup>•</sup> . ....	98
Figure 6.6:	Resonance structure of <i>o</i> -nitrophenoxide illustrating resonance stabilization of the excess electron. ....	103
Figure 6.7:	Potential energy diagram illustrating the relationship between C-N bond dissociation energies (D <sub>0</sub> ) and electron affinities (EA) of a nitroaromatic (X-NO <sub>2</sub> ) and its corresponding anion (X-NO <sub>2</sub> <sup>-</sup> ). ....	105
Figure 7.1:	Mass spectrum of 0.1 mM copper (II) nitrate solution in 25/75 (%v/v) methanol/water solvent. The upper inset shows the isotropic pattern for Cu(NO <sub>3</sub> ) <sub>3</sub> <sup>-</sup> . ....	110
Figure 7.2:	Collision induced dissociation mass spectra of (a) Cu(NO <sub>3</sub> ) <sub>3</sub> <sup>-</sup> and (b) Cu(NO <sub>3</sub> ) <sub>2</sub> <sup>-</sup> at 30 eV <sub>lab</sub> collision energy with 0.50 mTorr Ar collision gas. ....	112
Figure 7.3:	Energy resolved mass spectra for the fragmentation of (a) Cu(NO <sub>3</sub> ) <sub>2</sub> <sup>-</sup> and (b) Cu(NO <sub>3</sub> ) <sub>2</sub> <sup>-</sup> . ....	114

Figure 7.4: Hypothetical molecular orbital diagram for the formation of CuO from Cu <sup>+</sup> and O <sup>-</sup> . The relative orbital energies suggest the copper atom is not oxidized upon bond formation with oxygen and the unpaired electron remains on the oxygen atom. ....	119
Figure 7.5: Optimized copper anion cluster structures calculated at the B3LYP/6-311+G(3df) level of theory. Atomic charges were calculated for each cluster using the natural population analysis method. ....	120
Figure 7.6: Optimized neutral copper cluster structures calculated at the B3LYP/6-311+G(3df) level of theory. Atomic charges were calculated using the natural population analysis method. ....	122

## CHAPTER 1

### INTRODUCTION

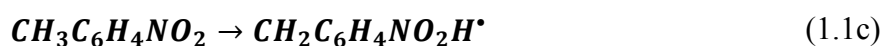
#### 1.1 Nitro Containing Energetic Materials

Nitro (-NO<sub>2</sub>) containing compounds are an important class of highly energetic materials. These compounds have the ability to quickly release stored potential energy.<sup>1-4</sup> This property has resulted in the wide use of nitro compounds in military explosives. For example, Hitler's Luftwaffe in World War II, used the Sprengbombe Cylindrisch 1000 bomb filled with a 15% cyclotrimethylenetrinitramine (RDX) and 70% 2,4,6-trinitrotoluene (TNT) mixture.<sup>5</sup> In the Vietnam War the United States used the BLU-43/B "Dragontooth" cluster landmines made from a nine gram mixture of nitromethane and nitroethane.<sup>6</sup> Most recently in the War on Terror, C-4, made of 91% RDX, has been used extensively.<sup>7</sup>

One reason nitro compounds are so widely used in the explosives industry is the chemical stability of the compounds. Explosives made from nitro compounds can be classified as insensitive munitions.<sup>8</sup> These explosives are stable enough to allow transport by military vehicles, but are energetic enough to destroy targets when detonated.<sup>9</sup> The low shock sensitivity of these explosives requires an external energy source to cause detonation. Typically, this external energy source is supplied by chemical or electrical means.<sup>2</sup>

Numerous studies have been focused on the chemical decomposition processes that occur in the detonation step.<sup>4,10,11</sup> Currently, the general consensus is the first step in explosive detonation must involve homolytic cleavage of the weakest bond in the molecule. In the case of

nitroaromatic compounds, such as TNT, three major steps are thought to occur in during thermal decomposition. These reactions are shown in Eq 1.1a-c for *o*-nitrotoluene and include (a) C-NO<sub>2</sub> homolysis, (b) isomerization of the NO<sub>2</sub> to an ONO, nitrite group, resulting in elimination of NO•, and (c) attack of the methyl substituent to form –NO<sub>2</sub>H, ultimately resulting in the loss of water.<sup>4,10,11</sup>



The shock sensitivity, or ease with which the explosives can be detonated, has been linked to the amount of energy required to cause homolytic cleavage of the C-NO<sub>2</sub> bond.<sup>4</sup> Understanding the shock sensitivity of explosive compounds is critical to developing new explosives as well as implementing proper handling and ordinances for dealing with explosive materials. Rice *et al.* calculated C-NO<sub>2</sub> bond dissociation energies (BDEs) for a variety of nitroaromatic molecules and discovered a rough correlation between the logarithm of the impact sensitivity and the calculated BDEs.<sup>12</sup> In molecules where the C-NO<sub>2</sub> bond is the weakest, the dissociation energy can be used to index the relative sensitivity.<sup>3</sup> Song reported the weakest BDE scaled by the total molecular energy serves as a reasonable indicator of explosive sensitivity.<sup>4</sup> In addition to the bond dissociation energies, numerous other properties of individual nitro and nitrate containing molecules, such as vibrational states of the molecule,<sup>13,14</sup> molecular electronegativities,<sup>15,16</sup> heats of reaction,<sup>17</sup> and partial atomic charges<sup>5,16,18-20</sup> have been linked to explosive characteristics. These works motivate the need to understand and measure the energetic properties of nitro containing molecules to advance the understanding of these explosive materials.

## 1.2 Energetic Properties

Energetic properties, such as bond dissociation energies, are vital to understand the relationship between chemical reactions (explosions) and energy. A fundamental understanding of these energetic properties is necessary to fully understand any chemical process. Energetic quantities of specific interest to this dissertation are illustrated in Figure 1.1. The energy difference between a neutral species and the anionic species is known as the electron affinity (EA). The EA is typically positive for a system that forms a stable anion. This implies the anion is lower in energy than the neutral species. The adiabatic detachment energy (ADE) is another term for electron affinity. The ADE values are identified by determining the energy associated with the transition from the ground vibrational state of the anion to the ground vibrational state of the neutral. Occasionally, it is not possible to accurately measure the energy associated with this transition. In these cases the vertical detachment energy (VDE) is a useful quantity. The VDE is the energy associated with the transition from the ground vibrational level of the anion species to the most populated vibrational energy level of the neutral species. The VDE corresponds to the transition with the greatest Franck-Condon overlap. Another way of thinking about the VDE is the amount of energy required for the near instantaneous removal of an electron from the anion.

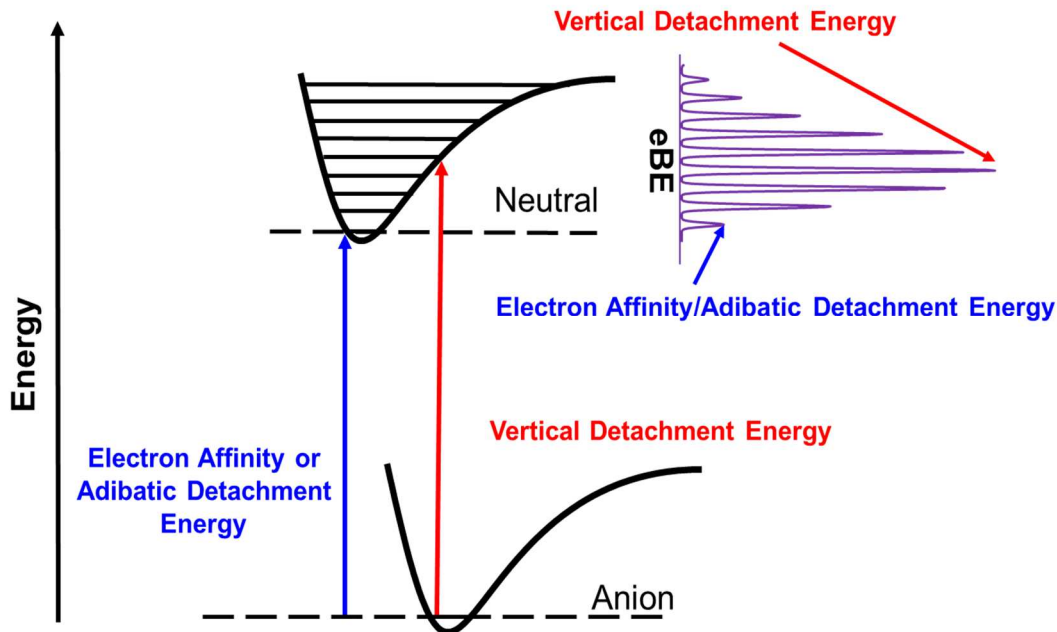


Figure 1.1: Schematic potential energy curves showing the definitions of thermochemical quantities extracted from photoelectron spectra (inset on the top right). The electron affinity (EA), also known as the adiabatic electron detachment energy (ADE), is described in by the blue pathway. The vertical detachment energy (VDE) is described by the red pathway.

The relationship between the electron affinity of a molecule and the bond dissociation energy of the molecule can be expressed by the negative ion thermochemical cycle. This relationship is summarized in Eq. (1.2)

$$D_0(AB) = -EA(AB) + D_0(AB^-) + EA(A) \quad (1.2)$$

where  $D_0(AB)$  represents the bond dissociation energy of molecule  $AB$ ,  $EA(AB)$  is the electron affinity of  $AB$ ,  $D_0(AB^-)$  is the dissociation energy of the anion  $AB^-$ , and  $EA(A)$  is the electron affinity of the neutral fragment  $A$ . Figure 1.2 shows the dissociation energy for the neutral species is obtainable from measurements made on the corresponding anionic species. This is particularly important because it is considered difficult to directly measure bond dissociation energies for neutral species using traditional techniques such as bomb calorimetry.

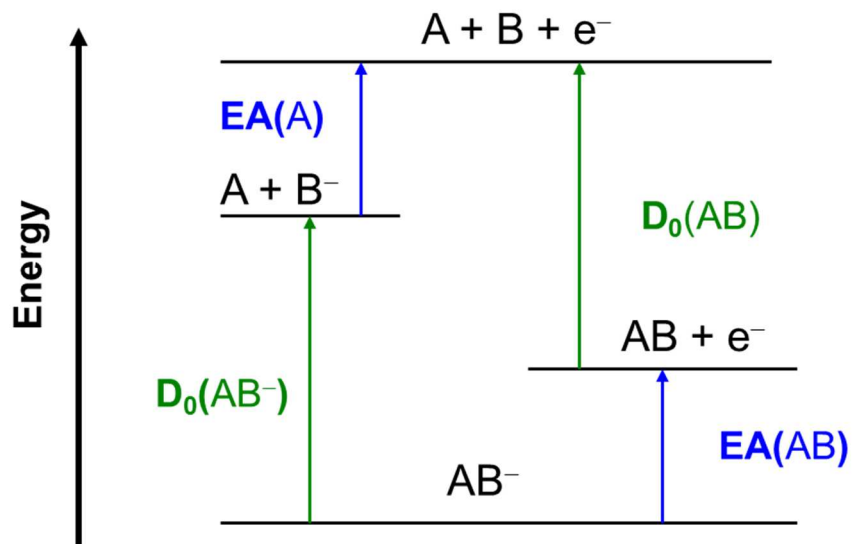


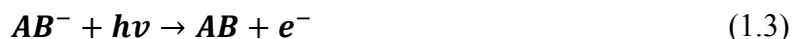
Figure 1.2: Negative ion thermochemical cycle illustrating the relationship between bond dissociation energies ( $D_0$ ) and electron affinities ( $EAs$ ) of a generic molecule ( $AB$ ) and its corresponding anion ( $AB^-$ ).

### 1.3 Experimental Measurements of Energetic Properties

Two experimental techniques have been utilized in this dissertation for the purpose of measuring energetic properties of nitro containing molecules. Photoelectron Spectroscopy (PES) allows for the measurement of electron affinity and vertical detachment energies. Energy Resolved Mass Spectrometry (ERMS) can be used to measure the bond dissociation energies of specific anions. The combination of these two experimental techniques allows for the completion of the negative ion thermochemical cycle, therefore, providing a method to determine the bond dissociation energies of neutral nitro containing compounds. Detailed descriptions of each experiment are provided in Chapter 2.

### 1.3.1 Photoelectron Spectroscopy

Photoelectron spectroscopy is based on the photoelectric effect. If an anion,  $AB^-$ , absorbs energy from a photon,  $h\nu$ , the excess electron,  $e^-$ , can be ejected from the molecule. This process is described in Eq. (1.3).



If the energy absorbed from the photon is greater than the electron binding energy of the molecule, the electron is ejected with excess kinetic energy according to the law of conservation of energy and the photoelectric effect. This is illustrated in Eq. (1.4)

$$eKE = h\nu - eBE \quad (1.4)$$

where  $eKE$  is the electron kinetic energy,  $h\nu$  is the energy of the absorbed photon, and  $eBE$  is the electron binding energy. Recording the kinetic energy distribution of the ejected electrons, PES allows for the determination of the electron affinity.

### 1.3.2 Energy Resolved Mass Spectrometry

ERMS relies on the dissociation of a mass-selected precursor anion through collision with an inert target gas. A generic collision reaction is shown in Eq. (1.5)



where  $AB^-$  is the precursor anion,  $Ar$  is the inert target gas,  $A$  is the neutral fragment, and  $B^-$  is the anion fragment. The apparent cross section is measured in the center-of-mass frame as a function of the collision energy. The threshold energy,  $E_0$ , is taken as the minimum amount of energy needed to cause the dissociation energy. This energy is treated as the bond dissociation energy of the anion. Accurate bond dissociation energies can be extracted from the apparent

cross sections by correcting for kinetic shifts using RRKM theory.<sup>21</sup> The kinetic shift corrections account for slow fragmentation process occurring on a timescale slower than the experiment. Additional terms included are internal and translational energy distributions. The bond dissociation energies determined in the ERMS studies, coupled with the electron affinity values measured in the PES studies, allows for the completion of the negative ion thermochemical cycle. The completion of this cycle allows for the determination of neutral bond dissociation energies which have been previously mentioned as crucial to understanding the shock sensitivity of nitro containing explosives.

#### 1.4 Dissertation Overview

The remaining portion of this dissertation is divided into seven chapters. Chapter 2 provides a description of the experimental methods and data analysis procedures utilized in this dissertation. The newly constructed photoelectron imaging spectrometer used in Chapters 3 and 4 is described first. The experimental apparatus used in the mass spectrometry experiments, discussed in Chapters 5 -7, is described in the later part of Chapter 2. Chapter 3 is a functionality study using the photoelectron imaging spectrometer. This chapter is based on the first study, focused on the photoelectron angular distributions of  $\text{CH}^-$ , completed on the photoelectron imaging spectrometer. Solvation effects in nitromethane cluster anions are investigated using the photoelectron imaging spectrometer in Chapter 4. This work demonstrates the ability of the photoelectron imaging experiment to measure energetic properties such as solvation energies, vertical detachment energies, and estimated electron affinity values. Chapters 5 -7 focus on ERMS and collision induced dissociation mass spectrometry experiments. In Chapter 5, the C-N bond dissociation energies of the radical anion forms of nitrobenzene and the three nitrotoluene

isomers are measured. Chapter 6 is a continuation of Chapter 5 to include nitrophenoxide radical anions. Chapter 7 is the first in a series of studies focusing on transition metal nitrate cluster anions. This chapter focuses on the fragmentation pathways and metal chemistry of copper nitrate cluster anions. The key results from Chapters 3 – 7 are summarized in Chapter 8.

The body of work reported in this dissertation is based on the following publication list.

Deepest gratitude is expressed to all coauthors.

Chapter 3

B. Bandyopadhyay, C. J. Pruitt, and D. J. Goebbert, *J. Chem. Phys.*, 138, 201101 (2013).

Chapter 4

C. J. Pruitt, R. M. Albury, and D. J. Goebbert (to be submitted to *Chem. Phys. Lett.*).

Chapter 5

C. J. Pruitt and D. J. Goebbert, *Chem. Phys. Lett.*, 580, 21 (2013).

Chapter 6

C. J. Pruitt, K. Benham, B. Bandyopadhyay, and D. J. Goebbert, *Chem. Phys. Lett.*, 614, 192 (2014).

Chapter 7

C. J. Pruitt and D. J. Goebbert, *J. Phys. Chem. A*, 120, 4755 (2015).

## CHAPTER 2

### EXPERIMENTAL SETUPS AND DATA ANALYSIS

#### 2.1 Overview of Negative Ion Photoelectron Imaging Spectrometer

The imaging experiments described in Chapters 3 – 4 were carried out on the negative ion photoelectron imaging spectrometer described in the remainder of this chapter. The imaging apparatus was built in-house with assistance from The University of Alabama College of Arts and Sciences Machine and Electronic shops. The fundamentals of this instrument can be traced back to Lineberger,<sup>22</sup> Chandler and Houston,<sup>23</sup> Eppink and Parker,<sup>24</sup> and Sanov.<sup>25</sup> A schematic of the negative ion photoelectron imaging spectrometer is shown in Figure 2.1.

In this experiment, a sample gas is introduced into the apparatus through a pulsed valve, creating a supersonic expansion. An ion source (discharge or electron gun) creates an electrically neutral plasma. Anions in this plasma are extracted into a time-of-flight mass spectrometer (TOF-MS).<sup>26</sup> These anions are propelled down the flight tube by a set of extraction plates. Just before entering the flight tube, two sets of deflectors and an Einzel lens help to steer and focus the anions. An in-line detector allows for the detection of the anions. The resulting spectrum is the time-of-flight resolved masses. A pulsed laser can be timed to overlap with a specific packet of anions. The overlap between the anion packet and laser causes electron detachment from the anion. These detached electrons are known as photoelectrons.

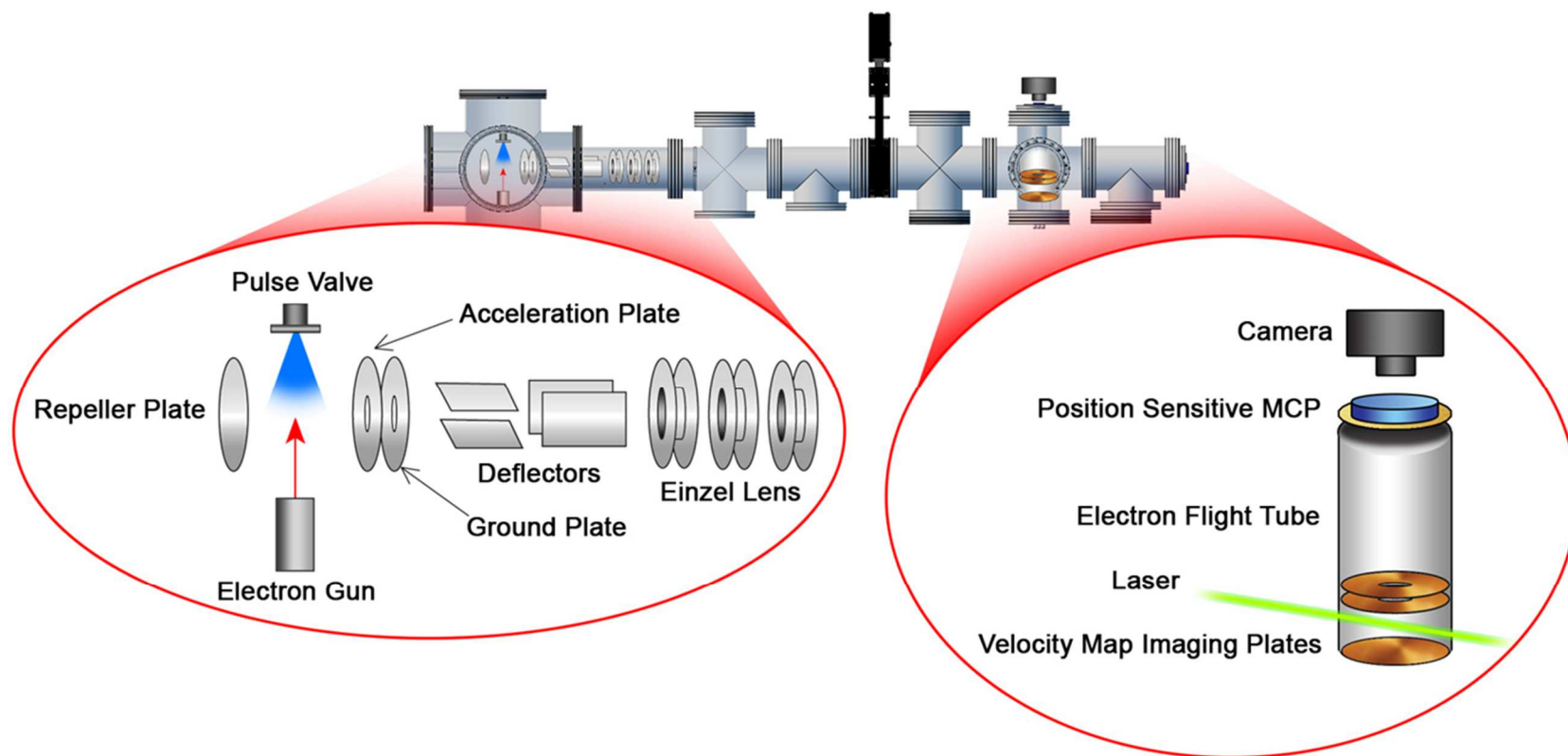


Figure 2.1: Instrumental schematic of the negative ion photoelectron imaging spectrometer used in Chapters 3 – 4. Figure made by Mr. Bradley Smith (The University of Alabama).

The velocity map imaging (VMI)<sup>23,24</sup> assembly, perpendicular to the ion flight path, allows for the detection of the detached photoelectrons with a position sensitive detector. A charge coupled device (CCD) camera is utilized to record the photoelectron images produced from the detached photoelectrons striking the imaging detector.

## 2.2 Vacuum Hardware

The instrument is made of two differentially pumped sections, the ion source chamber/flight tube and the detection region. The entire vacuum chamber is made of 304L stainless steel. A schematic of the vacuum chamber is shown in Figure 2.2. The source chamber is held under vacuum by a diffusion pump (DP) (Oerlikon Leybold, model DIP 3000) with a nominal pumping speed of 3000 l/s for air. The DP is mounted to a tee. A 10” pneumatic gate valve (VAT, Series 121) separates the tee and the source chamber to prevent oil contamination of the source region. Santovac 5 pump oil is utilized in the DP to minimize back-streaming. A rotary vane mechanical pump (Oerlikon Leybold, model D40B) with a pumping speed of 40 m<sup>3</sup>/hr acts as the backing pump. The DP is water-cooled by a chiller (Dimplex Thermal Solutions, model 1000MM-JT). When operating the DP, the baseline pressure of the source region is  $1 \times 10^{-6}$  Torr. The detection region is isolated from the flight tube by another pneumatic gate valve (A&N Corporation, GV600-CF-E-P). Turbo molecular pumps (TMPs) (Oerlikon Leybold, Turbovac TMP 361), with nominal pumping speeds of 400 l/s, are mounted directly to 8” conflate (CF) flanges in a parallel configuration in the detection region. Rotatory vane mechanical pumps (Oerlikon Leybold, D16B) with pumping speeds of 16 m<sup>3</sup>/hr back each TMP. The same water chiller used to cool the DP is employed to cool the TMPs. The baseline pressure of the detection region is  $1 \times 10^{-8}$  Torr.

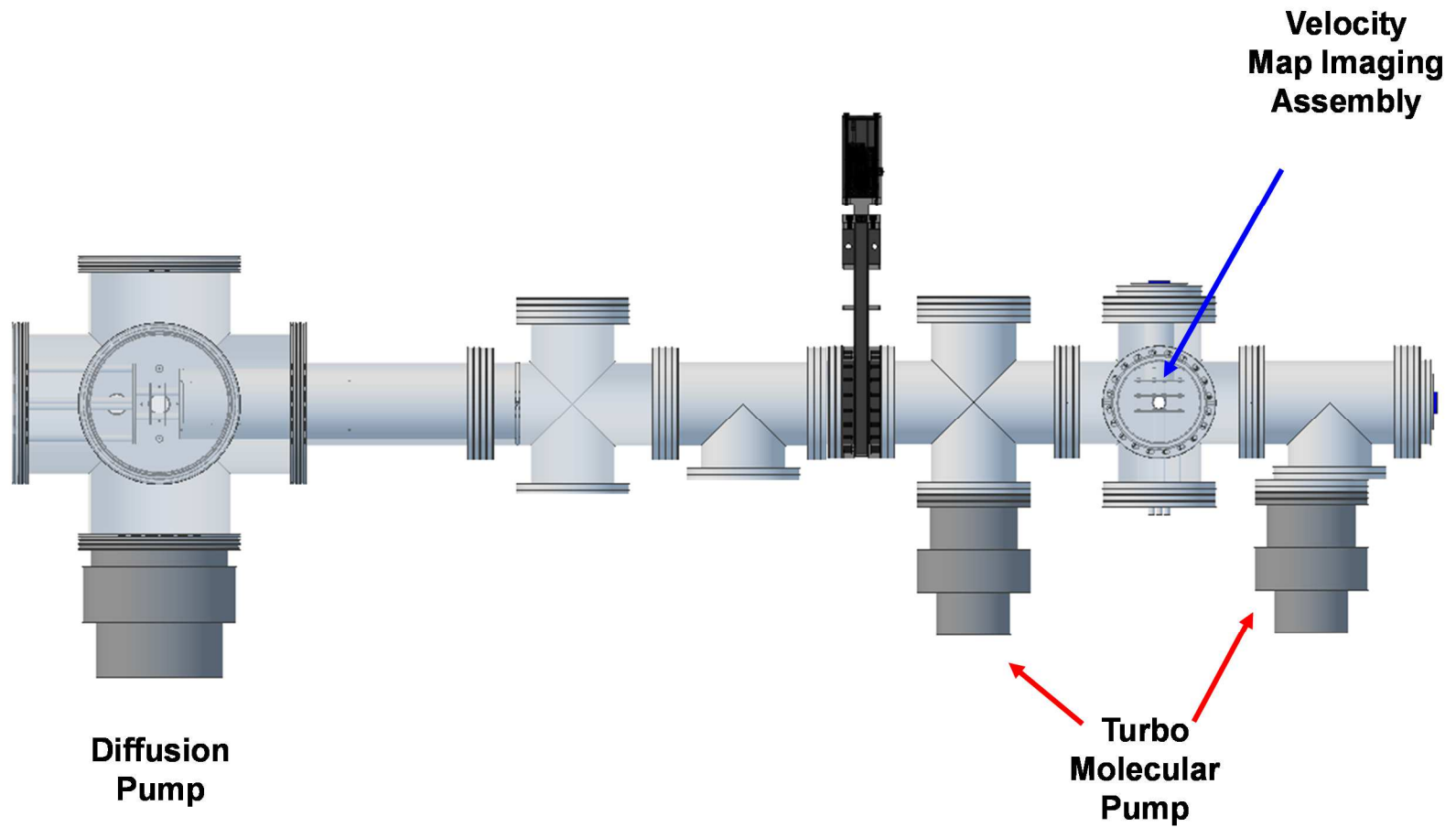
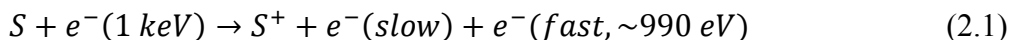


Figure 2.2: Schematic drawing of the vacuum chamber housing the negative ion photoelectron imaging spectrometer. A 10" diffusion pump is used to evacuate the vacuum chamber. Turbo molecular pumps are used to achieve ultra-high vacuum conditions.

## 2.3 Ion Sources

A sample gas is introduced into the vacuum chamber *via* supersonic expansion from a pulsed solenoid valve (General Valve, Series 99) with a nozzle orifice of  $\sim 800 \mu\text{m}$  and a conical half-angle of  $45^\circ$ . The magnetic force generated by the solenoid lifts a spring-loaded PEEK poppet to open the valve. An IOTA ONE high speed valve driver (Parker Hannifin Corp., General Valve, model DG535) controls the firing of the valve. The valve is triggered externally by a TTL pulse ( $T_0$ ) from a delay generator (Stanford Research Systems, Inc., model DG535). Typically, the valve operates at a frequency of 10 Hz, and is opened for approximately  $\sim 120 - 130 \mu\text{s}$ . When the valve is operating the pressure in the source chamber is  $1-2 \times 10^{-5}$  Torr, while the pressure in the detection region is approximately  $4.5 \times 10^{-7}$  Torr.

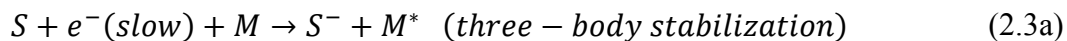
An electron gun (Kimball Physics Inc., EGPS-1017B) is mounted in line with the pulse valve. A high current ( $\sim 3.5$  Amps) is passed through a bent tungsten filament, heating the filament. Thermionic emission from the filament produces a high energy (1 keV) electron beam that penetrates through the supersonic expansion, resulting in slow secondary electrons from an ionized sample, S. This process is shown in Eq. (2.1).



Energetic anions,  $S^{-*}$ , are produced by secondary electron attachment to the neutral species, Eq. (2.2).



The nascent anions can energetically relax by three mechanisms, Eq. (2.3)





If the stabilization pathways are not accessible to the anion, the excess electron will be lost. The plasma generated from the supersonic expansion is electrically neutral. This implies the high energy electrons are scattered out of the jet. The slow moving electrons cool in the expansion through inelastic events.<sup>27</sup> Low energy ion-neutral collisions allow for the formation of other anionic species.

Discharge ionization sources, with a variety of electrode geometries, have also been developed. These discharge sources are designed to be attached directly to the face plate of the pulse valve. As the gas exits the pulse valve it passes through an electrical discharge generated by applying a high voltage to one electrode while keeping the other electrode at ground potential. Anion formation proceeds through similar processes described in Eq. (2.3).

## 2.4 Time-of-Flight Mass Spectrometer

A Wiley-McLaren TOF-MS serves as the mass analyzer.<sup>26</sup> The TOF-MS consists of an acceleration region, ion optics, a field free flight tube, and detector. Approximately 6” downstream from the nozzle, the expanding gas containing the synthesized anions enters the TOF-MS orthogonally between the repeller and acceleration plates. Separate high voltage pulse generators (Directed Energy Inc., model PVX-4140) pulse the potential (rise/fall time < 25 ns) applied to the repeller (-3.40 kV) and acceleration (-2.47 kV) plates. Each plate is made of stainless steel with a diameter of 3” and a thickness of 0.04”. The acceleration plate has a 0.5” diameter hole in the middle of the plate covered by a fine nickel mesh, 70 wires per square inch (Precision Eforming, LLC., 90% maximum transmission). The repeller and ground plates are

separated by 1" PEEK insulators. The potential applied to these plates provides the kinetic energy needed for the anions to reach the detector at the end of the flight tube. As the anions leave the acceleration region, they are referenced to a ground potential by passing through a grounding plate. The grounding plate is made of aluminum with a diameter of 4.75" and a 0.25" thickness. The plate is coated in Aquadag (Thor Labs, AQE32), a colloidal graphite coating, to reduce oxidation of the plate. A nickel mesh is also attached to this plate. The grounding plate is separated from the acceleration plate by a 1" Teflon block. Two sets of deflectors (vertical and horizontal) and an Einzel lens focus the anions in the ion optic region. The deflectors are separated from the grounding plate by 1" PEEK insulators. The deflectors and Einzel lens are made of aluminum and coated in Aquadag. The deflectors each measure 2.25" x 1" x 0.25". The Einzel lens is made of three separate spools 3" in diameter with a hole 1" in diameter in the center of each spool. The spools each measure 1.5" in height. The first and third spools are grounded, while the second spool is wired to a high voltage power supply (Gamma High Voltage Research, RMCR5R). The deflectors and Einzel lens are electrically isolated using 0.5" PEEK insulators. Before exiting the ion optics region, the anions are once again referenced back to a ground potential by the third spool of the Einzel lens. This allows us to avoid electrically floating the flight tube. Anions traverse the flight tube and strike a chevron-type dual microchannel plate detector (Burle, Inc.) at the end of the flight tube, 96" from the repeller plate. The MCP detector is 40 mm in diameter and is composed of front and rear MCPs, and an anode plate. In order to power each part of the detector a voltage divider is used in conjunction with a high voltage power supply (Gamma High Voltage Research, RMCR3R). The input voltage ( $+V_{\text{INPUT}}$ ) is divided so the anode plate receives  $V_{\text{OUTPUT}}$ , the rear MCP receives  $V_{\text{OUTPUT}} - 200 \text{ V}$ , and the front MCP receives 66% of  $V_{\text{OUTPUT}}$ . Figure 2.3 shows the electrical schematic for the voltage

divider box constructed in house. The output signal from the anode plate is sent to a 100MHz preamplifier (Phillips Scientific, Model 6931). The amplified signal is recorded on a 300 MHz digital oscilloscope (Rigol, Model 3012) where it is then transferred to a computer for analysis. The acquired spectra can be converted from the time-of-flight to the mass scale using Eq. (2.4)

$$t = a \left( \frac{m}{z} \right)^{1/2} + t_0 \quad (2.4)$$

where  $t$  is the time-of-flight for the anion,  $a$  is a proportionality constant,  $m/z$  is the mass-to-charge ratio for the anion, and  $t_0$  is the initial time-of-flight constant. The values for  $a$  and  $t_0$  are determined by recording the flight times for two anions,  $t_1$  and  $t_2$ , with known  $m/z$  ratios,  $m_1/z$  and  $m_2/z$ . This allows a system of two equations with two unknowns to be solved for  $a$ , Eq. (2.5), and  $t_0$ , Eq. (2.6).

$$a = \frac{t_2 - t_1}{\left( \frac{m_2}{z} \right)^{1/2} - \left( \frac{m_1}{z} \right)^{1/2}} \quad (2.5)$$

$$t_0 = t_1 - a \left( \frac{m_1}{z} \right)^{1/2} \quad (2.6)$$

Figures 2.4 and 2.5 show sample spectra plotted in the time-of-flight scale and mass scale, respectively.

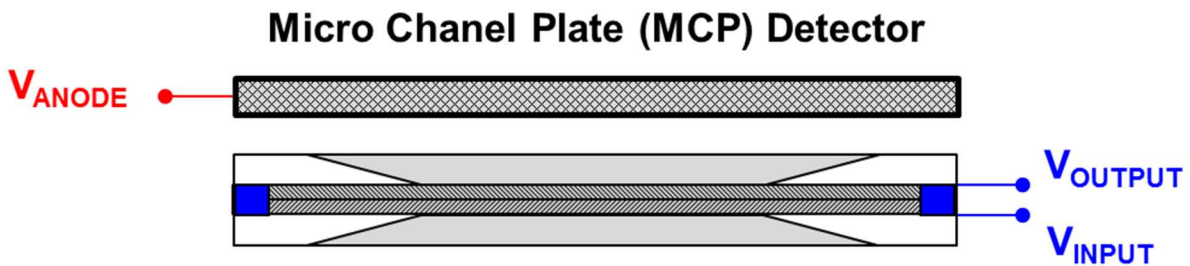
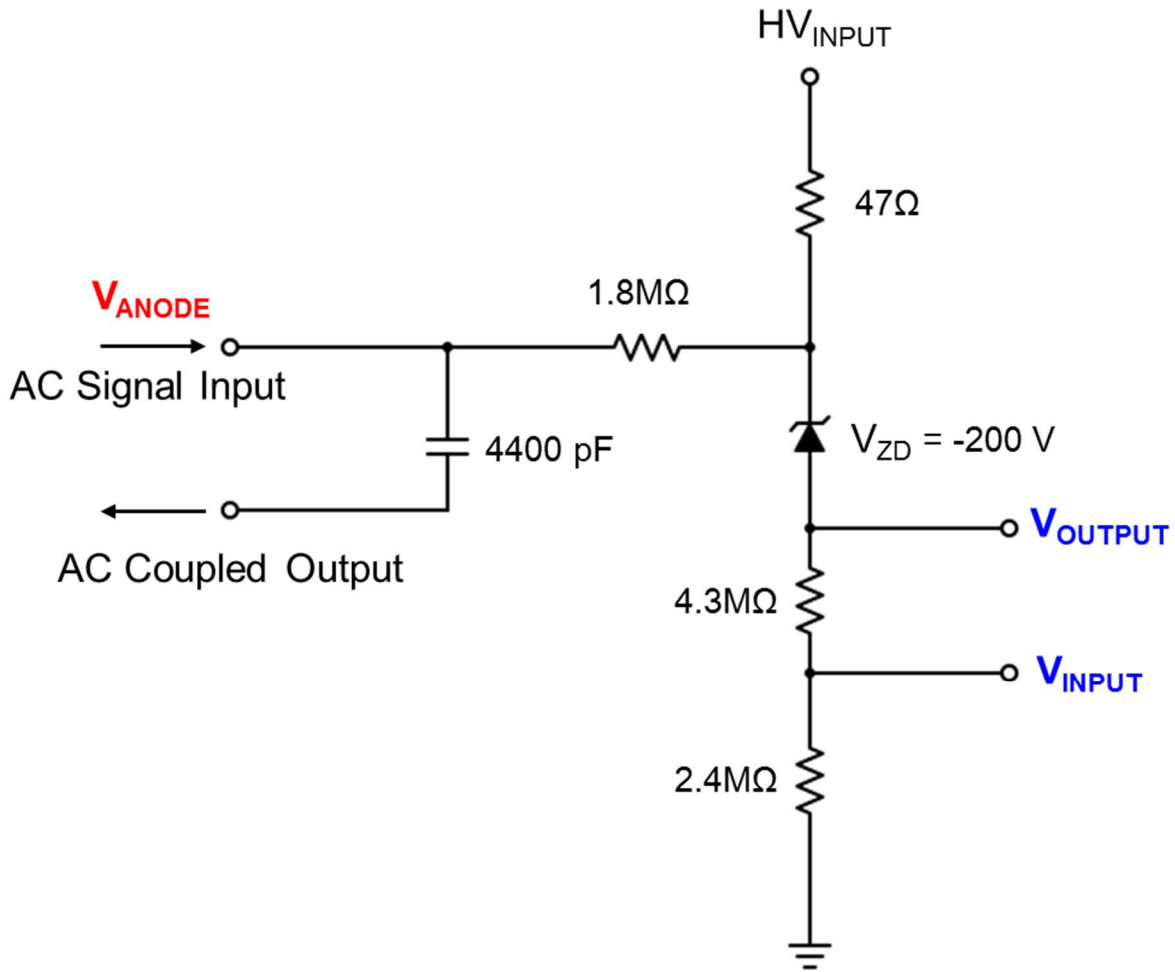


Figure 2.3: Circuit diagram of the bias network for the ion detector. A regulated  $-200\text{ V}$  voltage drop between the  $V_{ANODE}$  and  $V_{OUTPUT}$  is regulated by the Zener diode. Two  $2200\text{ pF}$  capacitors in parallel provide the  $4400\text{ pF}$  capacitance. This blocks the HV DC component of the anode, allowing the AC component to travel to the preamplifier.

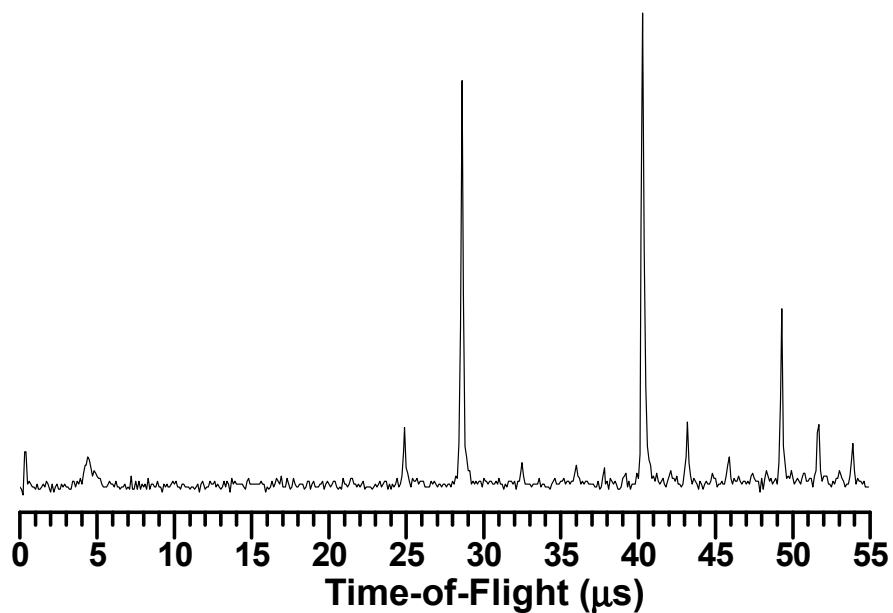


Figure 2.4: Time-of-Flight scale mass spectrum obtained using the negative ion photoelectron imaging spectrometer

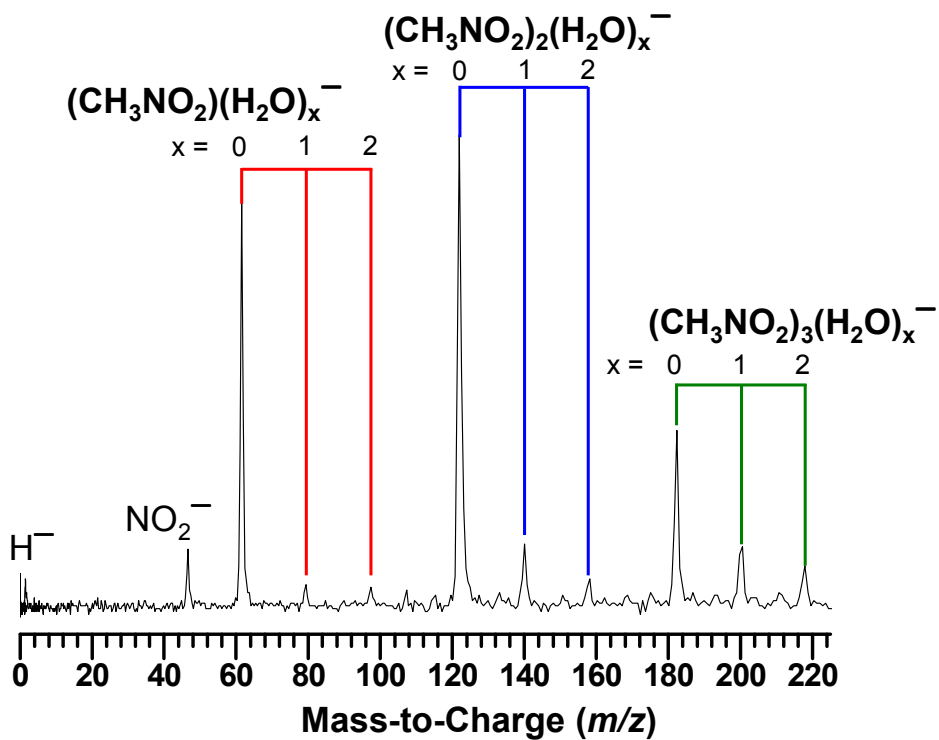


Figure 2.5: Mass-to-Charge scale mass spectrum. The spectrum in Figure 2.4 was converted to the mass-to-charge scale using Eqs. (2.5) and (2.6).

## 2.5 Laser System

A Q-switched, pulsed Nd:YAG laser system (Continuum, Surelite II-10), operating at 10 Hz with an average pulse width of 5 ns, acts as the primary light source in the imaging experiments. The fundamental wavelength, 1064 nm, of this laser can be doubled (532 nm), tripled (355 nm), or quadrupled (266 nm) using harmonic crystals (KTP). The maximum energy and power outputs for each wavelength are reported in Table 2.1. In a typical experiment ~30% of the maximum power is utilized. An optical parametric oscillator (OPO) is also available for use in imaging experiments. The OPO provides coherent, broadband radiation from 410 nm – 2,630 nm ( $\pm 5$  nm) when pumped by 355 nm light. This allows for the production of tunable radiation throughout a significant portion of the electromagnetic spectrum. The average energies for the OPO range from 5 mJ/pulse to 15 mJ/pulse.

The laser and ion beams overlap approximately 18” before the TOF-MS detector. The laser light, which is linearly polarized, is coplanar with the ion beam, and enters the apparatus perpendicular to the ion beam. Fused silica windows cut at the Brewster’s angle ( $55.5^\circ$ ) act as entrance and exit ports for the laser beam. Cutting the windows at the Brewster’s angle allows for the reduction of reflective losses at the air/glass interface. A beam dump mounted on the air side of the exit window collects the remaining light.

Table 2.1: Power and energy measurements for pulsed Nd:YAG laser used in photoelectron imaging experiments.

Wavelength (nm)	Energy (mJ/pulse)	Power (W)
1,064	630	6.3
532	310	3.1
355	180	1.8
266	100	1.0

## 2.6 Velocity Map Imaging Assembly

Photoelectrons detached from mass-selected anions are detected using the velocity-map imaging (VMI) assembly.<sup>24</sup> The current VMI stack combines the imaging technique developed by Chandler and Houston<sup>23</sup> with the VMI arrangement introduced by Parker and Eppink.<sup>24</sup> The VMI assembly, surrounded in  $\mu$ -metal, is located in the detection region of the instrument. The assembly consists of imaging plates, field-free electron flight tube, nickel mesh,  $\mu$ -metal shielding, and a position sensitive MCP detector. Oxygen-free high conductivity (OFHC) copper was used to make the three imaging plates: (1) repeller, (2) acceleration, and (3) grounding. Each plate is electrically isolated from one another by 1" PEEK insulators and measures 3" in diameter and 0.03" in thickness. The acceleration and grounding plates have 1" diameter holes in the center of the plates. The laser and ion beams overlap in the space between the repeller and acceleration plates. Negative potentials applied to the repeller plate help to accelerate photoelectrons produced from the laser and anion overlap through the center of the plates. The photoelectrons then travel through the field free electron flight tube attached to the grounding plate. The  $\mu$ -metal shielding helps protect the photoelectrons from magnetic fields. Nickel mesh is secured to the end of the field free electron flight tube to shield the photoelectrons from the potential at the front of the imaging detector. When photoelectrons strike the surface of the imaging detector, the position is recorded on a position sensitive dual chevron-type MCP attached to a P43 phosphor screen anode and fiber optic vacuum window (Burle, Inc.) The imaging detector is 40 mm in diameter. The potential applied to the first MCP is + 2 kV. The second MCP is supplied with a + 3 kV potential. The potential difference between the two MCPs is increased to  $\sim$ 2 kV using a +1 kV pulse (Directed Energy Inc., Model PVX-4150) for approximately 350 ns during the photodetachment process. This allows for noise discrimination.

The phosphor screen has a constant potential of +6.5 kV applied. Figure 2.6 is a schematic of the RC circuit used to control the potentials applied to the imaging detector. A charge-coupled device (CCD) camera (The Imaging Source, DMK 41BU02.H) captures images of the phosphor screen as the photoelectrons strike the surface of the detector. The camera has 1280 x 960 pixels and is controlled through a IEEE 1394 (FireWire) connection. Images are acquired at 10 frames per second. Approximately 30,000 laser shots are collected for a single image to produce a good signal to noise ratio. A LabVIEW program written in-house is used to compile and save the collected photoelectron images.

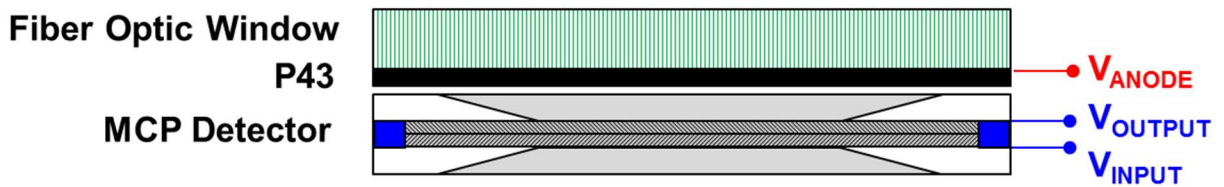
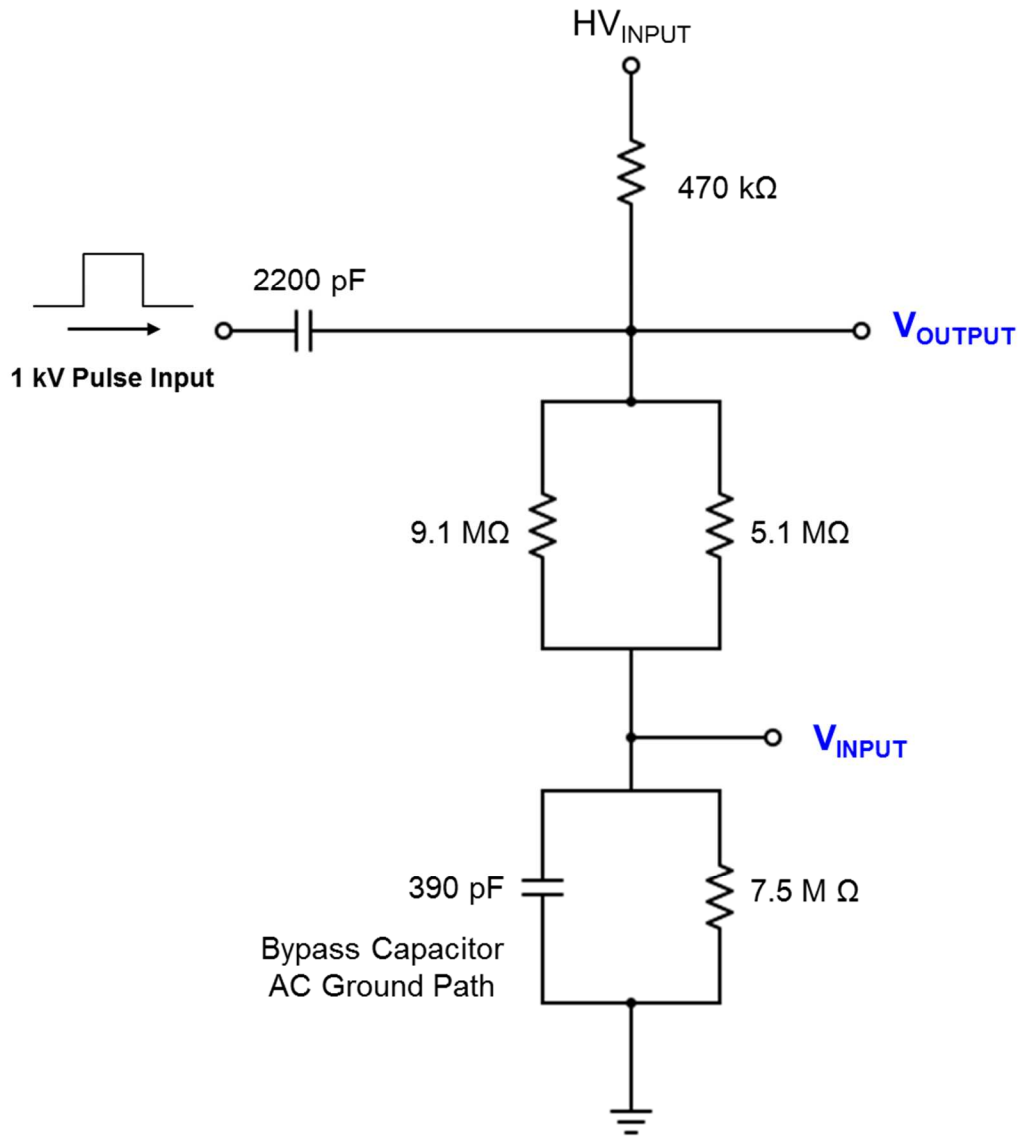


Figure 2.6: Circuit diagram of the bias network with gated gain for the imaging detector. Voltage is applied to the first MCP plate using the  $V_{INPUT}$ . Additional voltage is applied to the output of the second MCP using  $V_{OUTPUT}$ . Approximately 6.5 kV is applied to the P43 screen.

## 2.7 Triggering Sequence

The timing sequence is triggered externally from the pulse valve driver (IOTA One Valve Driver),  $T_0$ . This output is wired through a BNC connection to the input of a low jitter digital delay generator (Stanford Research Systems, Model DG645). The delay generator is used to control the rest of the timing sequence. The timing scheme for the imaging experiment is shown in Figure 2.7. The pulsed voltage applied to the TOF-MS, Channel A, is triggered  $\sim 500 \mu\text{s}$  after the rising edge of  $T_0$ . The voltage is applied to the TOF-MS plates for approximately  $330 \mu\text{s}$ . The timing of the laser Q-switch and flash lamp are controlled by Channels C and E, respectively. The flash lamp flashes  $\sim 210 \mu\text{s}$  before the Q-switch is opened. This value is held constant during an experiment, but can be adjusted to higher or lower values to change the power of the laser. The timing of the Q-switch opening is adjusted to overlap with a specific anion packet by adjusting the delay between Channels C and A. Typically, the overlap between the laser and the mass selected anions occurs  $5 - 15 \mu\text{s}$  before the anions hit the TOF-MS detector at the end of the flight tube. Good overlap between the laser and anion packet results in the detachment of electrons. Consequently, neutral molecules are also produced. The intensity of the neutral molecule signal, used to determine if there is good overlap between the laser and anions, is monitored by the TOF-MS detector. Anions are deflected by applying a negative voltage to a deflector mounted perpendicular to the TOF-MS detector. Channel G, triggered  $50 \text{ ns}$  after the rising edge of Channel C, controls the timing when the additional  $+1 \text{ kV}$  pulse is applied to the VMI stack. This is effectively the imaging time window.

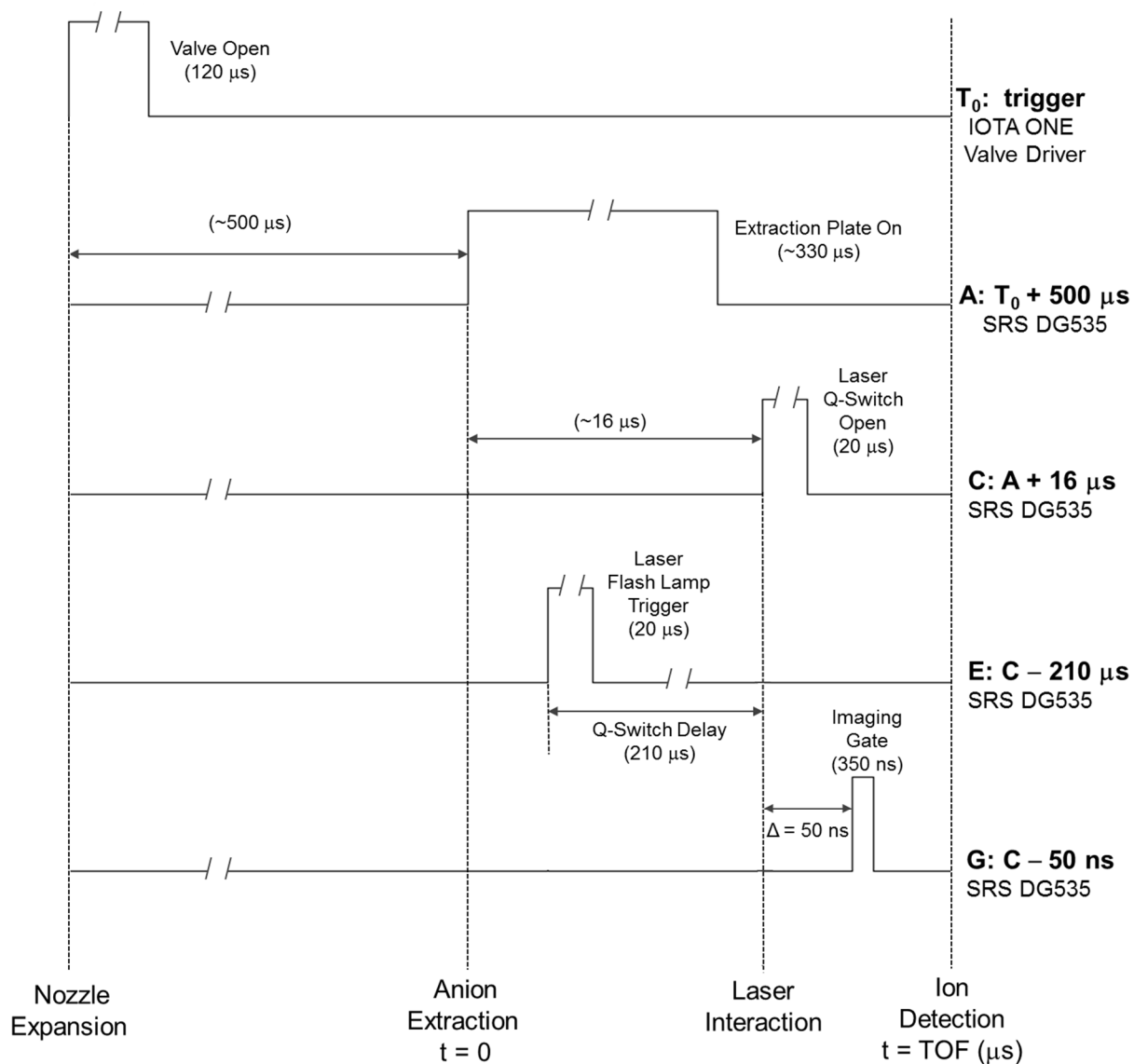


Figure 2.7: Triggering sequence for the photoelectron imaging experiment. Delay times representative of experimental values are listed. The timing sequence is initiated by the IOTA ONE valve driver,  $T_0$ . Channels A – G are controlled by the digital delay generator.

## 2.8 Analysis of Photoelectron Images

A photoelectron image is a two-dimensional (2-D) projection of the three-dimensional (3-D) probability distribution of the photoelectron. Cylindrical symmetry imposed by the linear polarization of the laser (parallel to the imaging detector surface), allow for the reconstruction of the 3-D wave using an inverse Abel transformation.<sup>28</sup> This reconstruction is carried out using the BA<sub>S</sub>is Set EX<sub>P</sub>ansion (BASEX) software developed by Dribinski *et al.*<sup>29</sup> BASEX allows for the reconstruction of the original 3-D distribution from expansion coefficients obtained by fitting the raw 2-D image with a basis set of Abel-transformed narrow Gaussian functions. The reconstructed image corresponds to a slice along the laser polarization axis through the center of the reconstructed 3-D sphere. All images in this dissertation have been reconstructed in this manner. Figure 2.8 shows the (A) projected image of O<sup>-</sup> taken at 532 nm and (B) reconstructed image.

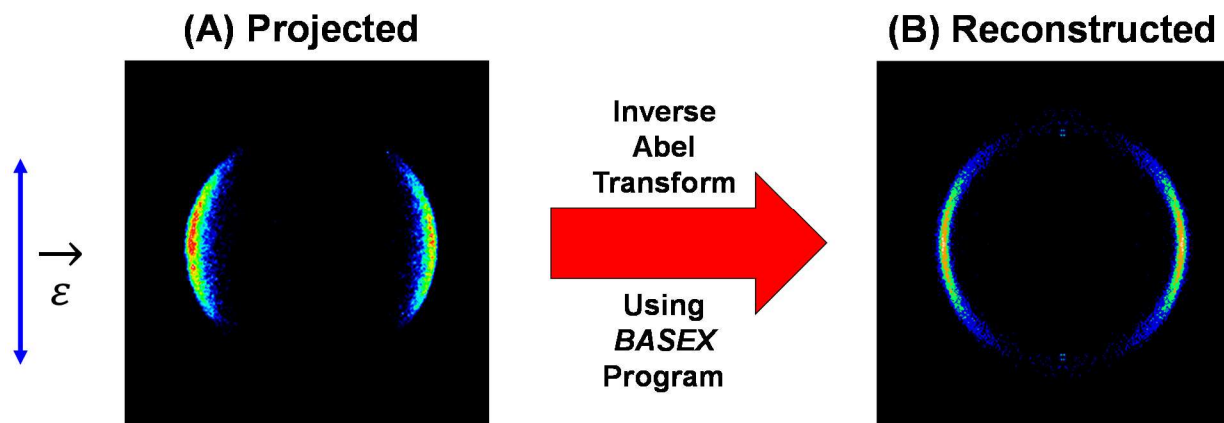


Figure 2.8: Photoelectron image of (A) O<sup>-</sup> taken at 532 nm and (B) reconstruction of projected image completed using the BASEX program. The blue arrow indicates the laser polarization axis.

Radial distributions of the detached photoelectrons can be obtained by integrating the signal intensity over the polar angle  $\theta$  at each radial coordinate,  $r$ . These intensities can be thought of as the electron velocity distribution,  $P(r)$ . The distance from the center of the reconstructed image is directly proportional to the velocity of the photoelectrons,  $v \propto r$ . The radial coordinate can then be thought of as the electron velocity in pixel scale. The electron kinetic energy,  $eKE$ , is proportional to the square of the velocity of the photoelectrons. Conversion from the velocity to energy domain is done using Eq. (2.7):

$$eKE = eKE_{cal} \frac{V}{V_{cal}} \left( \frac{r}{r_{cal}} \right)^2 \quad (2.7)$$

where  $eKE_{cal}$ ,  $v_{cal}$ , and  $r_{cal}$  are values for the electron kinetic energy, radial maximum of the corresponding peak, and pixel number from a calibration species. The value for  $eKE_{cal}$  is calculated using the energy conservation law in Eq. (2.8)

$$eKE_{cal} = hv - EA \quad (2.8)$$

where  $hv$  is the photon energy and  $EA$  is the well-known electron affinity of an atomic calibration species, e.g.  $H^-$  and  $O^-$ . Values for  $eKE$  can then be calculated for each value of  $v$  and  $r$  provided in the reconstructed image output file from the BASEX program. Eq. (2.9) shows the radial distribution,  $P(r)$ , can then be used to calculate the photoelectron energy spectra  $P(eKE)$  by utilizing a Jacobean function.

$$P(eKE) = P(r) \frac{dr}{d(eKE)} \propto P(r) \frac{1}{\sqrt{eKE}} \quad (2.9)$$

Direct comparison of data obtained at different photon energies is possible by plotting the spectra as a function of the electron binding energy, Eq. (2.10):

$$eBE = h\nu - eKE \quad (2.10)$$

where  $eBE$  is the electron binding energy,  $h\nu$  is the photon energy, and  $eKE$  is the electron kinetic energy from Eq. (2.7). A photoelectron spectrum of  $O^-$  is shown in Figure 2.9(B).

In addition to the photoelectron spectrum, photoelectron imaging provides the photoelectron angular distribution (PAD). PADs can be obtained by integrating the reconstructed image intensities over a specific radial range for each value of the polar angle  $\theta$ , measured with respect to the laser polarization axis. Typically, the limits of integration are set to the full width half maximum value for the selected peak. The values of  $\theta$  range from  $10^\circ$  to  $89^\circ$ . The general PAD expression for a one-photon detachment process from anions with a linearly polarized light is described in Eq. (2.11):

$$I(\theta) = \frac{\sigma_{tot}}{4\pi} \left[ 1 + \frac{\beta(3\cos^2\theta - 1)}{2} \right] \quad (2.11)$$

where  $I(\theta)$  is the intensity of the photoelectrons at angle  $\theta$ , which is the angle of the photoelectron velocity with respect to the laser polarization axis,  $\sigma_{tot}$  is the total photodetachment cross section, and  $\beta$  ( $-1 \leq \beta \leq 2$ ) is the anisotropy parameter.<sup>30,31</sup> For images where the intensity is at a maximum perpendicular to the laser polarization axis,  $\beta = -1$ . If the intensity of the image peaks parallel to the laser polarization axis,  $\beta = 2$ . In the event the intensity of the image is isotropic,  $\beta = 0$ . The anisotropy parameter allows for investigation of symmetry properties of the parent orbital of the photoelectron, as well as a means to acquire direct experimental evidence of the photodetachment process. The photoelectron angular distribution for  $O^-$  is shown in Figure 2.9(C).

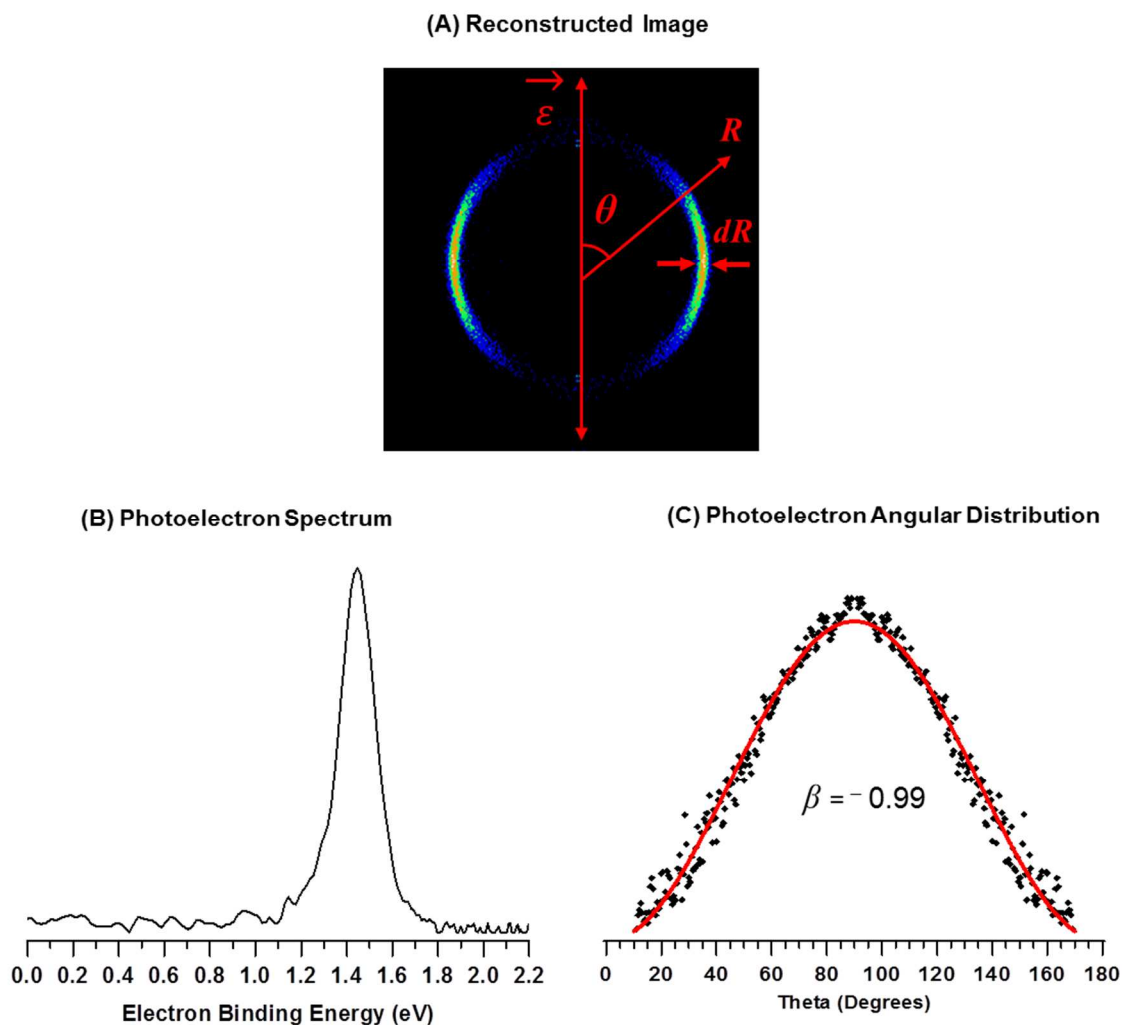


Figure 2.9: (A) Reconstructed image of  $O^-$  taken at 532 nm. (B) Photoelectron spectrum obtained from the reconstructed image. Intensity is plotted as a function of electron binding energy. (C) Photoelectron angular distribution for  $O^-$ . The black diamonds correspond to experimental data. The red line is a fit to Eq. (2.11). The anisotropy parameter ( $\beta$ ) was determined from the fit to Eq. (2.11).

## 2.9 Mass Spectrometry

### *2.9.1 Experimental Overview*

The experiments described in Chapters 5 – 7 were performed using a triple quadrupole mass spectrometer (Finnigan TSQ 7000). A solution containing the analyte of interest is pumped by a syringe pump at approximately 4  $\mu\text{L}/\text{min}$  into the ionization source. Ions created in the source region are sampled by a heated capillary (200°C). The capillary acts as a barrier between the atmospheric pressure and the first differentially pumped vacuum region (700 mTorr). A tube lens and skimmer focus the ion beam before it enters the second differentially pumped vacuum region (1 mTorr). Electrostatic lenses collimate the ion beam before the beam enters the high vacuum region, which contains the analyzer assembly. Once the ions are in the analyzer assembly various modes of operation are employed to investigate the anions.

### *2.9.2 Instrumental Overview*

The instrumental schematic is shown in Figure 2.10. The triple quadrupole mass spectrometer is composed of an ion source, analyzer assembly, and ion detection system all housed in a vacuum manifold pumped by two turbo molecular pumps (TMP) and a rotary-vane pump. Both electrospray ionization (ESI)<sup>32</sup> and atmospheric pressure chemical ionization (APCI)<sup>33</sup> sources were used in the experiments described in this dissertation.

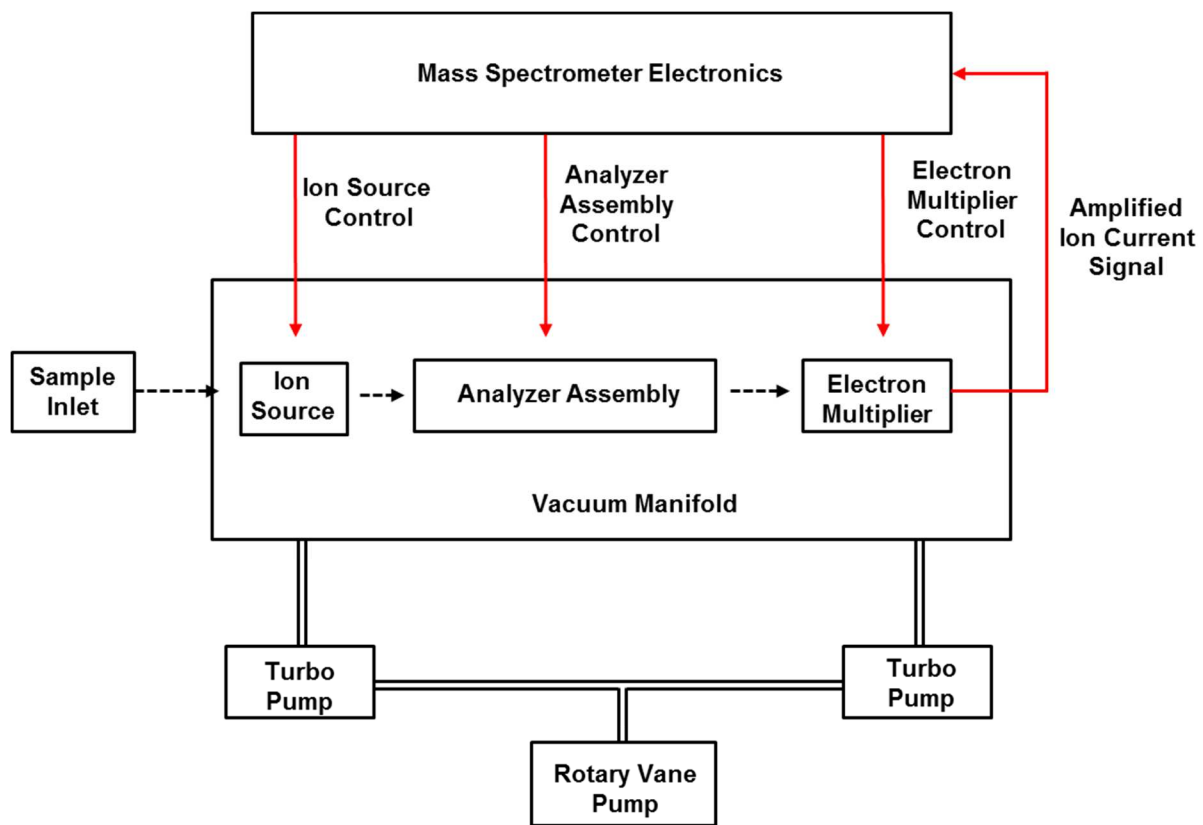


Figure 2.10: Instrumental schematic of the triple quadrupole mass spectrometer (Finnigan, TSQ 7000) used in Chapters 5 – 7.

### 2.9.3 Ion Sources

A schematic of the ESI source is shown in Figure 2.11. The main components of the source are the spray needle and nose cone. A syringe pump (New Era Pump Systems, Inc.) is used to deliver a continuous flow ( $4 \mu\text{L}/\text{min}$ ) of solution containing the analyte through the electrospray needle. Anions are generated by applying a voltage ( $\sim -4 \text{ kV}$ ) to the stainless steel electrospray needle relative to the nose cone. A transfer capillary transports the anions from a region at atmospheric pressure to a region under high vacuum conditions. Nitrogen sheath gas transfers the anions from solution to the gas phase. A skimmer collimates the ion beam before it enters the analyzer assembly. Figure 2.12 shows a more detailed look at the anion formation process. The potential difference created by the voltages applied to the spray needle and nose cone generates an electric field. This electric field creates excess negative charge at the needle surface. The meniscus of the solution flowing through the needle is deformed as a result of the electric field, causing the meniscus to emerge from the spray needle. This is referred to as the Taylor cone.<sup>34</sup> Droplets containing the analyte of interest are generated with an excess charge and emitted in a jet from the Taylor cone. As the droplets move toward the nose cone solvent evaporation occurs. This results in an increase in the surface charge of the droplets. Smaller “offspring” drops are produced through a Coulombic explosion of the larger surface charged droplets. Free analyte molecules evaporate from the surface of the offspring drops in a similar fashion. These free analyte molecules then pass through the nose cone of the instrument and continue into the analyzer assembly.

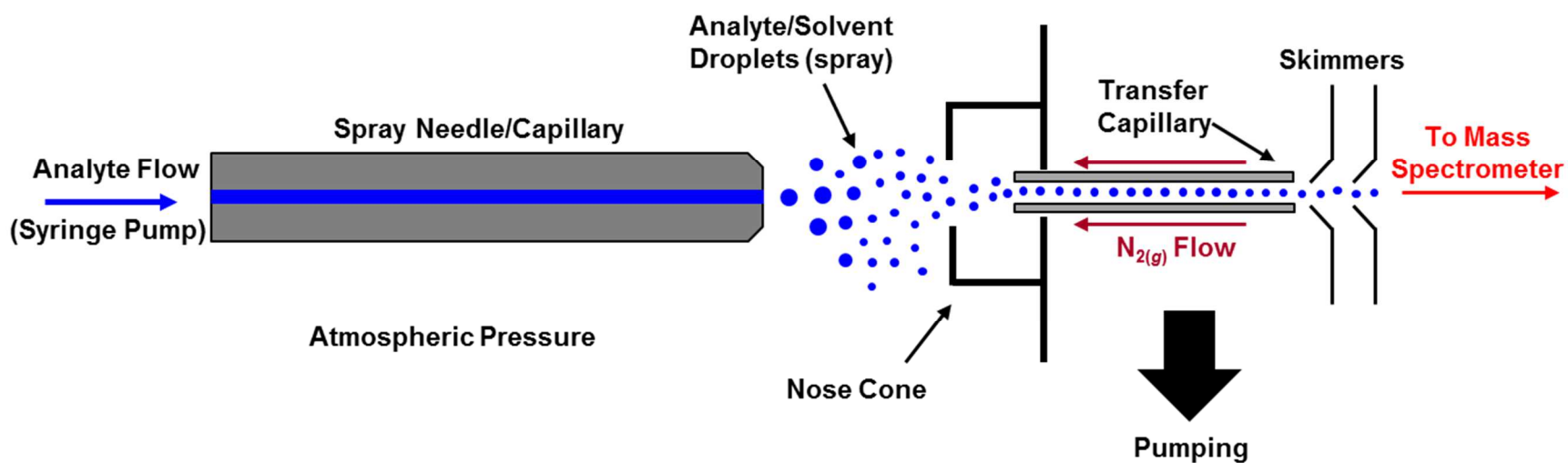


Figure 2.11: Schematic of electro spray ionization (ESI) source utilized in Chapter 7.

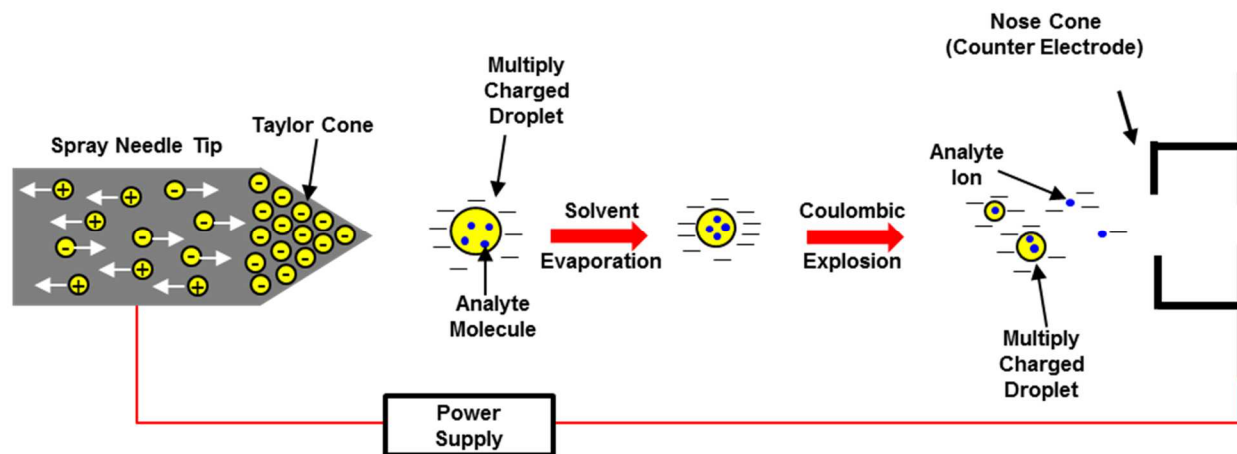


Figure 2.12: Schematic of the mechanism of anion formation for the ESI source.

A schematic of the APCI source is shown in Figure 2.13. The APCI source is made of a sheath gas tube, vaporizer heater block, and corona discharge needle. A solution containing the analyte is introduced into the source through a syringe pump. The solution is vaporized by the heater block. A specific current is applied to the corona discharge needle. Anions are formed from the solution passing through the cloud of electrons emitted from the tip of the discharge needle. A skimmer collimates the ion beam before it enters the analyzer assembly. Figure 2.14 provides a more in depth look at the anion formation mechanism for the APCI source. Electrons are emitted from the corona discharge needle and interact with reagent gases. These gases are ionized, creating a plasma. When the analyte of interest encounters the reagent gas plasma, anion formation occurs as a result of ion-molecule reactions.

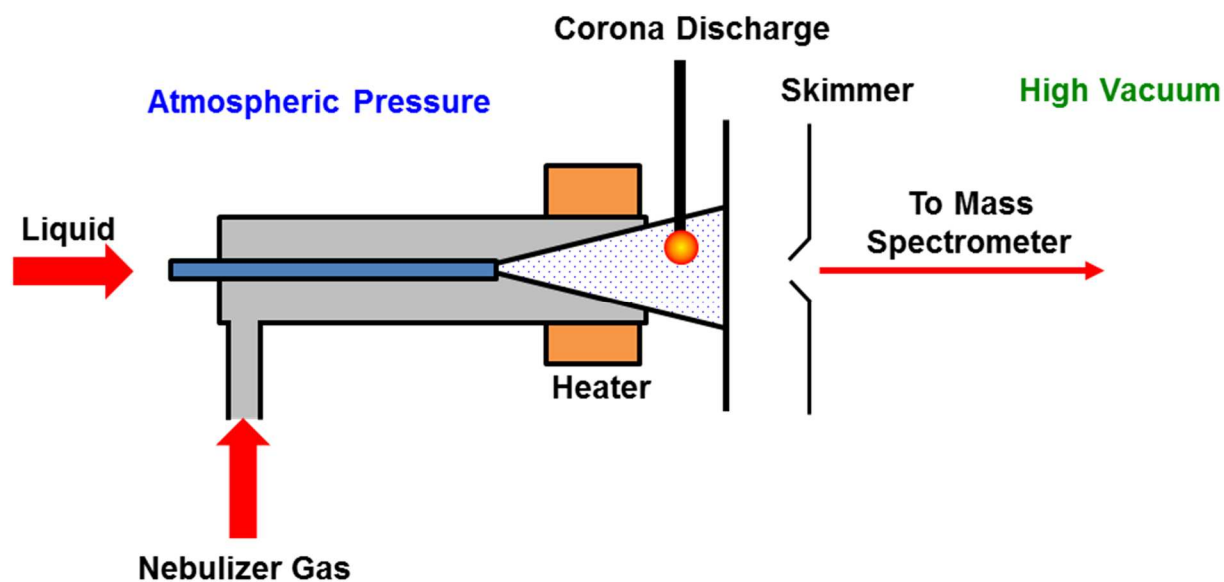


Figure 2.13: Schematic of the atmospheric pressure chemical ionization (APCI) source used in Chapters 5 and 6.

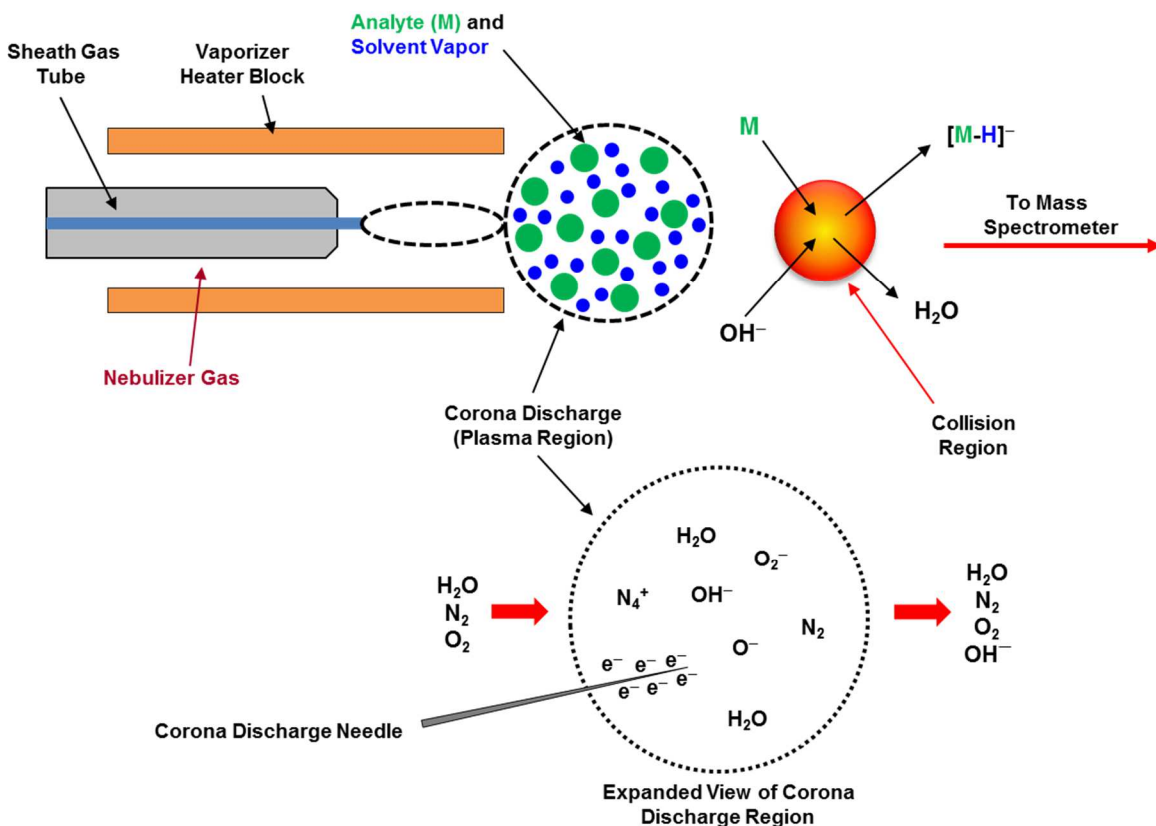


Figure 2.14: Schematic of anion formation mechanism using the APCI source.

#### 2.9.4 Analyzer Assembly

Figure 2.15 contains a schematic of the analyzer assembly. The analyzer assembly houses two quadrupole rod assemblies (Q1 and Q3), one octapole (Q2) assembly, and three electrostatic lenses. Each quadrupole consists of four metal rods placed precisely parallel to one another in a square array. The rods in the quadrupole are charged with a variable ratio of radio frequency (RF) voltages and direct current (DC) voltages. An electrostatic field produced by these potentials allows for stable oscillations of ions with a specific mass-to-charge ( $m/z$ ) ratio. Ions outside of this specific  $m/z$  ratio undergo unstable collisions. These ions strike the surface of one of the rods and are ejected from the rod assembly, or become neutralized, and are pumped away.

This allows Q1 and Q3 to act as either mass analyzers or ion transmission guides. Q2, the collision cell, is an octagonal array of cylindrical rods which only functions as an ion transmission guide. A variable RF voltage is applied to the rods of Q2, resulting in stable oscillations for a wide range of  $m/z$  ratios, allowing a range of ions to be transmitted into Q3. Three lens sets are axially aligned with the rod assemblies of the analyzers. Each lens set is held in cylindrical couplers, with each lens isolated from one another by anodized aluminum spacers. Q1 and Q2 are separated by lens set L2. Lens set L3 separates Q2 from Q3. The ion detection system is isolated from Q3 by lens set L4. Lenses from L2 and L3 provide two of the walls of the collision cell. These lenses help prevent the collision gas from exiting the collision cell and entering Q1 or Q3. The lenses also help to shield each mass analyzer from the RF voltages applied to adjacent analyzers. Additionally, the lenses help to focus the ion beam as it is transmitted into the different regions of the instrument. The ion detection system consists of a channeltron electron multiplier and a gold-plated glass ground shield. When the ions strike the surface of the electron multiplier secondary charged particles are emitted. These secondary particles strike the cathode of the electron multiplier with sufficient kinetic energy to generate a cascade of electrons. This results in a measurable current at the anode of the electron multiplier where the ions are detected.

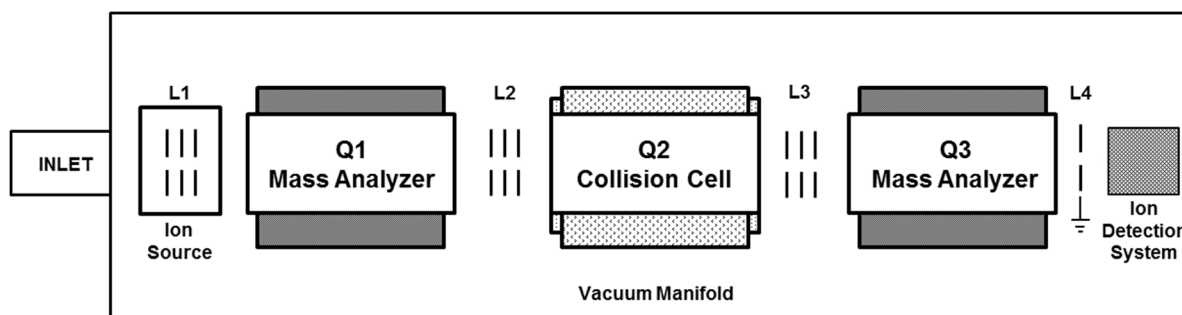


Figure 2.15: Analyzer assembly for triple quadrupole mass spectrometer. Q1 and Q3 are quadrupole mass analyzers. Q2 is an octapole collision cell. Electrostatic lenses are labeled L1, L2, L3, and L4.

## 2.10 Modes of Operation

### *2.10.1 QIMS*

Q1 acts as the primary ion guide. The voltages applied to Q1 are scanned to allow ions within a specific range of  $m/z$  ratios to transmit through to the other analyzers. Q2 and Q3 act as ion guides. Ions formed in the source are detected by the detector. Major peaks identified in a QIMS scan are then selected for study using collision induced dissociation and energy-resolved mass spectrometry.

### *2.10.2 Collision Induced Dissociation*

Collision induced dissociation (CID) experiments are carried out on all major peaks identified in a QIMS scan. A fixed voltage is applied to Q1 to mass select a specific precursor ion. Q2 acts as a collision cell. An inert collision gas, normally Ar, is introduced into Q2 at a constant pressure, approximately 0.5 mTorr for the experiments reported in this dissertation. When the mass selected precursor enters Q2, collisions between the ion and the inert gas induce ion fragmentation. The fragment ions from these collisions are monitored by Q3. The resulting CID spectrum shows all fragments formed from the dissociation of the selected precursor. Fragments observed in the dissociation of the precursor ion can be further investigated using energy-resolved mass spectrometry.

### *2.10.3 Energy Resolved Mass Spectrometry*

Energy resolved mass spectrometry (ERMS) is used to determine thermochemical data for precursor and fragment ions identified in CID studies. Fixed voltages are applied to Q1 and Q3 to mass select specific precursor and fragment  $m/z$  ratios, respectively. Q2 is pressurized to ~0.15 mTorr with Ar gas. The collision voltage applied to Q2 is scanned. The intensity of the fragment is monitored as a function of the collision cell voltage. The appearance energy is

indicated by the lowest energy at which the fragment is produced. This can then be related to the bond dissociation energy for the ion.<sup>35</sup>

The absolute zero kinetic energy of the precursor ion is determined using a retarding potential analysis.<sup>36</sup> The derivative of the transmission curve is plotted and used to correct for the collision energy of the ions in the laboratory frame. For the studies reported in this dissertation the collision offset ranged from 0.25 eV to 2.25 eV. The laboratory energies are converted to the center-of-mass frame using Eq. (2.12):

$$E_{CM} = E_{LAB} \left( \frac{m}{m + M} \right) \quad (2.12)$$

where  $E_{CM}$  is the center-of-mass energy,  $E_{LAB}$  is the corrected laboratory collision energy,  $m$  is the mass of the target gas, and  $M$  is the mass of the precursor ion. This conversion is required to provide a suitable energy scale for thermodynamic analysis.

## CHAPTER 3

### PHOTOELECTRON ANGULAR DISTRIBUTIONS OF CH<sup>-</sup>

#### 3.1 Introduction

The CH radical is a small molecule of great importance in stellar atmospheres,<sup>37</sup> the interstellar medium,<sup>38-40</sup> and combustion.<sup>41,42</sup> The radical nature of CH provides an interesting electronic structure. Photoelectron imaging is a valuable technique to investigate the electronic structure of radical species by performing photodetachment experiments on the anion. Previous photoelectron spectroscopy studies on CH<sup>-</sup> have been limited and inconsistent.<sup>43-45</sup> Feldman reported a photoelectron spectrum measured in the range of 0.5 eV to 2.0 eV with thresholds at 0.74 eV and 1.95 eV.<sup>43</sup> The photoelectron spectrum recorded by Kasdan showed three transitions at electron binding energies of 0.393 eV, 1.238 eV, and 1.980 eV.<sup>44</sup> The peak at 1.238 eV was assigned to the  $X^2\Pi \leftarrow X^3\Sigma^-$  transition. This transition occurred from detachment of one of the unpaired  $\pi$  electrons in the ground state of CH<sup>-</sup>. The  $a^4\Sigma^- \leftarrow X^3\Sigma^-$  transition was assigned to the feature at 1.980 eV. The  $a^4\Sigma^-$  state was produced as a result of electron detachment from the non-bonding  $3\sigma$  orbital of CH<sup>-</sup>. The band at 0.393 eV was attributed to electron detachment from the excited state anion,  $X^2\Pi \leftarrow a^1\Delta$ .<sup>44</sup> This is a particularly interesting assignment because it implies a long live metastable anion. Work by Okumura is in agreement with the results of Kasdan.<sup>45</sup> Our group carried out additional experiments on CH<sup>-</sup> to probe the low lying electronic states of the anion.<sup>46</sup> The experiments carried out in this chapter were part of the first study completed using the photoelectron imaging spectrometer.

## 3.2 Methods

All experiments were carried out using the photoelectron imaging spectrometer described in Chapter 2. Anions were generated by a DC discharge source made of two closely spaced metallic electrodes. The discharge conditions were optimized to atomize the gases in the expansion. Small atomic and diatomic species including  $\text{H}^-$ ,  $\text{CH}^-$ ,  $\text{O}^-$ ,  $\text{OH}^-$ ,  $\text{C}_2^-$  and  $\text{C}_2\text{H}^-$  were generated in the discharge source. It is important to note many organic gases produce  $\text{CH}^-$  in our source, but the high vapor pressure of nitromethane creates a stable anion signal. Anions were detected using the TOF-MS. Approximately 2 m downstream from the source region the anions interact with a beam of photons in the velocity map imaging<sup>24</sup> assembly. Photoelectrons were detected using the CCD camera and position sensitive imaging detector.

Photons were generated from a pulsed Nd:YAG laser. Frequency doubling and tripling of the fundamental wavelength of the laser to produced 532 nm and 355 nm photons. An optical parametric oscillator (OPO) was pumped at 355 nm to produce tunable radiation. In this experiment, photoelectron images were collected from 410 nm to 600 nm in 25 nm steps, 532 nm, and 355 nm. The average photon energy ranged from 5 mJ/pulse to 15 mJ/pulse. The photoelectron spectra were calibrated using  $\text{O}^{\bullet-}$ .<sup>47,48</sup> Approximately 15,000 laser shots were collected for each image. The analysis procedure outlined in Chapter 2 was utilized to analyze the photoelectron images.

## 3.3 Results and Discussion

### *3.3.1 Photoelectron Spectra*

Figure 3.1 shows representative photoelectron images of  $\text{CH}^-$  collected at 532 nm. The image on the left is the uncorrected raw image, whereas the Abel-inverted image is on the right.

Each image was treated independently. Two features, an intense outer band and a weaker inner band, appear in every image. Using the methods described in Chapter 2, the photoelectron spectra were extracted from each Abel-inverted image. Figure 3.1 contains a representative photoelectron spectrum plotted in the electron binding energy, eBE, scale. This ensures all features appear at the same energy regardless of the photon energy. The most intense feature corresponds to the  $X^2\Pi \leftarrow X^3\Sigma^-$  transition.<sup>49</sup> This represents electron detachment from the  $1\pi$  orbital. The electron binding energy of this peak is  $1.26 \pm 0.02$  eV at 532 nm. The weaker feature is assigned to the  $^4\Sigma^- \leftarrow X^3\Sigma^-$  transition. This corresponds to detachment from the  $3\sigma$  orbital of  $\text{CH}^-$ . The electron binding energy for this peak is  $1.98 \pm 0.02$  eV at 532 nm. The doublet-quartet splitting is  $0.72 \pm 0.03$  eV at 532 nm. This value is in good agreement with a reported value of  $0.742 \pm 0.008$  eV by Lineberger.<sup>44</sup>

Detachment from the excited anion state  $a^1\Delta$  was previously measured at 0.393 eV.<sup>44</sup> We did not observe this band. This could be a result of the ionization source. It is possible the discharge source utilized in our experiment does not generate a sufficient population of anions in the  $a^1\Delta$  excited state. It is also possible the anions relax before photodetachment. However, previous work on trapped  $\text{CH}^-$  reported a lifetime of  $5.9 +0.8/-0.6$  s, therefore if anions are generated in the  $a^1\Delta$  excited state the anions should be observed in our experiment.<sup>45</sup>

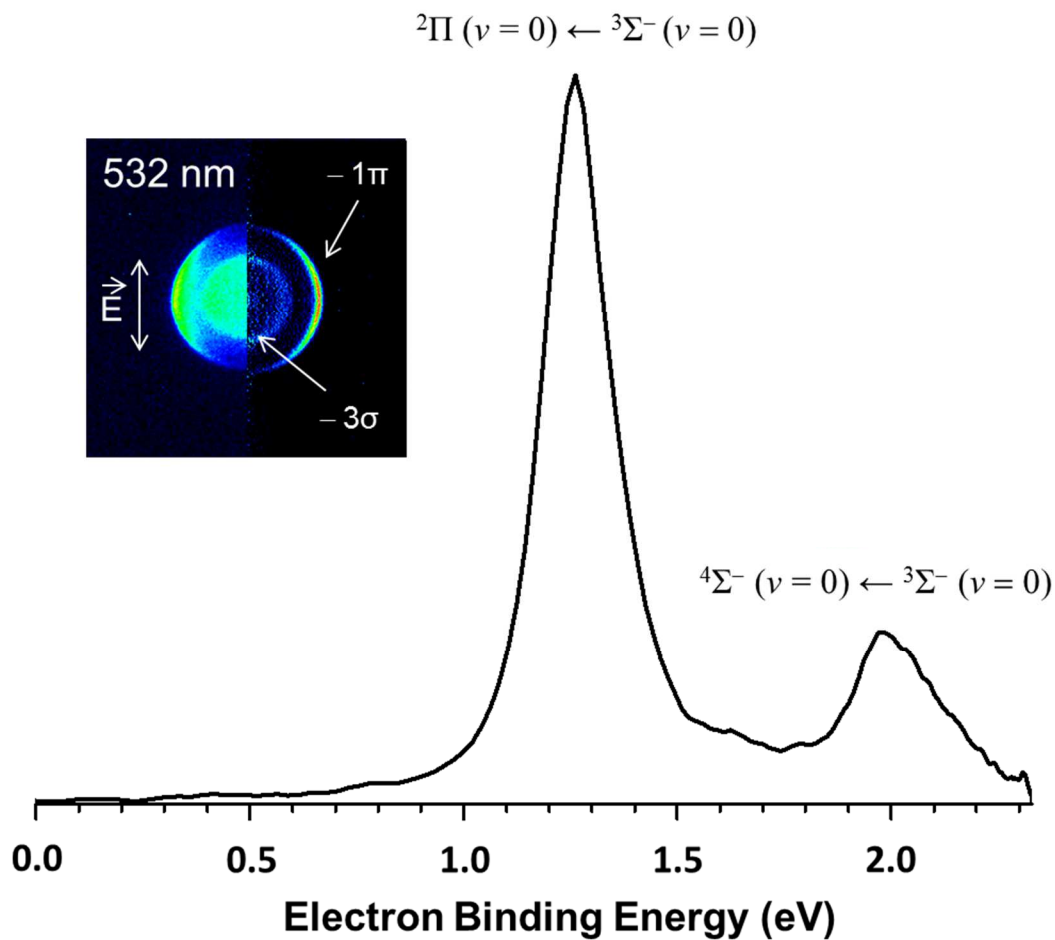


Figure 6.1: Representative photoelectron image and photoelectron spectrum of  $\text{CH}^-$  measured at 532 nm. The spectrum is plotted in terms of the electron binding energy obtained by subtracting the electron kinetic energy from the photon energy.

### 3.3.2 Photoelectron Angular Distributions

Figure 3.2 shows the anisotropy values extracted from the photoelectron images collected for this study as a function of electron kinetic energy. Photodetachment from the  $1\pi$  orbital (red diamonds) produces negative values for  $\beta$ . As the electron kinetic energy increases the anisotropy parameter becomes less negative for detachment from the  $1\pi$  orbital. Figure 3.2 shows there is no general trend for detachment from the  $3\sigma$  orbital (blue circles) of  $\text{CH}^-$ . The anisotropy parameter ranges from 0.02 for an electron kinetic energy of 0.499 eV to -0.51 for an electron kinetic energy of 1.512 eV for detachment from the  $3\sigma$  orbital.

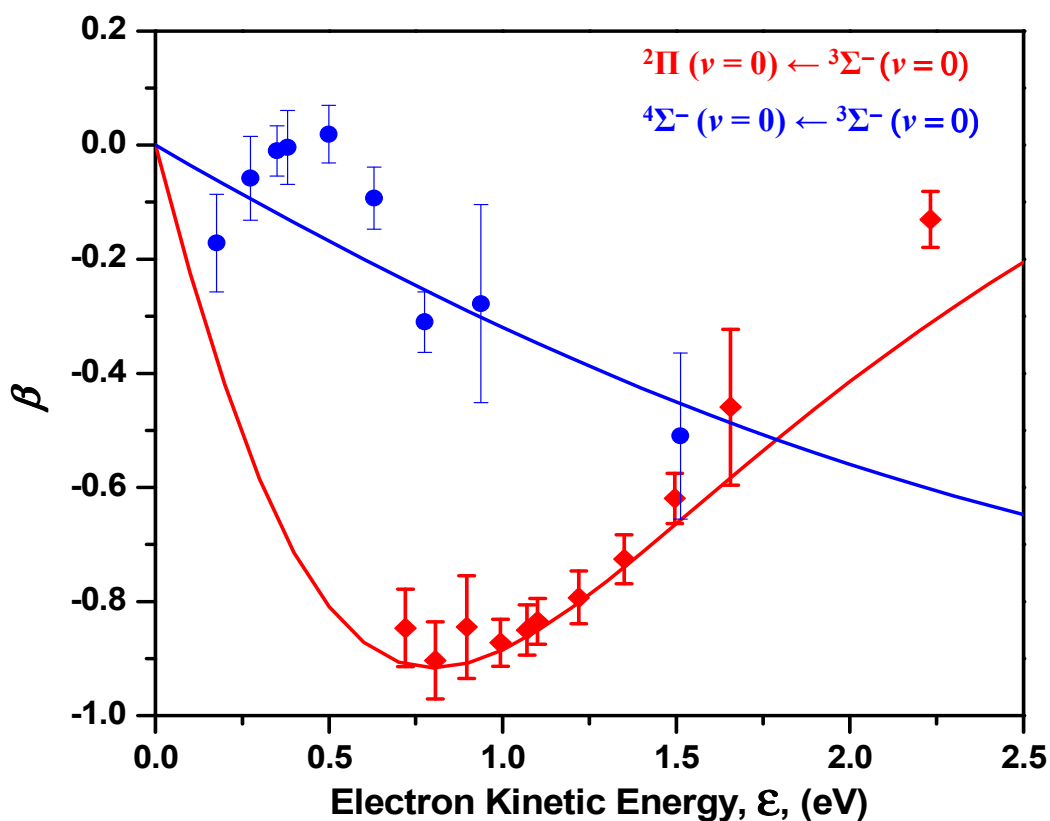


Figure 3.2: Photoelectron angular distributions as a function of electron kinetic energy for the  ${}^2\Pi \leftarrow {}^3\Sigma^-$  (red diamonds) and  ${}^4\Sigma^- \leftarrow {}^3\Sigma^-$  (blue dots) transitions. The solid lines are fits to each data set using Eq. 3.7. The fractional  $p$  character is  $f = 0.95$  for the  ${}^2\Pi \leftarrow {}^3\Sigma^-$  transition and  $f = 0.99$  for the  ${}^4\Sigma^- \leftarrow {}^3\Sigma^-$  data but considered unreliable.

The first approach used to analyze the angular distributions is a qualitative method called the  $s$  and  $p$  model.<sup>25,50</sup> The  $s$  and  $p$  model uses group theory to identify all dipole allowed partial wave contributions to the outgoing photoelectron. This approach is based on three approximations. The first approximation requires the outgoing photoelectron is restricted to  $s$  and  $p$  partial waves. This is expressed in Eq. (3.1)

$$\Psi_{free} \approx s + p_x + p_y + p_z \quad (3.1)$$

where  $\Psi_{free}$  is the wave function of the free outgoing electron wave and the different atomic orbitals are represented by  $s$ ,  $p_x$ ,  $p_y$ , and  $p_z$ . The second approximation accounts for orientation averaging by only considering three principle orientations (x, y, and z) for the molecular anion. The molecular frame of the anions is linked to the laboratory frame by aligning each molecular frame orientation with the laboratory frame. The third approximation is used for determining the allowed characters of the emitted partial waves. The character of the partial waves are determined by evaluating the non-zero matrix elements of the transition dipole moment matrix for each principal orientation. This can be done by implementing group theory. Specifically, the non-zero elements can be determined by requiring the direct product of the irreducible representations of the bound electron, the dipole moment operator, and the free electron wave must contain the totally symmetric irreducible representation of the anion point group. This relationship is expressed in Eq. (3.2)

$$\Gamma(\Psi_{free}) \otimes \Gamma(\hat{\mu}) \otimes \Gamma(\Psi_{bound}) \supseteq \Gamma_{TS} \quad (3.2)$$

where  $\Gamma(\Psi_{free})$  is the irreducible representation of the free electron wave,  $\Gamma(\hat{\mu})$  is the irreducible representation of the dipole moment,  $\Gamma(\Psi_{bound})$  is the irreducible representation of the bound electron wave, and  $\Gamma_{TS}$  is the totally symmetric irreducible representation of the anion point group.

The  $\text{CH}^-$  molecule is a member of the  $C_{\infty v}$  point group. According to the  $C_{\infty v}$  character table and the approximations of the  $s$  and  $p$  model, the orbital of  $\Psi_{bound}$  must be of character  $\Sigma^+$  or  $\Pi$ . Table 3.1 contains the partial waves allowed if  $\Psi_{bound}$  is assumed to have  $\Pi$  character and the dipole-moment is treated independently in each principle direction. The predicted magnitude of  $\beta$  is also included in Table 3.1. The experimental PAD show the greatest photoelectron intensity is perpendicular to the laser polarization axis. This corresponds to a negative value for  $\beta$ . The sign of the  $\beta$  values predicted from the group theory and symmetry approach are in good agreement with the experimental values.

Table 3.1: Allowed free-electron symmetries for detachment from  $\Psi_{bound}$  orbital with  $\Pi$  character within the  $C_{\infty v}$  point group.

Direct Product	Laboratory Frame	$\beta$
$\Psi_{bound} \otimes \widehat{\mu}_z$		
$\Pi \otimes \Sigma^+$	$p_x + p_y$	$\beta < 0$
$\Psi_{bound} \otimes \widehat{\mu}_y$		
$\Pi \otimes \Pi$	$p_y$	$\beta < 0$
$\Psi_{bound} \otimes \widehat{\mu}_x$		
$\Pi \otimes \Pi$	$p_x$	$\beta < 0$

Table 3.2 contains the partial wave contributions allowed from the final results of the direct product if  $\Psi_{bound}$  is assumed to have  $\Sigma^+$  character and the dipole moment is treated independently in each principle direction ( $x$ ,  $y$ , and  $z$ ). In order to satisfy Eq. (3.2),  $\Psi_{free}$  must consist of the orbitals listed in Table 3.2. The predicted sign of  $\beta$  is also reported in Table 3.2.

This implies the angular distribution is expected to be greatest parallel to the laser polarization axis. This corresponds to a positive value for  $\beta$ .

The PADs corresponding to detachment from the  $3\sigma$  orbital show predominantly isotropic character at low electron kinetic energies and more perpendicular character at higher electron kinetic energies. This does not agree with the predicted sign of  $\beta$  from the  $s$  and  $p$  model. This is due to the low symmetry of the  $C_{\infty v}$  point group. This limitation of the symmetry-based has been demonstrated in previous work.<sup>51</sup> The failure of the  $s$  and  $p$  model to correctly predict the sign of  $\beta$  in the case of detachment from the  $3\sigma$  orbital demonstrates the need for another approach to analyze PADs.

Table 3.4: Allowed free-electron symmetries for detachment from  $\Psi_{bound}$  orbital with  $\Sigma^+$  character within the  $C_{\infty v}$  point group.

Direct Product	Laboratory Frame	$\beta$
$\Psi_{bound} \otimes \widehat{\mu}_z$		
$\Sigma^+ \otimes \Sigma^+$	$s + p_z$	$\beta > 0$
$\Psi_{bound} \otimes \widehat{\mu}_y$		
$\Sigma^+ \otimes \Pi$	$p_z$	$\beta > 0$
$\Psi_{bound} \otimes \widehat{\mu}_x$		
$\Sigma^+ \otimes \Pi$	$p_z$	$\beta > 0$

A more quantitative approach for analyzing PADs involves calculating  $\beta$  as a function of the electron kinetic energy.<sup>30,31,52</sup> This approach is based on the Bethe-Cooper-Zare equation, Eq.

(3.3)

$$\beta = \frac{l(l-1)\chi_{l,l-1}^2 + (l+1)(l+2)\chi_{l,l+2}^2 - 6l(l+1)\chi_{l,l+1}\chi_{l,l-1} \cos(\delta_{l+1} - \delta_{l-1})}{2l+1[l\chi_{l,l-1}^2 + (l+1)\chi_{l,l+1}^2]} \quad (3.3)$$

where  $l$  is the atomic orbital angular momentum quantum number,  $\chi_{l,l-1}^2$  are radial matrix elements for the  $l_f = l_i \pm 1$  dipole allowed free electron partial waves of the outgoing photoelectron, and  $\cos(\delta_{l+1} - \delta_{l-1})$  is the phase shift induced by interaction with the remaining neutral species.<sup>52</sup> It is important to note, the anisotropy parameter is not expressed as a function of the electron kinetic energy in the Bethe-Cooper-Zare equation. Applying the Wigner threshold law for anion photodetachment,  $\sigma_l \propto \varepsilon^{l+1/2}$ , to the Bethe-Cooper-Zare equation allows for the anisotropy parameter to be expressed as a function of electron kinetic energy by assuming  $\frac{\sigma_{l+1}}{\sigma_{l-1}} \propto \varepsilon^2$  and therefore  $\frac{\chi_{l,l+1}^{l_i, l_i+1}}{\chi_{l,l-1}^{l_i, l_i-1}} \propto A\varepsilon$ . This restatement of Eq. (3.3) is known as the Wigner-Bethe-Cooper-Zare equation, Eq. (3.4)

$$\beta(\varepsilon) = \frac{l_i(l_i-1) + (l_i+1)(l_i+2)A^2\varepsilon^2 - 6l_i(l_i+1)A\varepsilon \cos(\delta_{l_i+1} - \delta_{l_i-1})}{(2l_i+1)[l_i + (l_i+1)A^2\varepsilon^2]} \quad (3.4)$$

where  $\varepsilon$  is the electron kinetic energy and  $A$  is a proportionality coefficient.<sup>53</sup> However, the dependence of Eq. (3.4) on  $l$  means the equation is not appropriate for calculating  $\beta$  for non-atomic species. Therefore, the PADs obtained from imaging experiments on  $\text{CH}^-$  cannot be analyzed with Eq. (3.4). However, it is possible to analyze the PADs in this chapter using the mixed  $sp$  model.<sup>54</sup>

Grumblin *et al.* derived the mixed  $sp$  model based on Eq. (3.4) to describe photodetachment from a stationary state made of a linear combination of one  $s$  and one  $p$  type functions.<sup>54</sup> This is expressed in Eq. (3.5)

$$|\psi_{bound}\rangle = \sqrt{1-f}|s\rangle + \sqrt{f}|p\rangle \quad (3.5)$$

where  $f$  is the fractional  $p$  character ranging from  $0 \leq f \leq 1$ . The dipole selection rules require the  $s$  portion of the linear combination produce  $p$  partial waves as a result of photodetachment. The  $p$  component of the linear combination produces  $s$  and  $d$  partial waves. In this model the PAD can be described using the spherical harmonics for the partial waves, Eq. (3.6)

$$I(\theta) = |\Psi(\theta)|^2 = \left| \sqrt{f} e^{i\delta_0} C_0 Y_{00}(\theta) + \sqrt{f} e^{i(\delta_2+\pi)} C_2 Y_{20}(\theta) \right|^2 + 3 \left| \sqrt{1-f} e^{i(\delta_1+\pi/2)} C_1 Y_{10}(\theta) \right|^2 + [d_{xz}, d_{yz} \text{ terms}] \quad (3.6)$$

where  $Y_{lm}$  represent the spherical harmonics and  $C$  represents the coefficients for the partial waves. A new expression for the photoelectron angular distribution can be written by arbitrarily defining the spherical harmonics as unnormalized functions ( $Y_{00} = 1$ ;  $Y_{10} = \cos \theta$ ;  $Y_{20} = 3\cos^2\theta - 1$ ) and including the necessary normalization constants in the coefficients. Using this approach, the photoelectron angular distribution intensity at  $0^\circ$  is expressed in Eq. (3.7)

$$I(0^\circ) = fC_0^2 + 3(1-f)C_1^2 + 4fC_2^2 - 4fC_0C_2\cos(\delta_2 - \delta_0) \quad (3.7)$$

and Eq. (3.8) is the angular distribution intensity at  $90^\circ$ .

$$I(90^\circ) = fC_0^2 + fC_2^2 + 2fC_0C_2\cos(\delta_2 - \delta_0) \quad (3.8)$$

Given Eqs. (3.7) and (3.8), it is possible to obtain an expression for the anisotropy parameter by substituting Eqs. (3.7) and (3.8) into Eq. (3.9) and dividing by  $C_0^2$

$$\beta = \frac{\rho - 1}{1 + \rho/2} \quad (3.9)$$

where  $\rho = \frac{I(0^\circ)}{I(90^\circ)}$ . This new expression is given in Eq. (3.10).

$$\beta = \frac{2(1-f)\left(\frac{C_1}{C_0}\right)^2 + 2f\left(\frac{C_2}{C_0}\right)^2 - 4f\left(\frac{C_2}{C_0}\right)\cos(\delta_2 - \delta_0)}{f + 2f\left(\frac{C_2}{C_0}\right)^2 + (1-f)\left(\frac{C_1}{C_0}\right)^2} \quad (3.10)$$

Application of the Wigner threshold law allows for the ratio of coefficients to be restated as shown in Eqs. (3.11a) and (3.11b)

$$\frac{C_1^2}{C_0^2} = \frac{\chi_{0,1}^2}{\chi_{1,0}^2} = \frac{\sigma_1}{\sigma_0} = B\varepsilon \quad (3.11a)$$

$$\frac{C_2^2}{C_0^2} = \frac{\chi_{1,2}^2}{\chi_{1,0}^2} = \frac{\sigma_2}{\sigma_0} = A^2\varepsilon^2 \quad (3.11b)$$

where  $\sigma$  is the partial cross section and  $A$  and  $B$  are constants. The constants  $A$  and  $B$  are inversely related to the size of the bound orbital.<sup>55</sup> The terms  $B\varepsilon$  and  $A^2\varepsilon^2$  can be substituted into Eq. (3.10) to provide a way to predict  $\beta$  as a function of electron kinetic energy for one-electron photodetachment from an orbital of mixed  $sp$  character. This new equation is described in Eq. (3.12).

$$\beta = \frac{2(1-f)B\varepsilon + 2fA^2\varepsilon^2 - 4fA\varepsilon \cos(\delta_2 - \delta_0)}{f + 2fA^2\varepsilon^2 + (1-f)B\varepsilon} \quad (3.12)$$

Further simplification of Eq. (3.12) can be achieved by setting the cosine term equal to one.<sup>132, 134</sup> At the extreme limit of  $f=0$ , corresponding to photodetachment from a pure  $s$  type wave, Eq. (3.12) predicts a  $\beta$  value of +2, which is in agreement with Eq. (3.3). In the limit of  $f=1$ , corresponding to detachment from a pure  $p$  wave, Eq. (3.10) reduces to Eq. (3.2) This shows Eq. (3.12) is valid for atomic systems, but is also valid for mixed  $sp$  systems. As a result of this, the photoelectron angular distributions recorded in this chapter are analyzed with the mixed  $sp$  model in Eq. (3.12).

The photoelectron angular distributions measured in this experiment for both the  $^2\Pi$  and  $^4\Sigma^-$  states were fit to Eq. (3.12) from the mixed  $sp$  model. Figure 3.2 shows the anisotropy parameter,  $\beta$ , as a function of electron kinetic energy for both the  $^2\Pi \leftarrow ^3\Sigma^-$  (red diamonds) and  $^4\Sigma^- \leftarrow ^3\Sigma^-$  (blue dots) transition. The best fit for each curve to Eq. (3.12) is also shown in Figure 3.2. The fit for the  $^2\Pi \leftarrow ^3\Sigma^-$  transition goes through most of the points. Deviation between

experimental data and Eq. (3.12) occurs at higher electron kinetic energies. This could be attributed to the Wigner threshold approximation, which is only good at low electron kinetic energies. Additionally, some delocalization of electron density onto the hydrogen atom, which is not accounted for in the model, could be responsible. For the best reported fit the fractional  $p$  coefficient,  $f$ , is equal to 0.95. This is excellent agreement with the expected value of  $f \approx 1$ , considering the  $1\pi$  orbital is approximated as a nearly pure carbon  $2p$  orbital. These data points could also be fit using the Cooper-Zare model for detachment from a  $p$ -type orbital. A fit between  $^4\Sigma \leftarrow ^3\Sigma^-$  transition and Eq. (3.12) cannot be made. Particularly problematic is the low electron kinetic energy region. This behavior cannot be fit to Eq. (3.12). At higher electron kinetic energies a crude fit can be obtained. The corresponding fractional  $p$  character from this fit is  $f = 0.99$  for the  $3\sigma$  orbital. However, this value for  $f$  is not realistic.

Two possible explanations can be offered to account for the poor fit between the mixed  $sp$  model and the PADs for detachment from the  $3\sigma$  orbital. It is possible the assumptions used to derive Eq. (3.12) break down, or detachment from the  $3\sigma$  orbital of  $\text{CH}^-$  involves other effects not included in the mixed  $sp$  model. Identifying major problems with the derivation of Eq. (3.12) is difficult. In the extreme limits of  $f$ , Eq. (3.12) reduces to the pure atomic functions given in Eq. (3.3). This suggests the model captures the underlying physics in cases of weak and strong  $sp$  mixing. The agreement between the experimental data and Eq. (3.12) for detachment from the  $1\pi$  orbital, as well as previous studies on  $\text{NH}_2^-$  and  $\text{CCl}_2^-$ , suggests Eq. (3.12) adequately describes electron detachment from a mixed  $sp$  orbital in well-behaved systems.<sup>50</sup> Therefore, it is unlikely the model function is responsible for the major disagreement between our experiment and Eq. (3.12).

The other possibility is  $\text{CH}^-$  deviates from Eq. (3.12) due to physical processes not included in the model. At approximately 0.5 eV  $\beta$  is zero. This corresponds to an isotropic PAD. Isotropic PADs are typically signatures of a resonant or secondary process. Scrambling of the angular distributions is known to occur between photon absorption and electron ejection from a long-lived state.<sup>56-58</sup> In a study on the photodissociation of  $\text{O}_{2n}^-$  clusters spontaneous electron ejection (auto-detachment) occurs in highly vibrationally excited  $\text{O}_2^-$  photofragments.<sup>56,57,59</sup> The excited oxygen molecule produces an isotropic PAD because electrons are emitted in random directions. This arises from the timescale of photodetachment. Photodetachment is generally thought to occur instantaneously. In comparison to rotation and vibrations in the molecule, electron detachment is infinitesimally short. In the event an anion is excited into a long-lived state the anion has ample time to rotate before electron ejection occurs. This rotation of the anion produces the isotropic signature associated with resonant or secondary processes. Generation of anions in a temporary state, such as dipole bound anions, vibrationally, or electronically excited anions, acts as another source of long-lived anions.<sup>58</sup> The isotropic PAD measured in Figure 3.2 is most likely due to an unexpected long-lived resonant state present in  $\text{CH}^-$  anion. The effects of resonant states are not included in Eq. (3.12), thus it does not reproduce the experimental trend observed for detachment from the  $3\sigma$  orbital.

It is important to identify the source of resonance if an excited anion is generated. The small dipole moment of  $\text{CH}^-$  makes a dipole-bound anion unlikely. However, electron excitation could occur. The ground state electron configuration of  $\text{CH}^-$  is  $(1\sigma)^2(2\sigma)^2(3\sigma)^2(1\pi)^2$  where both  $\pi$  orbitals are half-filled. Two types of low energy transitions must be considered: electron excitation from the  $1\pi$  orbital to a higher unoccupied orbital or excitation from the  $3\sigma$  orbital to the partially filled  $1\pi$  orbital. No connection is observed between the resonance state and the  $^2\Pi$

state in CH. However, there is a connection observed between the resonance state and the  $^4\Sigma^-$  state. Figure 3.3 shows a schematic electronic energy diagram for the anion excitation and electron auto-detachment mechanism. The corresponding electron structure is also shown in the adjacent curves. According to Figure 3.3, the  $^4\Sigma^-$  state is produced from excitation of a  $3\sigma$  electron to the  $1\pi$  orbital followed by auto-detachment. Excitation of a  $1\pi$  electron does not produce the  $^4\Sigma^-$  state. This means the deviation between the experimental data and Eq. (3.12) is a result of the  $^3\Pi \leftarrow ^3\Sigma^-$  transition. This assignment explains why the angular distributions for the  $^2\Pi$  state are not affected by the resonance.

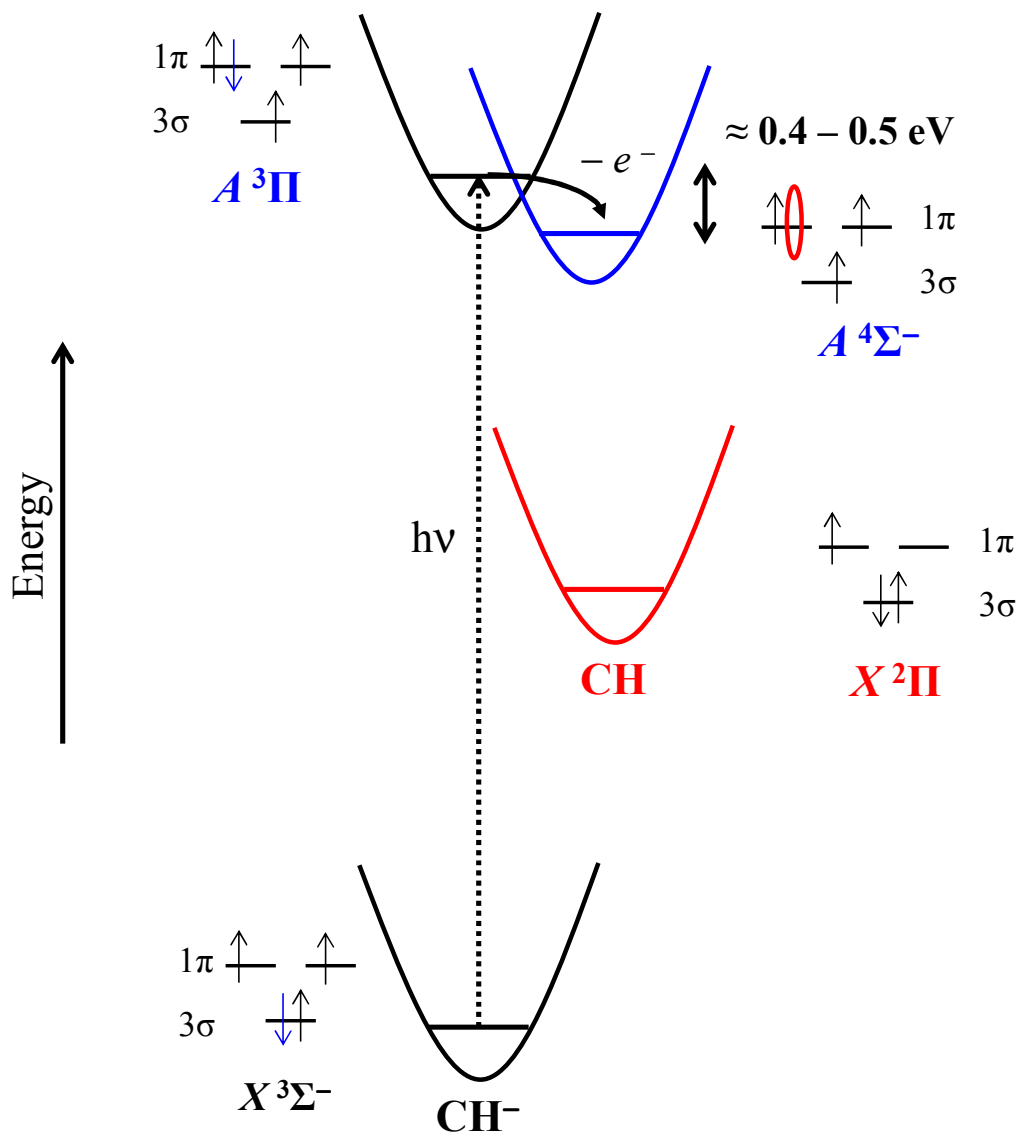


Figure 3.3: Schematic electronic energy diagram illustrating the mechanism for anion excitation and electron auto-detachment from the excited state of  $\text{CH}^-$ . The corresponding electronic structure diagrams for each state is indicated by the red arrow, and the only low-lying neutral state allowed by electron auto-detachment is the  $^4\Sigma^-$  excited state of  $\text{CH}$ , as indicated by the red circle.

### 3.4 Conclusions

Photoelectron imaging experiments were conducted on a newly constructed negative ion photoelectron imaging spectrometer on  $\text{CH}^-$  at wavelengths ranging from 410 nm to 600 nm. Analysis of the photoelectron spectra show two major peaks. The first peak, with electron binding energy of  $1.26 \pm 0.02$  eV, corresponds to the  $X^2\Pi \leftarrow X^3\Sigma^-$  (detachment from the  $1\pi$  orbital) transition. The second peak is assigned to the  $^4\Sigma^- \leftarrow X^3\Sigma^-$  (detachment from the  $3\sigma$  orbital) transition, and has an electron binding energy of  $1.98 \pm 0.02$  eV. The photoelectron angular distributions were analyzed using a qualitative symmetry based approach and a quantitative method using the mixed  $sp$  model. The symmetry based approach accurately predicted the magnitude of the anisotropy parameter for detachment from the  $1\pi$  orbital, but not for detachment from the  $3\sigma$  orbital. This provided motivation for testing the recently developed mixed  $sp$  model. The equation for the mixed  $sp$  model, Eq. (3.12), correctly modeled behavior for detachment from the  $1\pi$  orbital. However, detachment from the  $3\sigma$  orbital did not agree with model behavior predicted by Eq. (3.12). This discrepancy is the result of an excited temporary anion state with a lifetime sufficiently long for rotation before electron emission. This produces an isotropic PAD, as observed at low electron kinetic energies. Analysis of the photoelectron angular distribution using the mixed  $sp$  model revealed evidence for a temporary anion excited state of  $\text{CH}^-$  previously not observed or predicted.

## CHAPTER 4

### PHOTOELECTRON IMAGING OF NITROMETHANE CLUSTER ANIONS

#### 4.1 Introduction

Nitromethane,  $\text{CH}_3\text{NO}_2$ , is the simplest nitro-substituted organic compound. It is a prototypical compound capable of forming molecular anions due to the high electron affinity of the nitro group. Efforts to understand the formation of  $\text{CH}_3\text{NO}_2^-$  have been made utilizing electron transfer collisions with free electrons,<sup>60</sup> Rydberg atoms,<sup>61,62</sup> and alkali metal atoms.<sup>63-66</sup> The results from these works have shown valence bound  $\text{CH}_3\text{NO}_2^-$  forms through an initial dipole bound state. The excess electron is in a diffuse orbital on the methyl group in the dipole bound state. However, out-of-plane bending of the nitro group results in the energy of the  $\pi^*$  orbital of the nitro group being lowered. This results in the excess electron shifting into the  $\pi^*$  orbital, giving the anion a non-planar C- $\text{NO}_2$  group.

Several experimental studies have been conducted on the nitromethane anion.<sup>51,61,67-70</sup> Conventional photoelectron spectroscopy has been used to probe the dipole and valence bound states of nitromethane.<sup>61</sup> An adiabatic electron affinity of  $0.26 \pm 0.08$  eV was first reported for the nitromethane anion in this study. Infrared spectroscopy studies have demonstrated auto-detachment from  $\text{CH}_3\text{NO}_2^-$  occurs as a result of vibrational excitation of CH stretches.<sup>71,72</sup> More recent low energy photoelectron imaging experiments have reported an adiabatic electron affinity of  $0.172 \pm 0.006$  eV for the nitromethane anion.<sup>67</sup> This is the currently accepted value for the adiabatic electron affinity for nitromethane. Additional photoelectron imaging experiments

using high energy photons have been conducted to probe the excited electronic states of nitromethane and assign symmetries to the observed electronic states.<sup>68</sup>

Hydrated nitromethane anion,  $\text{CH}_3\text{NO}_2^-\cdot(\text{H}_2\text{O})$ , has also been widely studied.<sup>69,73,74</sup> Infrared photodissociation spectroscopy with Ar tagging was used to structurally characterize the nitromethane anion water complex.<sup>73,74</sup> These works showed a double ionic hydrogen bond is formed between the H-atoms on the water and the O-atoms on the nitromethane anion. The interaction between the nitromethane and water molecule in the neutral species is limited to a single hydrogen bond. Identical results were obtained from a vibrational spectroscopy experiment aimed at investigating the influence of hydration on the solute anion.<sup>69</sup> Good agreement was found between the vibrational spectroscopy work and theoretical studies at the MP2/aug-cc-pVDZ level.<sup>73</sup>

Photodissociation spectroscopy has been used to investigate the dissociation of nitromethane cluster anions,  $\text{CH}_3\text{NO}_2^-_n$ ,  $n = 1 - 6$ .<sup>68</sup> The  $\text{NO}_2^-(\text{CH}_3\text{NO}_2)_k$  and  $\text{OH}^-$  products form from core-dissociation, whereas the  $(\text{CH}_3\text{NO}_2)_k^-$  fragment forms as a result of energy transfer from the excited anion to the solvent network or a core-dissociation-recombination mechanism. These fragments are consistent with the anion clusters containing a monomer-anion core solvated by neutral nitromethane molecules.

The aim of this study was to examine the photoelectron spectra of small nitromethane cluster anions. Shifts in the vertical detachment energies (VDEs) were used to estimate solvation energies. Estimated values for the electron affinities of each cluster were also estimated from the photoelectron spectra. Structures for each cluster are proposed based on low-level theoretical calculations. Theoretical VDEs and ADEs are presented for each cluster structure. Probable

structures for the nitromethane dimer and trimer are proposed from calculated detachment energies.

## 4.2 Methods

The experiments described in this chapter were completed using the negative ion time-of-flight velocity map imaging<sup>24</sup> spectrometer described in Chapter 2. Argon carrier gas was seeded with nitromethane vapor and introduced into the vacuum chamber through the pulse valve operating at 10 Hz and 40 psi backing pressure. The electron gun was positioned opposite the direction of the gas expansion. Anions were formed by secondary-electron attachment following collisions with high-energy electrons (1 keV). The anions were mass-analyzed using the linear TOF-MS.

The fundamental wavelength of a pulsed Nd:YAG laser was frequency tripled to produce 355 nm photons. At this wavelength, the average power of the laser is 54 mJ/pulse. Approximately 2 m downstream from the source region, the anions of interest interact with the beam of photons in the velocity-map imaging assembly. Photoelectrons are created from the overlap of the laser with the specific anion packet. These photoelectrons are accelerated and focused onto the imaging MCP detector. Approximately 30,000 laser shots were utilized to collect the photoelectron images shown in this chapter. Each image was analyzed by the procedures described in Chapter 2. The photoelectron spectra were calibrated using the well-known transitions of  $O^{\bullet-}$  at 355 nm.<sup>47,48</sup>

Theoretical calculations were carried out using the Gaussian 09 suite of programs.<sup>75,76</sup> Cluster geometries were optimized at the unrestricted density functional theory level with the B3LYP functional<sup>77,78</sup> and 6-31+G(d),<sup>79</sup> 6-31++G(d,2p),<sup>80</sup> 6-311+G(d),<sup>75</sup> and aug-cc-pVDZ<sup>81</sup>

basis sets. Normal mode analysis for each optimized structure showed no imaginary frequencies. This confirms each structure corresponds to a local minimum. These calculations serve as a point of comparison for the experimental vertical detachment energies and estimated electron affinity values. The energetics reported are meant to serve as points of relative comparisons.

## 4.3 Results and Discussion

### *4.3.1 Photoelectron Images and Spectra*

Figure 4.1 shows the projected and reconstructed photoelectron images for the nitromethane (a) monomer, (b) dimer, (c) trimer, and (d) hydrated monomer. The two distinct features of each image are labeled A and B. Figure 4.2 shows the corresponding photoelectron spectra extracted from each image. Band A corresponds to electron detachment from the anion to form the neutral species in the electronic ground state. Band B corresponds to the lowest energy triplet state of nitromethane. The spectrum for the monomer is in good agreement with a previously published spectrum at 355 nm.<sup>68</sup>

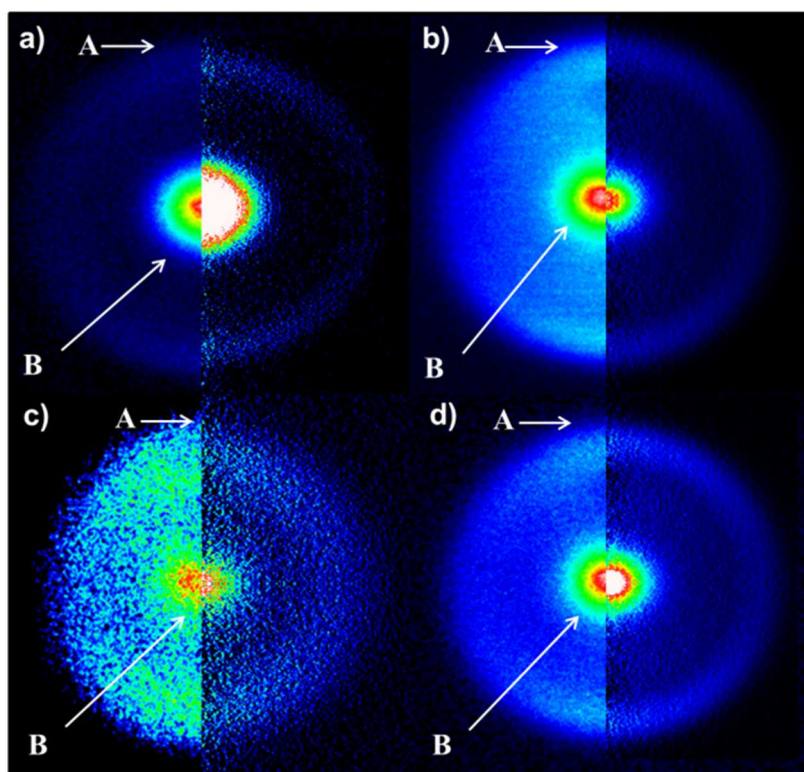


Figure 4.1: Raw (left) and reconstructed (right) photoelectron images of nitromethane anion (a) monomer, (b) dimer, (c) trimer, and (d) hydrated monomer recorded at 355 nm. The laser polarization axis is vertical in the plane of the figure.

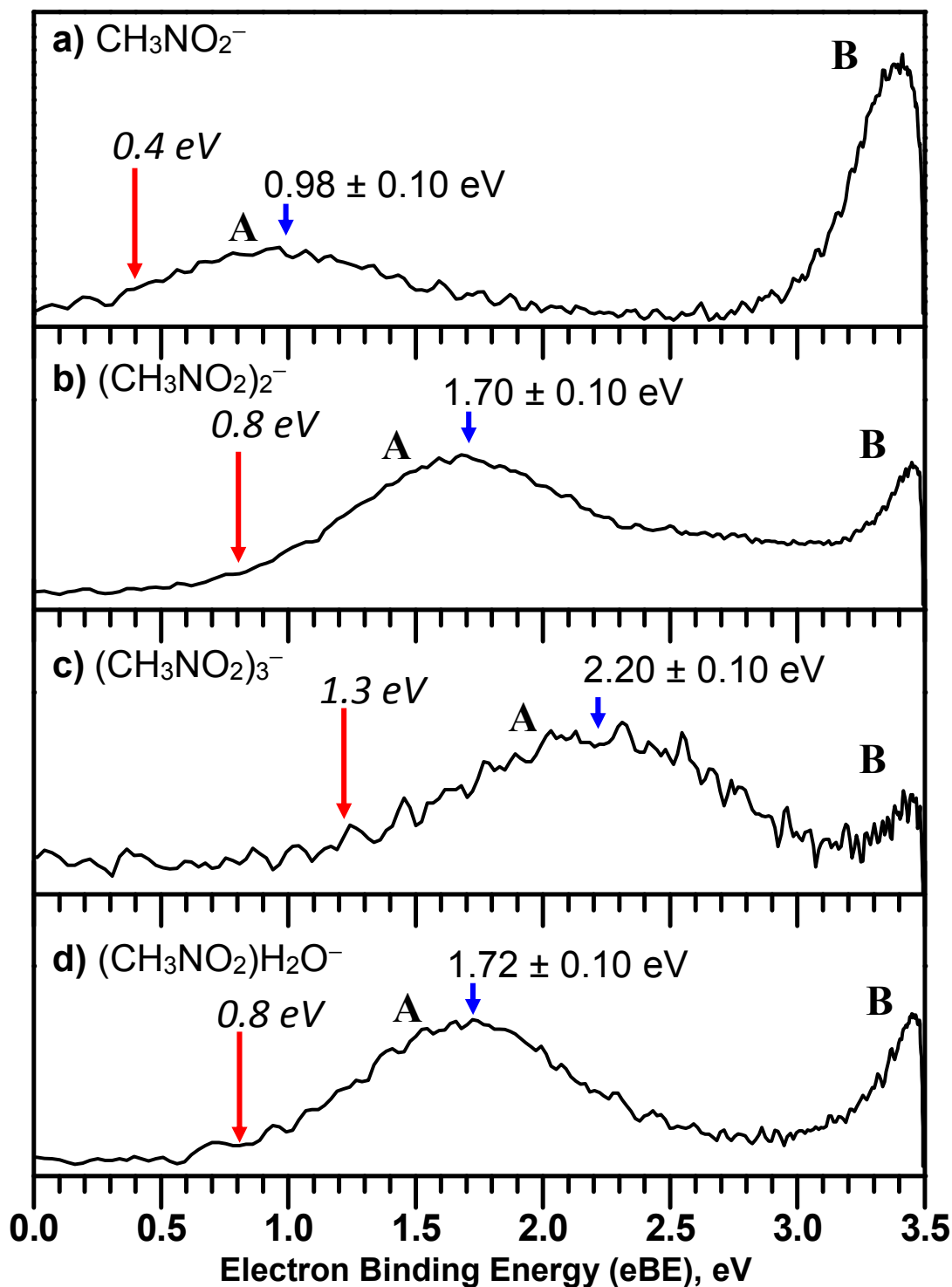


Figure 4.2: Photoelectron spectra of nitromethane anion (a) monomer, (b) dimer, (c) trimer, and (d) hydrated monomer. The energy scale is the electron binding energy (eBE) obtained by subtracting the electron kinetic energy from the photon energy. The vertical detachment energies are listed above the blue arrows. The estimated electron affinities,  $EA_{\text{est}}$ , are listed above the red arrows in italics.

The unresolved band A in Figure 4.2(a) is a result of a large change in geometry upon photodetachment of the excess electron in the  $\pi^*$  orbital of  $\text{CH}_3\text{NO}_2^-$ . As a result of electron detachment from the anion the geometry of the nitrogen atom is changed. In the nitromethane anion the nitrogen atom has a trigonal pyramidal geometry with a C- $\text{NO}_2$  dihedral angle of  $147^\circ$ , whereas the C- $\text{NO}_2$  dihedral angle in neutral nitromethane is nearly planar. Upon electron detachment, the neutral molecule is formed in a highly vibrationally excited state because the C- $\text{NO}_2$  out of plane vibration is a low energy vibration. This results in a large difference in geometry between the anion and neutral. As a result of this, band A is a broad featureless band for the electronic ground state of neutral nitromethane. Figure 4.2 shows band B shifts to higher detachment energies as the cluster size increases. This shift is responsible for the decrease in relative intensity for band B because the band is shifted to energies greater than the photon energy used in this work. The onset of this band is shown in Figure 4.2 (b) – (d). The unresolved nature of band B is a result of the low resolution of our velocity-map imaging assembly. The primary focus of this band is the shift in the low energy band, A, as a function of solvation. Comparison of the nitromethane anion cluster spectra shows a shift in band A to higher energy. This is attributed to solvent stabilization. The similarity of the spectra suggests the anion clusters consists of a monomer-anion solvated by neutral molecules.<sup>82</sup>

Exact electron affinities for nitromethane and nitromethane cluster anions cannot be determined from Figure 4.2. This is because the origin transition cannot be identified. As a result of this, approximate electron affinity values are determined by estimating the onset of band A for each cluster in Figure 4.2. These onsets are indicated by the red arrows. In order to avoid confusion with adiabatic electron affinities determined from the energy of an unambiguously identified origin band, the approximated electron affinities are reported as estimated electron

affinities,  $EA_{\text{est}}$ . The reported  $EA_{\text{est}}$  of the nitromethane anion from Figure 4.2(a) is approximately 0.4 eV. This is considerably larger than the currently accepted adiabatic detachment energy of 0.172 eV. The difference corresponds to an uncertainty of approximately  $\pm 0.2$  eV for our  $EA_{\text{est}}$  values. The VDE for the nitromethane anion is  $0.98 \pm 0.10$  eV. This value is in good agreement with previously published VDEs.<sup>51,61,67,74</sup> The dimer and trimer anion clusters have VDEs of  $1.70 \pm 0.10$  eV and  $2.20 \pm 0.10$  eV respectively. The hydrated nitromethane anion has a VDE of  $1.72 \pm 0.10$  eV, which is in agreement with a previously reported VDE of  $1.57 \pm 0.1$  eV.<sup>74</sup>

#### 4.3.2 Structure Calculations

Optimized structures and the singly occupied molecular orbital (SOMO) for the nitromethane neutral and anion clusters calculated at the B3LYP/aug-cc-pVDZ level of theory are shown in Figure 4.3. Important distances are reported in Angstroms. The C-NO<sub>2</sub> dihedral, an important parameter for characterizing the differences between nitromethane molecules, are reported for each cluster molecule. The nitromethane anion has a calculated C-NO<sub>2</sub> dihedral angle of 146.4°. The SOMO of the anion shows the excess electron is localized in the  $\pi^*$  orbital of the NO<sub>2</sub> group. Figure 4.3 shows the neutral nitromethane molecule has a nearly planar C-NO<sub>2</sub> group, with slightly shorter N – O bond distances.

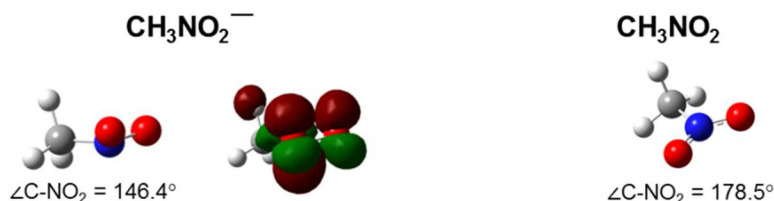


Figure 4.3: Optimized structures and SOMO for the nitromethane anion and neutral at the (U)B3LYP/aug-cc-pVDZ level of theory. Distances are given in Å. C-NO<sub>2</sub> dihedral angles are also reported.

Figure 4.4 contains the optimized structures for the hydrated nitromethane anion and neutral cluster. The anion structure shows the two hydrogen atoms on the water molecule are bound to the oxygen atoms on the nitro group. At the B3LYP/aug-cc-pVDZ level of theory the hydrogen bond distances are both 1.98 Å. The C-NO<sub>2</sub> dihedral angle is calculated to be 145.0°. This is nearly identical to the dihedral angle calculated for the monomer anion. Examination of the SOMO shows the excess electron remains localized in the  $\pi^*$  orbital of the nitro group. A similar structure for the hydrated nitromethane anion was predicted in previous studies utilizing density functional theory and MP2 methods.<sup>69,71,73,83</sup> The optimized hydrated neutral cluster structure differs in two aspects. In the neutral species, the water molecule interacts with the nitromethane molecule through one strong hydrogen bond to a single oxygen atom. The C-NO<sub>2</sub> dihedral angle is nearly planar in the neutral structure.

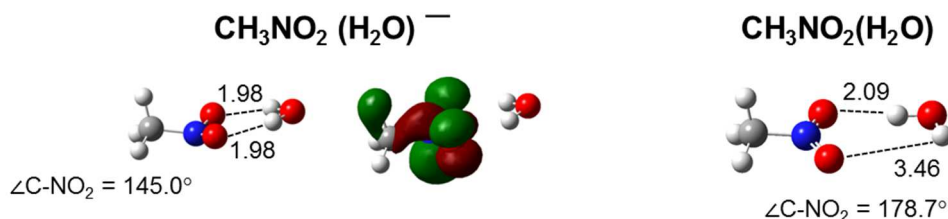


Figure 4.4: Optimized structures and SOMO for the hydrated nitromethane anion and neutral at the (U)B3LYP/aug-cc-pVDZ level of theory. Distances are given in Å. C-NO<sub>2</sub> dihedral angles are also reported.

The lowest energy structure for the nitromethane dimer anion is shown in Figure 4.5. The anion dimer has a bent structure, not the linear ion-dipole complex one might expect. Ion-dipole forces hold the dimer cluster together through a single O...C-H interaction. These intermolecular interactions are discussed in terms of hydrogen bond donors (D) or acceptors (A) as labeled in Figure 4.5. The oxygen-hydrogen bond distance is 1.92 Å, similar to the hydrogen bond distance calculated for the hydrated nitromethane anion. The acceptor molecule has a C-NO<sub>2</sub> dihedral

angle of  $149.1^\circ$ , whereas the donor molecule has a C-NO<sub>2</sub> dihedral angle of  $176.9^\circ$ . The dihedral angle on the acceptor molecule is similar to the C-NO<sub>2</sub> dihedral angle of the nitromethane anion. This indicates the excess electron is located on one molecule in the dimer structure. The SOMO shows the excess electron is localized on a  $\pi^*$  orbital of the acceptor molecule. This indicates the dimer structure is composed of a monomer-anion solvated by a neutral nitromethane molecule.

The removal of the excess electron results in a large geometry change according to the optimized neutral dimer structure. The two nitromethane molecules interact through two O $\cdots$ C-H interactions. In this structure, each molecule is acting as both a hydrogen bond donor and acceptor. The additional O $\cdots$ C-H interaction, resulting from the side-by-side arrangement of the nitromethane molecules, stabilizes the neutral dimer cluster. The ionic dimer cluster is bound through a strong ion-dipole interaction; however, the weaker dipole-dipole interaction of the neutral dimer cluster prefers a side-by-side binding. This change in structure suggests the origin transition for the anion dimer cannot be observed directly as a result of poor Franck-Condon overlap.

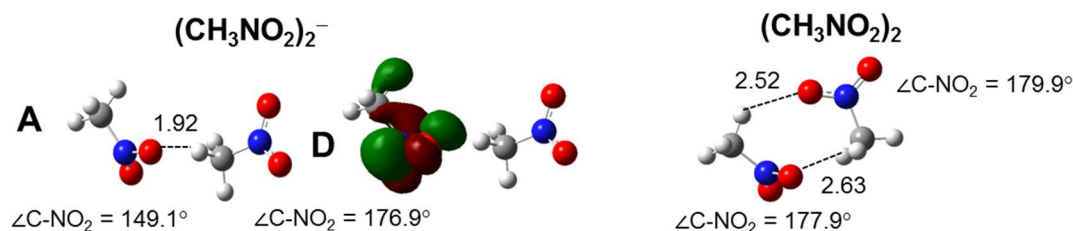


Figure 4.5: Optimized structures and SOMO for the nitromethane dimer cluster anion and neutral at the (U)B3LYP/aug-cc-pVDZ level of theory. Distances are given in Å. C-NO<sub>2</sub> dihedral angle are also reported.

The optimized trimer anion structure is shown in Figure 4.6. The molecules in the cluster are identified by their hydrogen bond interactions as a donor-acceptor (DA), donor-double-acceptor (DAA), and donor (D). The donor-double-acceptor molecule has a C-NO<sub>2</sub> dihedral

angle of  $154.2^\circ$ . This indicates the excess electron is located on this molecule. The C-NO<sub>2</sub> dihedral angle of the single donor molecule is  $178.3^\circ$ , whereas the donor-acceptor molecule has a dihedral angle of  $175.6^\circ$ . The distance between the methyl hydrogen on the donor-double-acceptor molecule to the oxygen atom of the nitro group of the donor-acceptor molecule is 2.70 Å. The distance between the oxygen atom of the donor-double-acceptor molecule and the methyl hydrogen on the donor-acceptor molecule is 1.88 Å. The oxygen atom on the donor-double-acceptor molecule is separated from the methyl hydrogen of the donor molecule by 2.02 Å. The SOMO shows the excess electron is primarily localized on the donor-double-acceptor molecule. A small amount of charge is delocalized onto the donor-acceptor molecule. This indicates the trimer anion is composed of a monomer-anion solvated by two neutral molecules with the second neutral nitromethane molecule binding at two positions rather than a single site. The donor molecule binds to the lowest energy binding site through a direct O··C-H interaction, therefore the donor-acceptor molecule must bind to the anion through indirect O··C-H side-by-side interactions.

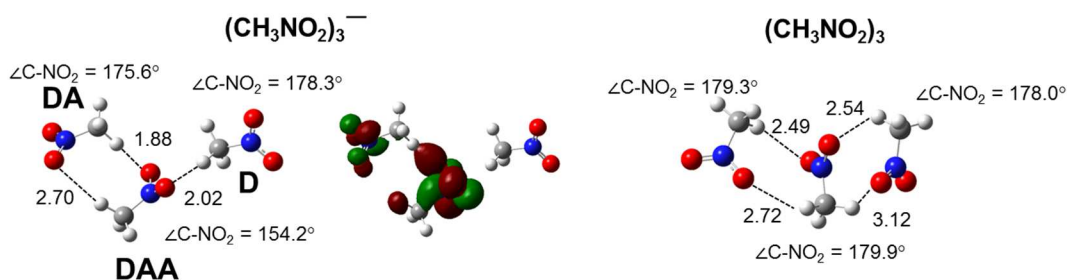


Figure 4.6: Optimized structures and SOMO for the nitromethane trimer cluster anion and neutral at the (U)B3LYP/aug-cc-pVDZ level of theory. Distances are given in Å. C-NO<sub>2</sub> dihedral angle are also reported.

Figure 4.6 also shows the lowest energy structure for the optimized neutral trimer. This structure is similar to the neutral dimer structure in regards to the side-by-side binding scheme. The center molecule acts as a hydrogen bond double-donor-double-acceptor, whereas each

exterior molecule acts as a donor-acceptor. The optimized neutral trimer structure shows there is a significant change in geometry of the single donor molecule of the trimer anion structure upon electron detachment to allow for the side-by-side binding seen in the optimized neutral trimer structure.

#### *4.3.3 Vertical Detachment and Adiabatic Detachment Energies*

DFT level theory was used to calculate VDEs and ADEs for each cluster structure. The VDEs were calculated by taking the differences in electronic energies from the neutral and anion at the optimized anion geometry. ADEs were calculated from the differences in the electronic energies with zero-point vibrational energy corrections for the optimized neutral and optimized anion form of each cluster. The calculated VDEs and ADEs using the B3LYP functional with a variety of basis sets are included in Table 4.1. The calculated VDEs of the nitromethane anion are  $\sim 0.3$  eV higher than the experimental value. The dimer and trimer cluster anions have calculated VDEs approximately 0.2 eV higher than the experimental value for all basis sets. The calculated VDEs for the hydrated nitromethane anion is 0.3 – 0.4 eV higher than the experimental value. There is relatively good agreement between the experimental and calculated VDEs. It is also important to note the calculated VDEs are consistent for all basis sets.

The ADE for the nitromethane anion is  $\sim 0.5$  eV for all basis sets used in this study. This is in good agreement with the 0.4 eV value for the approximate electron affinity of the nitromethane anion in this work. The dimer anion ADEs are approximately 1.2 eV. These values are larger than the estimated electron affinity of  $\sim 0.8$  eV. In the case of the trimer anion, the calculated ADEs are 1.60 – 1.64 eV, whereas the estimated electron affinity is  $\sim 1.3$  eV. The calculated ADEs for the hydrated nitromethane anion are 1.04 – 1.15 eV. The estimated electron

affinity is 0.8 eV. Comparison shows the calculated ADEs are greater than the estimated electron affinities. However, if we consider the large uncertainty,  $\pm 0.2$  eV, of the estimated electron affinities and the low level of theory used in this study, an acceptable agreement is found between experiment and theory.

#### 4.3.4 Cluster Structure – Experiment and Theory

Definitive structural assignments are not possible from the broad, featureless spectra in Figure 4.2. The unresolved nature in band A in Figure 4.2(a) is due to the large geometry change between the anion and neutral structure upon electron ejection. Similar band shapes are found in the photoelectron spectra of the clusters. This suggests large geometry changes to the nitro group, along with solvent reorganization, occurs in the cluster structures as a result of electron detachment. This is supported by the neutral structures in Figure 4.3-4.6. Characterization of the bands is possible by calculating the difference in the detachment energies. This is done according to Eq. (4.1)

$$\Delta DE = VDE - ADE \quad (4.1)$$

where  $\Delta DE$  is the difference in the detachment energies, VDE is the vertical detachment energy, and ADE is the adiabatic detachment energy. The difference in the detachment energies can be related to the Franck-Condon overlap as well as to the geometry difference between the anion and neutral structures. The overestimation of the VDEs and ADEs by theory is somewhat corrected by taking the difference in the calculated detachment energies. This allows for better agreement between experiment and theory. The theoretical  $\Delta DE$ s for the nitromethane, dimer, trimer, and hydrated nitromethane anion are listed in Table 4.1. The experimental  $\Delta DE$  values

are also included in Table 4.1 These values were calculated using the experimental vertical detachment energies and estimated electron affinities.

The theoretical  $\Delta$ DE for the nitromethane anion is approximately 0.7 – 0.8 eV, whereas the experimental  $\Delta$ DE is  $\sim$ 0.6 eV. The hydrated nitromethane anion has a theoretical  $\Delta$ DE just under 1 eV. This is in good agreement with the experimental value of approximately 0.9 eV. This difference is expected given the differences in the structures calculated for the anion and neutral dimer clusters. The trimer species has a theoretical  $\Delta$ DE of about 0.8 eV. This is also in good agreement with the experimental difference of 0.9 eV. These comparisons suggest the anion clusters are made from a single anion solvated by neutral molecules. Based on the limited spectral information the structures obtained from the theoretical calculations in this work are reasonable assignments. However, other experimental methods such as vibrational spectroscopy are better suited to confirm the structure of the dimer and trimer cluster anions.

Table 4.1: Comparison between experimental and theoretical vertical detachment energies (VDEs), adiabatic detachment energies (ADEs), and differences in detachment energies ( $\Delta$ DEs) for each cluster structure.

	Experiment	6-31+G(d)	6-31+G(d,2p)	6-31++G(d,2p)	6-311+G(d)	aug-cc-pVDZ
$\text{CH}_3\text{NO}_2^-$						
VDE (eV)	0.98	1.28	1.25	1.29	1.27	1.18
ADE (eV)	0.4 <sup>a</sup>	0.49	0.50	0.52	0.48	0.49
$\Delta$ DE(eV)	0.6	0.79	0.75	0.77	0.79	0.69
$(\text{CH}_3\text{NO}_2)_2^-$						
VDE	1.70	1.87	1.97	1.96	1.86	1.92
ADE	0.8 <sup>a</sup>	1.17	1.17	1.18	1.15	1.14
$\Delta$ DE(eV)	0.9	0.70	0.80	0.78	0.71	0.78
$(\text{CH}_3\text{NO}_2)_3^-$						
VDE	2.20	2.36	2.41	2.42	2.31	2.39
ADE	1.3 <sup>a</sup>	1.62	1.64	1.64	1.61	1.60
$\Delta$ DE(eV)	0.9	0.74	0.77	0.78	0.70	0.79
$\text{NM}^-(\text{H}_2\text{O})$						
VDE	1.72	2.12	2.11	2.10	2.12	2.02
ADE	0.8 <sup>a</sup>	1.16	1.15	1.14	1.15	1.09
$\Delta$ DE(eV)	0.9	0.96	0.96	0.96	0.97	0.93

<sup>a</sup>Estimated electron affinities,  $\text{EA}_{\text{est}}$

#### 4.3.4 Ion Solvation Energies

Figure 4.7 is a schematic potential energy surface showing the detachment energy differences as a function of ion solvation. The difference in the detachment energies is equal to the difference in the solvation energy of the anion and neutral clusters. Neutral solvation energies are typically much smaller than ion solvation energies. As a result of this, we make the assumption the neutral solvation energies can be neglected. Thus, the differences in detachment energies reported here are estimates of the anion solvation energies. Table 4.2 contains the solvation energies calculated for each cluster. These values were calculated from the VDEs reported in Table 4.1. The anion solvation energies reported should be treated as upper limits due to the neglect of neutral solvation energies.

The dimer and trimer cluster anions have calculated solvation energies of 0.72 eV and 0.50 eV respectively. Theoretical calculations predict binding energies of 0.80 eV and 0.58 eV for the dimer and trimer species. These values are in reasonable agreement with our reported energies. The reported experimental binding energies are within 0.06 eV of values previously reported for the dimer and trimer anions.<sup>84</sup> Considering the neglect of neutral-neutral solvation energies, these values are in good agreement. However, the experimental binding energies are lower than theoretical predictions for both the dimer and trimer clusters. This can be attributed to theoretical sources of error. The theoretical sources of error are expected to impact the neutral cluster energies more as a result of the weak interactions, which are difficult to treat accurately.

The cluster structures from Figure 4.3 are indirectly supported by the experimental solvation energies. The cluster with the highest binding energy is the hydrated nitromethane cluster with a binding energy of  $\leq 0.74$  eV. The water molecule in this cluster strongly binds through two hydrogen bonds. A slightly lower binding energy, 0.69 eV, is predicted from

theoretical calculations. The difference between theory and experiment can be attributed to the neglect of the hydrogen bond in the neutral hydrated nitromethane cluster. The binding energy of the solvent molecule in the dimer cluster is nearly as large. This is attributed to the strong interaction between the anion and the methyl group of the solvent molecule. Experiment and theory predict the binding energy will be lower for the second solvent molecule.

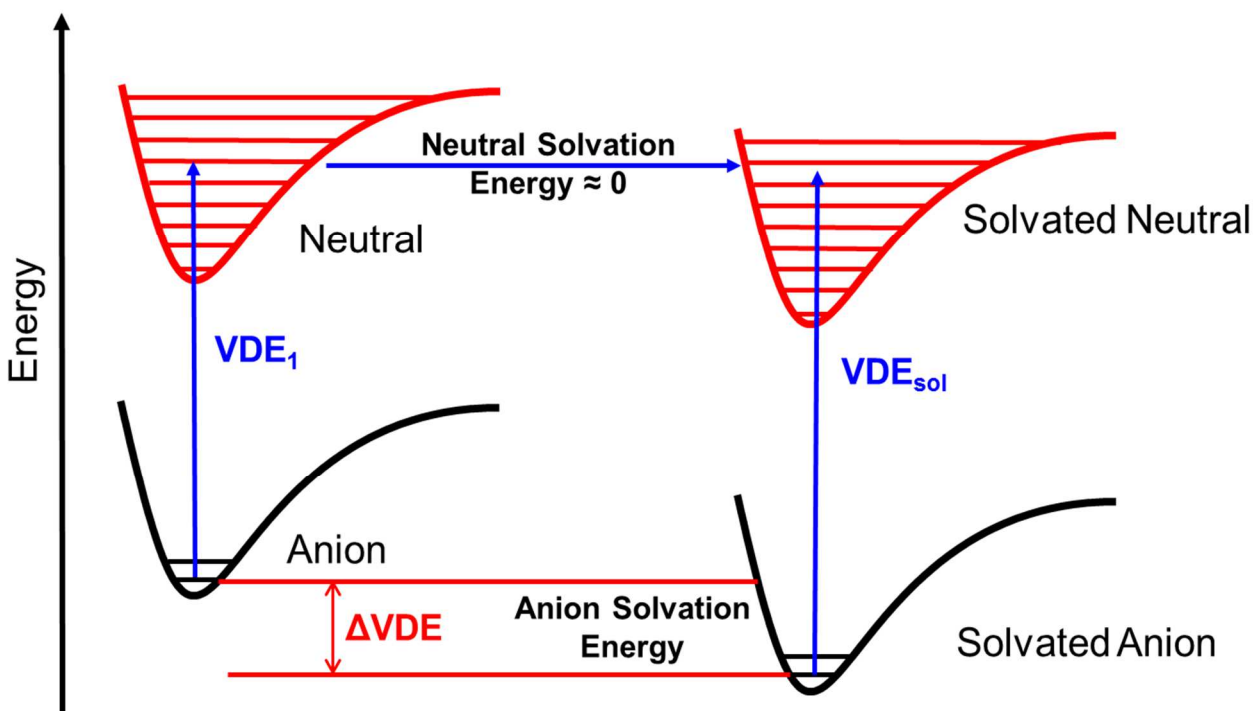


Figure 4.7: Schematic potential energy diagram illustrating the approach used to approximate solvation energies in this work.

Table 4.2: Solvation energies for the nitromethane clusters.

Reaction	Energy (eV)	Reference
$(NM)_2^- \rightarrow NM + NM^-$	$\leq 0.72$	This work
	0.80	This work (theory) <sup>a</sup>
	$0.659 \pm 0.009$	<sup>84</sup>
$(NM)_3^- \rightarrow NM + (NM)_2^-$	$\leq 0.50$	This work
	0.58	This work (theory) <sup>a</sup>
	$0.556 \pm 0.013$	<sup>84</sup>
$(NM \cdots H_2O)^- \rightarrow H_2O + NM^-$	$\leq 0.74$	This Work
	0.69	This work (theory) <sup>a</sup>

<sup>a</sup>Theoretical energies calculated from electronic + zero point energy differences at the (U)B3LYP/aug-cc-pVDZ level of theory

#### 4.4 Conclusions

Photoelectron spectroscopy was used in the study of nitromethane cluster anions. Ion energetics such as vertical detachment energies and estimated electron affinities were obtained from the photoelectron spectra. Stabilization of the solvent molecules results in an increase in the vertical detachment energies as the cluster size increases. Differences in the vertical detachment energies were utilized to estimate the anion solvation energies. Good agreement was found between experimental and theoretical vertical detachment energies and estimated electron affinities. Low energy structures for the dimer and trimer anion clusters, as well as their corresponding neutrals, were identified using theoretical calculations. The anion cluster structures suggest a single nitromethane anion is solvated by neutral nitromethane molecules *via* two O $\cdots$ C-H interactions, whereas the optimized neutral clusters show a preference for multiple interactions.

## CHAPTER 5

### C-N DISSOCIATION ENERGIES OF NITROBENZENE AND NITROTOLUENE RADICAL ANIONS AND NEUTRALS

#### 5.1 Introduction

Nitroaromatic compounds, such as 1,3,5-trinitrobenzene (TNB) and 2,4,6-trinitrotoluene (TNT), are high energy compounds often used in explosive applications. Typically, an external energy source is used to supply an initial energy packet to these compounds through shock (physical impact), chemical, or electrical energy. This external source provides the energy needed to start the initial endothermic bond-breaking step.<sup>2,4</sup> Homolytic bond cleavage of the weakest bond in the molecule is thought to occur in this first step. Few direct experimental measurements have been made concerning the bond energies of nitroaromatic compounds.<sup>85-87</sup>

Theoretical and experimental studies suggest three major initiation steps take place in the thermal decomposition of nitroaromatic compounds.<sup>10,11</sup> Figure 5.1 illustrates these reactions for *o*-nitrotoluene. These processes include (1) C-NO<sub>2</sub> homolysis, (2) isomerization of the NO<sub>2</sub> to an ONO, nitrite group, resulting in the elimination of NO•, and (3) attack of the methyl substituent to form the *aci* structure (-NO<sub>2</sub>H), ultimately resulting in the loss of H<sub>2</sub>O. All three reactions are expected to be important, but many models assume homolytic dissociation of the C-N bond is the initial reaction.<sup>12,88,89</sup> Consequently, it is important to know the amount of energy required to break the C-N bond in order to understand and model the decomposition of nitroaromatic compounds.

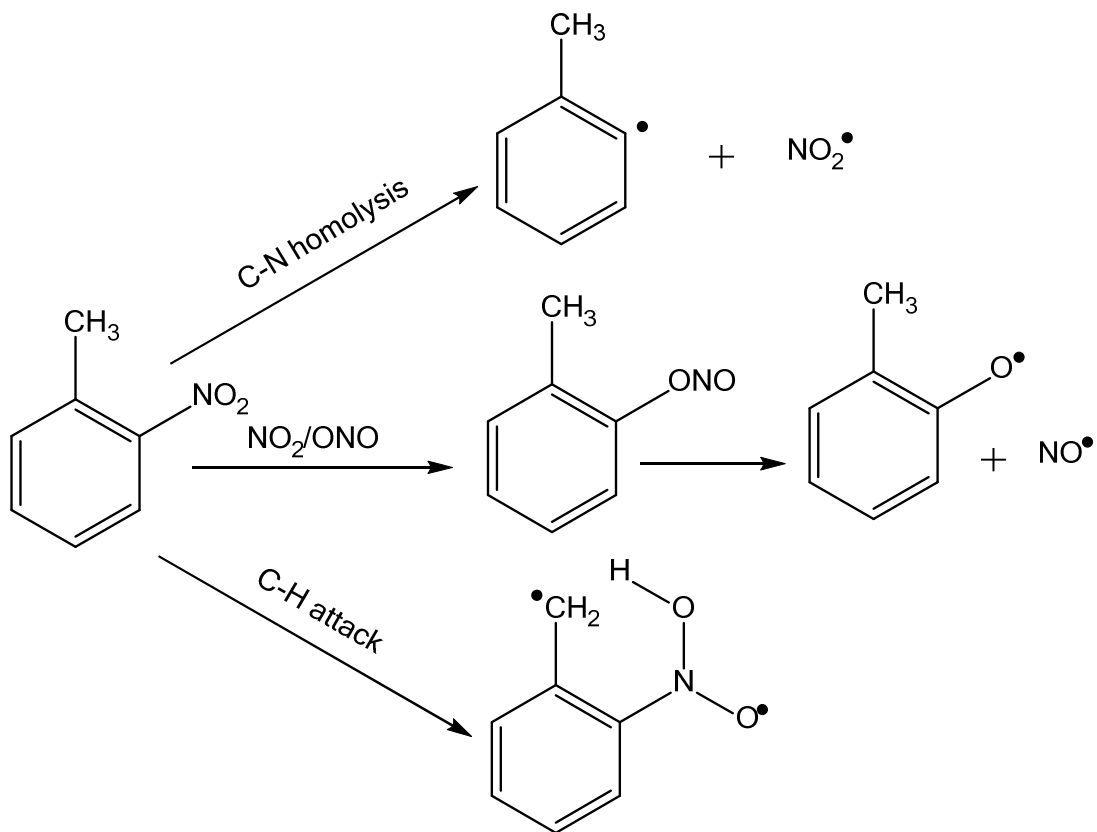


Figure 5.1: Dissociation reactions for *o*-nitrotoluene: (1) C-N homolysis, (2)  $\text{NO}_2/\text{ONO}$  rearrangement, and (3) C-H attack

Measuring direct bond dissociation energies is difficult; however, thermochemical cycles can be used to calculate bond energies. The anion thermochemical cycle can be derived from the potential energy diagram for C-N bond homolysis in Figure 5.2. The electron affinities (EAs), of nitrobenzene and NO<sub>2</sub> are defined as the amount of energy required to detach an electron from the ground vibrational state of the singly charged anion to form the neutral in the ground vibrational state. The dissociation energies, D<sub>0</sub>, are defined as the amount of energy required to break the C-N bond from the zero point vibrational energy of the molecule. The electron affinities of nitrobenzene and NO<sub>2</sub> and the dissociation energy of nitrobenzene radical anion, D<sub>0</sub>(NB<sup>•-</sup>) are needed to complete the thermochemical cycle. These values have been previously measured.<sup>90-92</sup> The dissociation energy of neutral nitrobenzene can be determined using Eq. (5.1).

$$D_0(NB) = -EA(NB) + D_0(NB^{\bullet-}) + EA(NO_2) \quad (5.1)$$

The C-N bond dissociation energy (BDE) of nitrobenzene was estimated to be 0.18 eV.<sup>64</sup> This is much lower than the bond energies for typical nitroaromatic compounds found in Table 5.1. Reduction of the C-N bond energies is expected to occur upon addition of an electron to a  $\pi^*$  orbital, but a difference of 2.8 eV seems extreme. Examination of the reported value revealed the authors used an electron affinity of 3.91 eV, from electron transfer measurements, for the NO<sub>2</sub> species.<sup>93</sup> A more accurate value, 2.273 + 0.005 eV, from negative ion photoelectron spectroscopy has since been reported for the electron affinity of NO<sub>2</sub>.<sup>92</sup> The current recommended value for the electron affinity of NO<sub>2</sub> suggests the C-N bond dissociation energy is approximately 1.8 eV. This value is in agreement with a recent infrared multiphoton dissociation experiment which also suggested a value of 1.8 eV for the BDE of the C-N bond of nitrobenzene anion.<sup>94</sup>

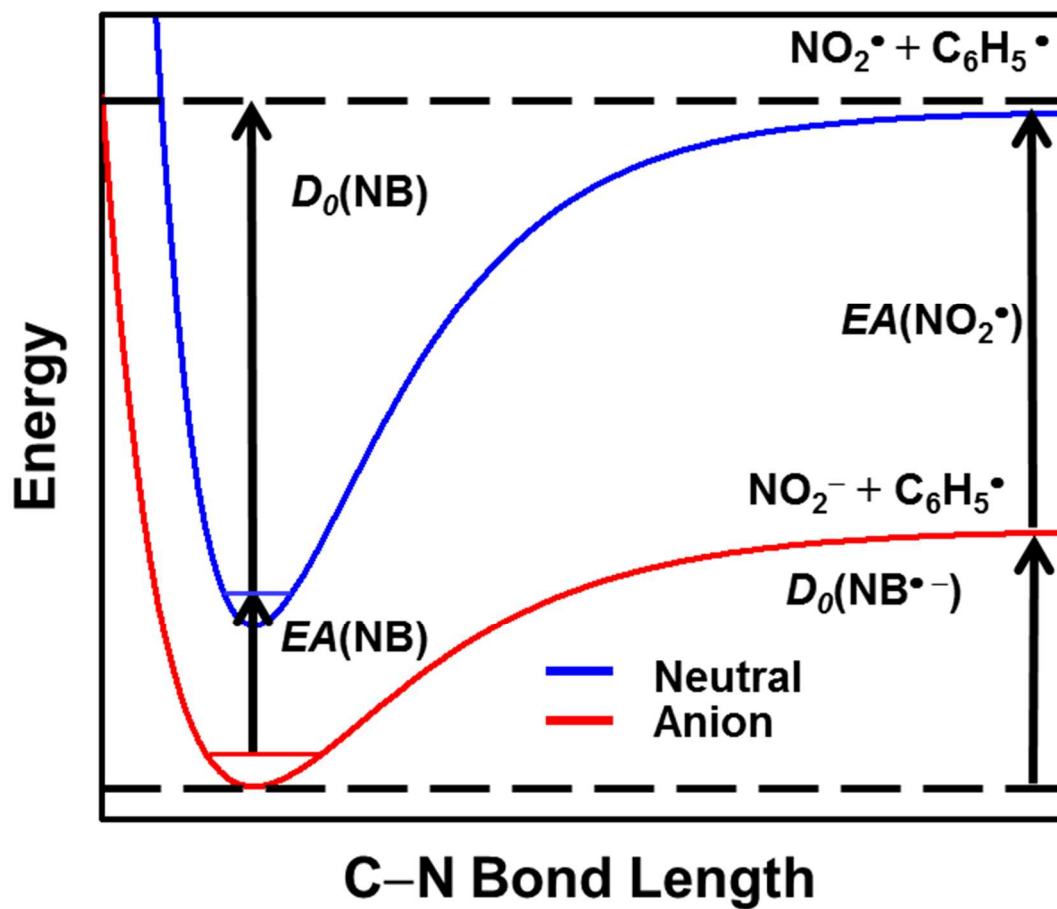


Figure 5.2: Schematic potential energy diagram for nitrobenzene and nitrobenzene radical anion C-N bond cleavage.  $D_0$  corresponds to the dissociation energy of the neutral or anion. EA is the electron affinity of nitrobenzene and  $NO_2$ .

Table 5.1: Experimental thermochemical values measured and used in this work

Thermodynamic Quantity	Energy (eV)	Energy (kJ/mol)	Reference
EA(NB)	$1.01 \pm 0.10$	$97.5 \pm 9.6$	90
	$1.000 \pm 0.010$	$96.49 \pm 0.096$	95
EA ( <i>o</i> -NT)	$0.92 \pm 0.10$	$88.8 \pm 0.96$	90
EA( <i>m</i> -NT)	$0.95 \pm 0.10$	$91.7 \pm 0.96$	90
EA ( <i>p</i> -NT)	$0.99 \pm 0.10$	$95.5 \pm 0.96$	90
EA (NO <sub>2</sub> )	$2.273 \pm 0.005$	$219.3 \pm 0.5$	92
D <sub>0</sub> (NB <sup>-</sup> )	$1.99 \pm 0.16$	$192 \pm 15$	This work
BDE (NB <sup>-</sup> )	0.18*		96
D <sub>0</sub> ( <i>o</i> -NT <sup>-</sup> )	$1.91 \pm 0.14$	$184 \pm 17$	This work
D <sub>0</sub> ( <i>m</i> -NT <sup>-</sup> )	$2.01 \pm 0.17$	$194 \pm 16$	This work
D <sub>0</sub> ( <i>p</i> -NT <sup>-</sup> )	$2.06 \pm 0.21$	$199 \pm 20$	This work
D <sub>0</sub> (NB)	$3.26 \pm 0.18$	$315 \pm 17$	This work
BDE(NB)	3.10	299	93
	$3.10 \pm 0.010$	$299 \pm 1$	87
D <sub>0</sub> ( <i>o</i> -NT)	$3.26 \pm 0.17$	$315 \pm 16$	This work
BDE( <i>o</i> -NT)	$3.04 \pm 0.11$	$293 \pm 11$	87
D <sub>0</sub> ( <i>m</i> -NT)	$3.29 \pm 0.19$	$317 \pm 18$	This work
D <sub>0</sub> ( <i>p</i> -NT)	$3.39 \pm 0.22$	$327 \pm 22$	This work
BDE( <i>p</i> -NT)	$3.10 \pm 0.10$	$299 \pm 10$	87

\*Authors used EA(NO<sub>2</sub>)= 3.91 eV in deriving the bond energy. The recommended value using EA(NO<sub>2</sub>) = 2.273 eV in their previous calculation yields BDE(NB<sup>-</sup>) = 1.82 eV.

## 5.2 Methods

Solutions of *o*- and *m*-nitrotoluene were made by adding ~25  $\mu\text{L}$  of reagent to 50 mL of 50/50 (%v/v) acetonitrile and water mixture. Nitrobenzene and *p*-nitrotoluene solutions were made by dissolving ~0.03 g of solid reagent in 50 mL of the previously described solvent system. To prevent photodecomposition each solution was stored in an amber bottle. All reagents used were purchased from commercial sources and used without further purification.

Each solution was introduced to the APCI source through a syringe pump with a flow rate of 4 $\mu\text{L}/\text{min}$ . The solutions were heated in vaporizer at 225 $^{\circ}\text{C}$  with 60 psi of nitrogen sheath gas. Ions were formed by a corona discharge needle with a constant current of 3 $\mu\text{A}$  (about -1.9 kV). A heated capillary at 125 $^{\circ}\text{C}$  was used to introduce the ions into a medium vacuum (~0.65 Torr) region. A small positive voltage applied to a skimmer extracted anions into a second differentially pumped region. An octapole ion guide was used to collimate the ion beam before the ions entered a high vacuum chamber containing the tandem mass spectrometer. Q1MS spectra were recorded by scanning the first quadrupole while the second and third quadrupoles operated as ion guides. CID spectra were recorded by mass selecting a precursor ion in the first quadrupole. The second octapole acted as a collision cell and was filled with Ar gas (~0.50 mTorr) at high pressure multiple collision conditions. Fragment ions were detected by scanning the third quadrupole. ERMS studies were conducted on fragment ions identified by CID. The pressure inside the collision cell was reduced to  $\leq 0.20$  mTorr to minimize the probability of multiple collisions. After the collision cell all ion optics and voltage offset differences were operated with constant relative differences throughout the collision voltage scans. Each data point reported in the spectra is an average intensity from multiple points across a 1 amu window containing the fragment ion peak. A composite curve was produced by averaging repeated scans

with a 1s dwell time at every collision energy. Normalized ERMS data was compared across multiple days to ensure reproducibility. To eliminate the possibility of isomer interference, all equipment was thoroughly cleaned before changing solutions.

Theoretical calculations were carried out using the Gaussian 09 program suite.<sup>75,76</sup> Energy calculations and geometry optimizations were carried out at the density functional theory (DFT) level using the B3LYP exchange-correlation functional<sup>77,78</sup> and 6-31+G(d),<sup>79</sup> 6-31++G(d,2p),<sup>80</sup> 6-311+G(d),<sup>75</sup> aug-cc-pVDZ<sup>81</sup> basis sets. Unrestricted UB3LYP method was used for species with an unpaired electron. Vibrational frequencies contained no imaginary frequencies, confirming that each structure corresponds to a local minimum.

### 5.3 Threshold Modeling

The energy resolved mass spectra were fit to Eq. (4.2)

$$\sigma(E) = \sigma_0 \sum g_i (E + E_i + E_0)^n / E \quad (4.2)$$

where  $\sigma_0$  is an intensity scaling factor,  $g_i$  is the fraction of ions with internal energy  $E_i$ ,  $E$  is the center-of-mass collision energy of the parent ion,  $E_0$  is the dissociation energy, and  $n$  is an adjustable parameter. Fits were carried out using the CRUNCH4D program.<sup>36</sup> The loss of  $\text{NO}_2^-$  was treated as a loose process using the variational transition state model because there is no barrier along the electronic potential energy surface. Ion kinetic energy distributions were incorporated into the fit by approximating a Gaussian curve with a 1.8 eV (laboratory frame) full width at half-maximum determined by a retarding potential analysis of the parent ion beam. The laboratory energy scale was corrected by locating the offset voltage corresponding to the zero ion kinetic energy from the retarding potential analysis. Deviations between the model function and the experimental threshold were minimized by adjusting the parameters of Eq. (5.2). Rotational

constants and vibrational frequencies of the precursor ions and fragments used in the modeling were taken from B3LYP/6-311+G(d) calculations.

## 5.4 Results and Discussion

### *5.4.1 Collision Induced Dissociation*

Each molecular anion was studied using CID. These CID studies were conducted using collision energies from 0 to 100 eV in the laboratory frame. Each compound produced similar spectra. Only one fragment,  $m/z$  46, corresponding to  $\text{NO}_2^-$ , was observed for each compound. This is characteristic of nitroaromatic compounds.<sup>97</sup> The CID spectra are shown in Figure 5.3. The presence of only  $\text{NO}_2^-$  indicates the nitro-nitrite isomerization and loss of  $\text{NO}^\bullet$  are not favorable for the radical anions of nitrobenzene and nitrotoluene. However, isomerization of the  $\text{NO}_2$  group is known to occur in both the cationic and neutral forms of many nitroaromatic compounds.<sup>85,98</sup> Fragments supporting proton transfer from the methyl groups were not observed. Therefore, of the three pathways in Figure 5.1 for the dissociation of neutral *o*-nitrotoluene, the only important reaction for radical anions is the loss of  $\text{NO}_2^-$ . Our findings are in agreement with the infrared multiphoton dissociation study conducted on these compounds.<sup>94</sup> More complex fragmentation channels have been reported in low energy electron collision studies on dinitrobenzenes.<sup>99</sup> In general, the major fragment observed is  $\text{NO}_2^-$ , but weaker fragments corresponding to loss of  $\text{NO}^\bullet$ ,  $\text{NO}_2^\bullet$ ,  $\text{OH}^\bullet$ ,  $\text{H}^\bullet$ , and  $\text{CH}_3^\bullet$  were also reported depending on the substituents and structure of the nitroaromatic compounds.<sup>99-106</sup>

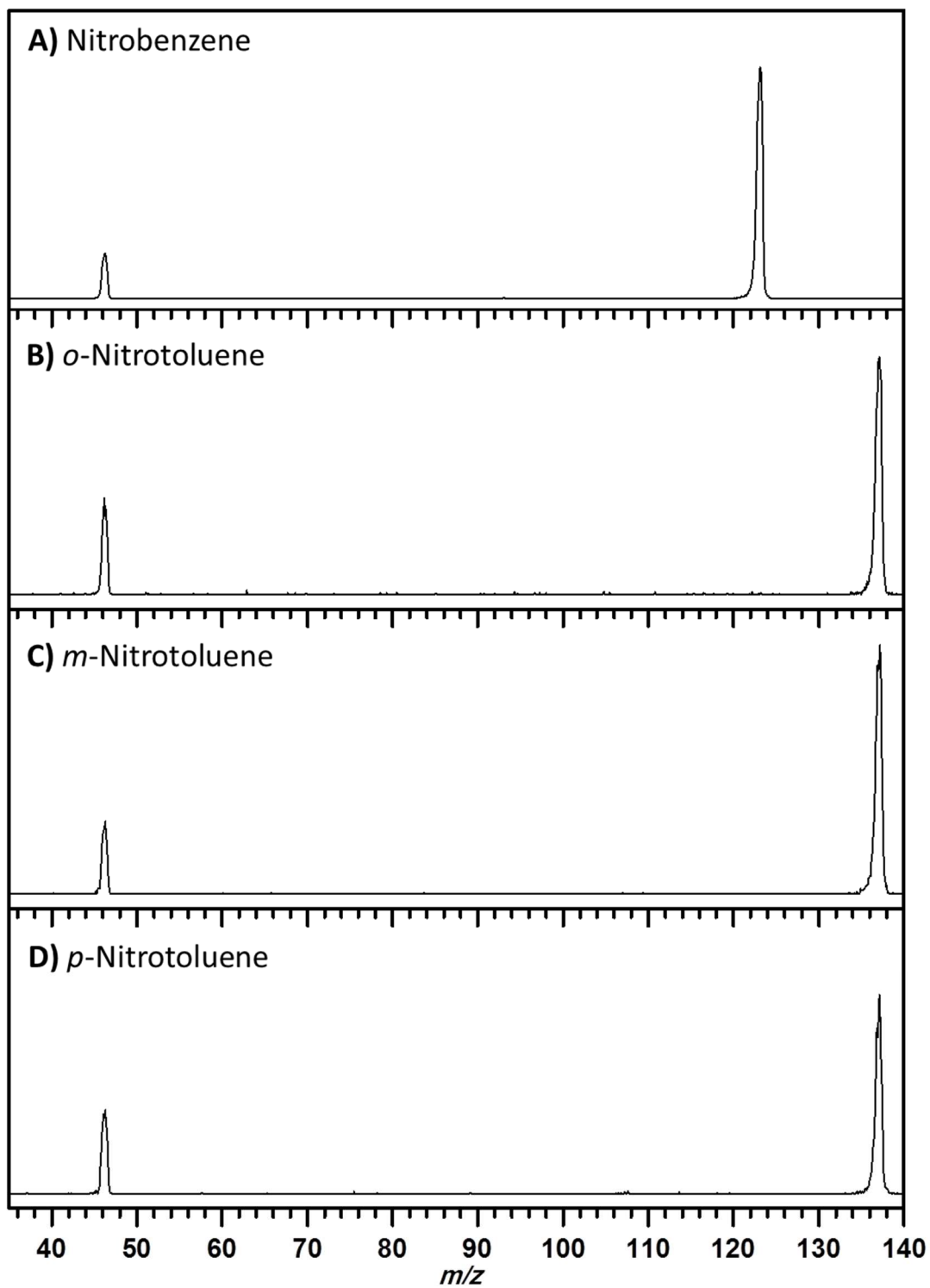


Figure 5.3: CID spectra collected at 30 eV<sub>lab</sub> collision energy for (a) nitrobenzene, (b) *o*-nitrotoluene, (c) *m*-nitrotoluene, and (d) *p*-nitrotoluene.

#### 5.4.2 Anion Dissociation Energies

Figure 5.4 is the energy dependent intensities of  $\text{NO}_2^-$ . Collision energies were converted from the laboratory frame to center-of-mass frame using Eq. (2.1) In Figure 5.3 the solid lines represent convoluted fits to Eq. (5.2). The dashed lines denote the unconvoluted fits. These unconvoluted fits correspond to dissociation energies at 0 K. The energy range was adjusted to fit the onset and steeply rising portion of the data to the model function in Eq. (5.2). Ion collisions outside of the collision cell contribute to the curvature in the low-energy region of the ERMS spectra.<sup>107</sup> Table 5.1 contains the average dissociation energies of nitrobenzene, *o*-nitrotoluene, *m*-nitrotoluene, and *p*-nitrotoluene radical anions from multiple measurements. The reported uncertainties include standard deviations from repeated measurements and uncertainty in the absolute voltage applied to the collision cell. Uncertainties due to experimental factors were accounted for by adjusting the temperature range of the precursor ion from 300 to 500 K, and scaling the experimental time window ( $\sim 5 \times 10^{-5}$  s) by factors of 0.5 and 1.5. The standard deviation of  $E_0$  was also incorporated. This accounts for variations in the energy range used to fit the data. Uncertainties from using theoretical values for the harmonic vibrational frequencies were included by scaling the frequencies by factors of 0.9 and 1.1. Each source of error was treated independently. The dissociation energy of the radical anion of nitrobenzene is  $1.99 \pm 0.16$  eV, *o*-nitrotoluene is  $1.91 \pm 0.14$  eV, *m*-nitrotoluene is  $2.01 \pm 0.17$  eV, and *p*-nitrotoluene is  $2.07 \pm 0.21$  eV. These values are considerably higher than the previously published 0.18 eV dissociation energy for the nitrobenzene anion.<sup>96</sup> However, our reported values are in good agreement with the nitrobenzene dissociation energy, ca. 1.82 eV, calculated from Eq. 5.1 using the electron affinity of  $\text{NO}_2$  reported from photoelectron spectroscopy. Our values are also in

agreement with a previous measurement of nitrobenzene bond dissociation energy<sup>87</sup> and an infrared multiphoton dissociation study on nitrobenzene anion fragmentation.<sup>94</sup>

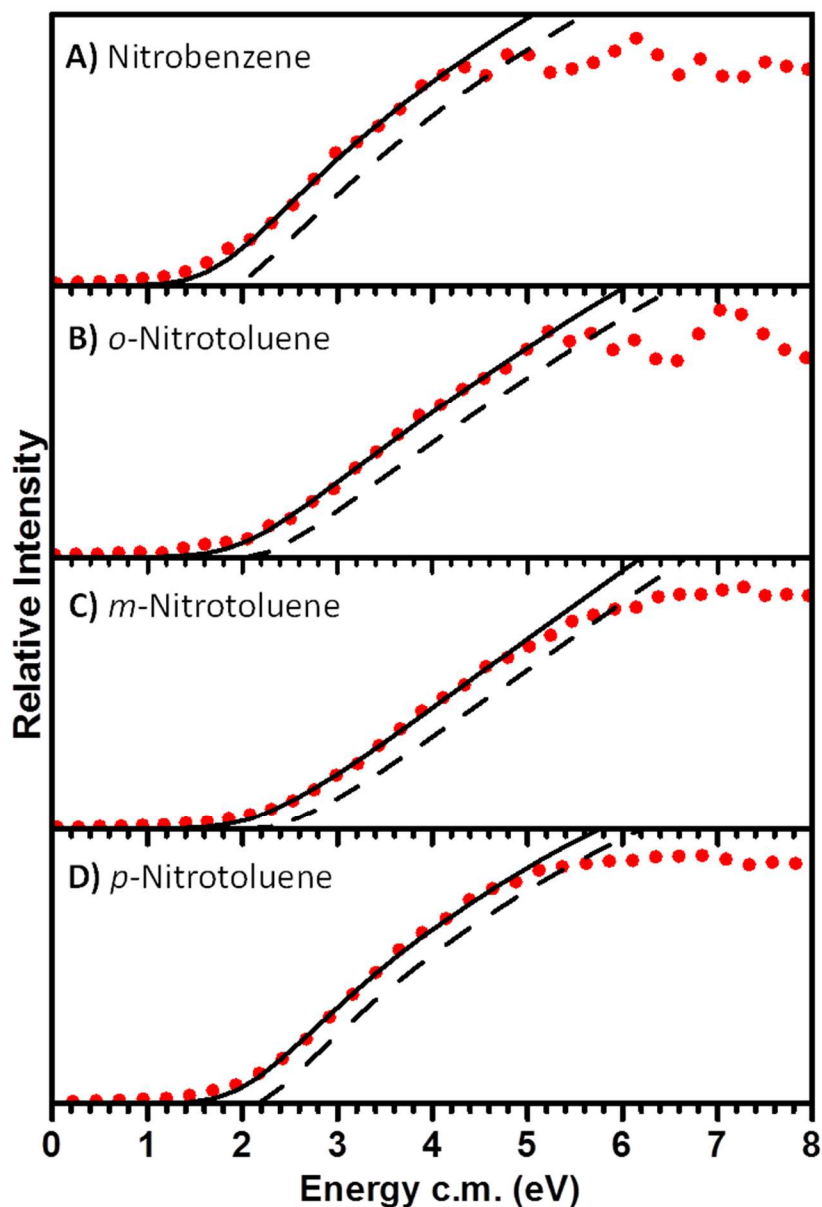


Figure 5.4: ERMS spectra for the formation of  $\text{NO}_2^-$  from (A) nitrobenzene, (B) *o*-nitrotoluene, (C) *m*-nitrotoluene, and (D) *p*-nitrotoluene as a function of collision energy. The solid lines correspond to the convoluted fit and the dashed lines to the unconvoluted fits using Eq. (5.2).

### 5.4.3 Neutral Dissociation Energies

The anion thermochemical cycle, Eq. (5.1), is completed with the experimental C-N dissociation energies of the nitrobenzene and nitrotoluene radical anions. Table 5.2 contains the dissociation energies of neutral nitrobenzene, *o*-nitrotoluene, *m*-nitrotoluene, and *p*-nitrotoluene. The EAs were taken from gas-phase equilibrium reactions.<sup>90</sup> The EA of NO<sub>2</sub><sup>•</sup> was taken from an anion photoelectron spectroscopy experiment.<sup>92</sup> The dissociation energy of neutral nitrobenzene is  $3.26 \pm 0.18$  eV, *o*-nitrotoluene is  $3.26 \pm 0.17$  eV, *m*-nitrotoluene is  $3.29 \pm 0.19$  eV, and *p*-nitrotoluene is  $3.39 \pm 0.22$  eV. The reported dissociation energies are all within experimental uncertainty of one another. This indicates the relative position of the methyl substituent on the aromatic ring has a negligible effect on the C-N bond dissociation energy. Our reported values are slightly higher than the previously reported experimental dissociation energies. It is important to note we are reporting energy differences. The reported values are not bond dissociation enthalpies, which account for differences in integrated heat capacities of the products and reactants. This suggests there could be a source of bias in our experiment. The gradual, rather than abrupt, onset makes fitting the threshold region of the experimental data to Eq. (5.2) challenging. This bias could arise from fitting the threshold region of the appearance curves. According to Eq. (5.1) the neutral bond energies will contain a systematic error if the threshold energies are too large.

Comparison between the reported neutral and anion dissociation energies show dissociation of the radical anions is approximately 1.3 eV lower in energy than the dissociation energy for the corresponding neutrals. Differences in the EAs dictate the differences in the BDEs according to Eq. (5.1). The bond energy in the anion is reduced due to the excess electron occupying an anti-bonding orbital. This corresponds to a reduction in the bond order. If a radical

anion is formed in the first steps of decomposition the energy required for bond dissociation is significantly lower than the neutral molecule. This suggests anions could be an important source of reactive intermediates in the decomposition process.

#### *5.4.4 Theoretical Comparison*

Theoretical bond dissociation energies are listed in Table 5.2 along with the reported experimental dissociation energies calculated using ion thermochemical values. The theoretical dissociation energies were calculated using the DFT method at the B3LYP level. Rough agreement is found between the experimental dissociation energies and the calculated B3LYP energies. However, our experimental dissociation energies and previous measurements are consistently larger than the theoretical values. The source of this error could be theoretical or experimental in nature. One way to address this issue is to compute the individual energies associated with each process in the anion thermochemical cycle, Eq. (5.1). Table 5.3 shows the electron affinities calculated for the nitroaromatic compounds of interest to this chapter and  $\text{NO}_2$ . The theoretical electron affinities deviate, on average, 0.3 eV from experimental values. This suggests the level of theory employed in this work does not accurately describe the electronic structure of the radical anions. The open-shell nature of nitroaromatic radical anions is not adequately described by a standard single determinant method. Therefore, rigorous multi-reference calculations are needed to accurately describe these systems. Such calculations are beyond the scope of this work. The reported theoretical energies should only be used as a rough estimation of the bond energies.

Table 5.2: Experimental and theoretical values for the dissociation energies,  $D_0$ , (eV) of nitrobenzene (NB) and nitrotoluene (NT) isomers.

	Experiment	B3LYP/ 6-31+G(d)	B3LYP/ 6-31++G(d,2p)	B3LYP/ 6-311+G(d)	B3LYP/ aug-cc-pVDZ
<i>Anions</i>					
NB	$1.99 \pm 0.16$	1.83	1.85	1.82	1.87
<i>o</i> -NT	$1.91 \pm 0.14$	1.61	1.63	1.60	1.68
<i>m</i> -NT	$2.01 \pm 0.17$	1.80	1.82	1.80	1.84
<i>p</i> -NT	$2.06 \pm 0.21$	1.81	1.83	1.80	1.85
<i>Neutrals</i>					
NB	$3.26 \pm 0.18$	2.91	2.91	2.85	2.89
<i>o</i> -NT	$3.26 \pm 0.17$	2.78	2.78	2.72	2.79
<i>m</i> -NT	$3.29 \pm 0.19$	2.92	2.92	2.86	2.90
<i>p</i> -NT	$3.39 \pm 0.22$	2.96	2.96	2.90	2.94

Table 5.3: Calculated electron affinities, EA, (eV) for nitrobenzene, nitrotoluene isomers, and nitrogen dioxide.

	Experiment	B3LYP/ 6- 31+G(d)	B3LYP/ 6-31++G(d,2p)	B3LYP/ 6-311+G(d)	B3LYP/ aug-cc-pVDZ	Reference
NB	$1.000 \pm 0.010$	1.29	1.30	1.29	1.29	90
<i>o</i> -NT	$0.92 \pm 0.10$	1.19	1.21	1.20	1.20	90
<i>m</i> -NT	$0.95 \pm 0.10$	1.24	1.26	1.26	1.25	90
<i>p</i> -NT	$0.99 \pm 0.10$	1.21	1.22	1.22	1.21	90
NO <sub>2</sub>	$2.273 \pm 0.005$	2.36	2.36	2.32	2.30	92

#### 5.4.5 Electron Detachment

Table 5.1 shows the bond dissociation energies of the nitroaromatic compounds are approximately twice as large as the reported EAs. The low magnitude of the EAs indicates internally excited anions can release energy by fragmentation or electron emission (electron auto-detachment). These two processes can occur on the same timescale, meaning auto-detachment should be competitive with bond dissociation. A statistical rate analysis suggests at low energies competition is critical, however, at higher energies, dissociation is the dominant process.<sup>94</sup> A competitive shift in the appearance energy of  $\text{NO}_2^-$  must be considered because the energy threshold for auto-detachment is so much lower than the reported bond dissociation energy. The competitive shift would produce a slight upward shift in the apparent dissociation energy threshold. Previous work suggests competitive shifts are important in cases when the difference in bond energy and EA exceed approximately 1 eV. Table 5.1 shows the difference between the anion dissociation energies and EAs of the nitroaromatic compounds are within the range at which competitive auto-detachment is thought to be important. Therefore, a competitive shift could be responsible for the higher apparent dissociation energies. Unfortunately, our instrumentation has no method to detect electron auto-detachment, so modeling the data in Figure 5.2 cannot account for competitive effects.

#### 5.5 Conclusions

CID and ERMS studies were carried out on nitrobenzene, *o*-nitrotoluene, *m*-nitrotoluene, and *p*-nitrotoluene anions. CID spectra for each anion showed the formation of only one fragment,  $\text{NO}_2^-$ , under all conditions. This shows other decomposition pathways, such as loss of  $\text{NO}^\bullet$  and nitro-to-nitrite isomerization, are only important in the cationic and neutral forms of the

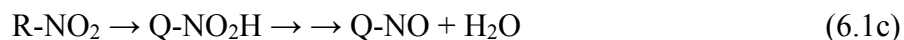
nitroaromatic compounds studied. C-N bond dissociation energies for each nitroaromatic radical anion were determined from appearance threshold analysis of the  $\text{NO}_2^-$  fragment. Reported dissociation energies for the radical anions were approximately 2 eV. Dissociation energies were also calculated using the thermochemical cycle for the corresponding neutral compounds. Experimental results indicate the relative position of the methyl substituent on the aromatic ring has a negligible effect on the C-N dissociation energies. The relative strength of the C-N bond is approximately the same for nitrobenzene and the three isomers of nitrotoluene. Nitrotoluene radical anions have significantly lower C-N bond dissociation energies in comparison to the corresponding neutrals. This can be attributed to the placement of the excess electron in to an anti-bonding orbital.

## CHAPTER 6

### FRAGMENTATION OF DEPROTONATED NITROPHENOL ANIONS

#### 6.1 Introduction

Many high energy compounds are known to have particularly high shock sensitivities. Studies have proposed molecular level bond energies are a reflection of the shock sensitivity of these compounds.<sup>10,88,96,108-112</sup> Polynitrophenols, such as picric acid, are especially shock sensitive and reactive energetic materials. The acidity of the alcohol substituent is affected by the nitro group. The pK<sub>a</sub> of picric acid, 0.38, indicates it is a strong acid and will readily lose a proton to form a stable anion. It is reasonable then to expect a significant fraction of the molecules will be present in their ionic form. Therefore, it is interesting to investigate the decomposition energetics of the deprotonated anions to better understand the detonation process. Numerous theoretical studies have been conducted on the unimolecular decomposition of nitroaromatics.<sup>10,11,85,113-116</sup> Three common low energy reactions have been identified, Eq. (6.1):



A rearrangement of the nitro group to the nitrite structure on the aromatic ring, R, followed by the elimination of NO<sup>•</sup> is indicated by Eq. 6.1a. The direct dissociation of the C-N bond to produce NO<sub>2</sub><sup>•</sup> is reported by Eq. 6.1b. The final equation, Eq. 6.1c, involves an H-abstraction from the nitroaromatic species to produce a radical, Q, eventually leading to the loss of water by

additional H-atom abstractions. All three processes have been predicted to occur at low energies.<sup>85,114,115,117</sup> Properties and relative locations of the substituents on the aromatic ring affect the energetics of these processes. To better understand these fragmentation pathways, we investigated the fragmentation of deprotonated *ortho*-, *meta*-, and *para*-nitrophenol.<sup>1</sup> These compounds were chosen as simple analogs of polynitrophenols. The information gathered during this study of isolated molecules could help facilitate better understanding of the bulk-phase properties of these compounds.

## 6.2 Methods

This study was carried out using the mass spectrometer described in Chapter 2. HPLC grade acetonitrile and 18.2 M $\Omega$  deionized water in a 50:50 by volume ratio was used to make nitrophenol solutions at a ~0.6 mg/mL concentration. Each isomer in this study was studied over multiple days. All equipment was thoroughly cleaned and dried between studies to reduce the possibility of interference from the other isomers.

Ions were generated using the atmospheric pressure chemical ionization source described in Chapter 2. The vaporizer temperature was 150 – 200°C. The corona current was held constant at 5.0  $\mu$ A. Anions were sampled by the heated capillary at 200°C. A skimmer and ion optics collimated the ion beam. Ions were detected by a channeltron electron multiplier. Collision induced dissociation studies were done initially. Specific anions of interest were later studied using energy resolved mass spectrometry. These two techniques were described in Chapter 2. The collision gas pressure was no more than 0.25 mTorr for the CID studies. This was done to minimize the probability of multiple collisions.

Theoretical calculations were carried out using the Gaussian 09 program suite.<sup>75,76</sup> Geometry optimization and energy calculations were carried out at the density functional theory (DFT) level using the B3LYP exchange-correlation functional<sup>77,78</sup> and the aug-cc-pVDZ<sup>81</sup> basis set. The vibrational frequency calculations did not result in imaginary frequencies, confirming each structure corresponds to a local minimum. Unrestricted UB3LYP method was used for species with an odd number of electrons. Transition states had a single imaginary frequency, corresponding to motion along the reaction coordinate.

## 6.3 Results and Discussion

### 6.3.1 Collision Induced Dissociation

Figure 6.1 shows CID spectra for the three deprotonated nitrophenol anions. Three common fragments were observed for all isomers,  $m/z$  46 ( $\text{NO}_2^-$ ), 92 ( $\text{C}_6\text{H}_4\text{O}^{\bullet-}$ ), and 108 ( $\text{C}_6\text{H}_4\text{O}_2^{\bullet-}$ ). The CID spectrum for *o*-nitrophenoxide shows two minor fragments with very low intensity at  $m/z$  64 ( $\text{C}_5\text{H}_4^{\bullet-}$ ) and 80 ( $\text{C}_5\text{H}_4\text{O}^{\bullet-}$ ). The fragment  $\text{C}_6\text{H}_4\text{O}_2^{\bullet-}$  is noted to have a lower relative intensity than the  $\text{C}_5\text{H}_4\text{O}^{\bullet-}$  fragment in the CID spectrum of *m*-nitrophenoxide. No low intensity fragments were identified in the CID spectrum of *p*-nitrophenoxide.

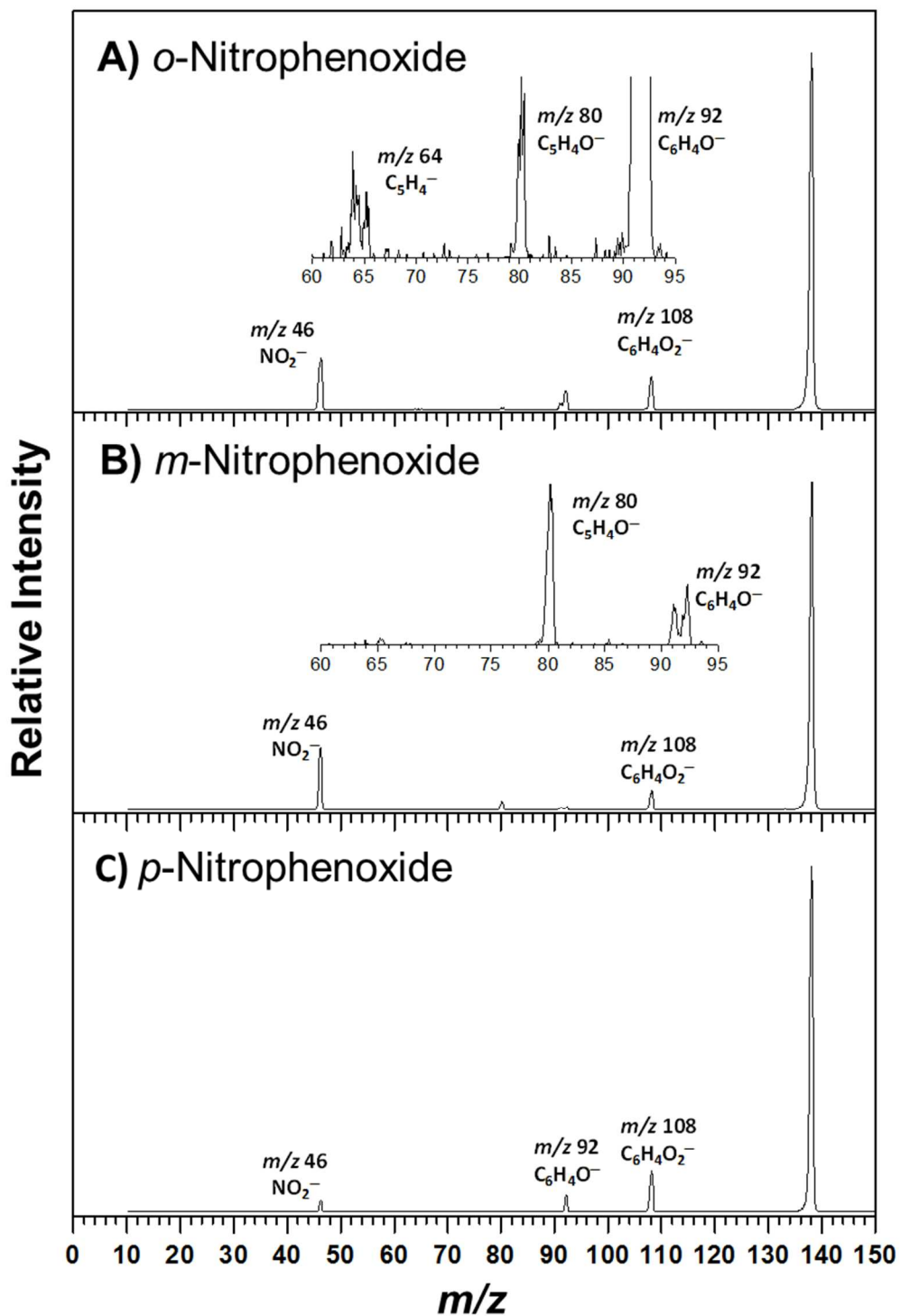


Figure 6.1: Collision induced dissociation spectra of (A) *o*-nitrophenoxide, (B) *m*-nitrophenoxide, and (C) *p*-nitrophenoxide at 20 eV<sub>lab</sub> collision energy with 0.250 mTorr Ar collision gas.

### 6.3.2 Energy Resolved Mass Spectrometry

Fragment ions identified in the CID studies were further investigated using ERMS. Figure 6.2 contains the ERMS spectra for each isomer. The lowest energy fragment is  $C_6H_4O_2^{\bullet-}$  for all isomers. For *o*-nitrophenoxide and *m*-nitrophenoxide,  $C_6H_4O_2^{\bullet-}$  has an appearance energy between 2 and 3 eV with a maximum intensity around 5 eV. A similar appearance energy is recorded for the *p*-nitrophenoxide isomer with a maximum intensity at 6 eV. Fragment  $C_6H_4O^{\bullet-}$  has an appearance energy between 3 – 4 eV for all isomers. The  $NO_2^-$  fragment has an appearance energy of approximately 3 – 3.5 eV for both *o*-nitrophenoxide and *m*-nitrophenoxide, and 4 eV for *p*-nitrophenoxide. Fragments  $C_6H_4O^{\bullet-}$  and  $NO_2^-$  have similar onset profiles. However, at higher collision energies the relative intensity of  $C_6H_4O^{\bullet-}$  increases slower than  $NO_2^-$ .  $C_5H_4O^{\bullet-}$  also has a comparable onset to  $NO_2^-$  in the *o*-nitrophenoxide and *m*-nitrophenoxide isomers. The appearance energy of  $C_5H_4O^{\bullet-}$  is around 3 – 4 eV for the *ortho* isomer. The low relative intensities of  $C_6H_4O^{\bullet-}$  and  $C_5H_4O^{\bullet-}$  suggests the fragments result from secondary fragmentation of  $C_6H_4O_2^{\bullet-}$ , corresponding to loss of CO and  $CO_2$ .

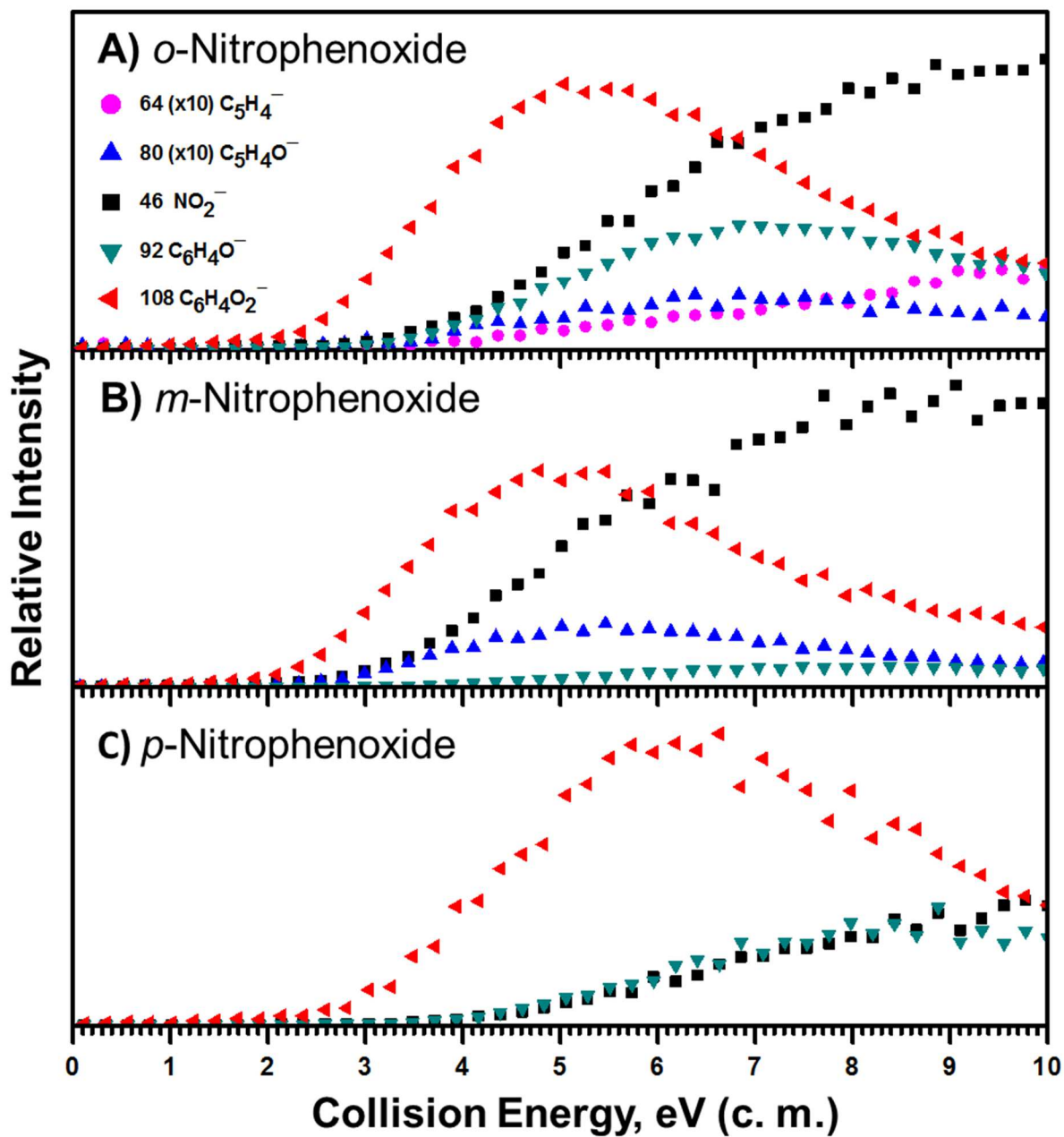


Figure 6.2: Energy resolved mass spectra for the fragmentation of (A) *o*-nitrophenoxide, (B), *m*-nitrophenoxide, and (C) *p*-nitrophenoxide. The collision energy has been converted to center-of-mass frame using Eq. (2.1).

### 6.3.3 Theoretical Calculations

The critical points on the potential energy diagram for the dissociation of *o*-nitrophenoxide to produce the five experimentally observed fragments are shown in Figure 6.3. All energies are relative to *o*-nitrophenoxide and are reported in eV. Zero point energy corrections are included. The lowest energy pathway is calculated to be the loss of NO• to form C<sub>6</sub>H<sub>4</sub>O<sub>2</sub>•<sup>-</sup>. Elimination of NO• is only possible if the nitro group undergoes a rearrangement to the nitrite structure. A rearrangement barrier of 2.44 eV was calculated. The rearranged nitrite structure is only 0.38 eV higher in energy than the nitro structure. A tight transition state for the rearrangement is indicated by the C–N separation (1.57 Å) at the transition state geometry. The transition state structure combines the in-plane and out-of-plane rotation of the NO<sub>2</sub> group. The NO group lies above the plane of the aromatic ring in the optimized nitrite structure. Relative to the nitrite structure, elimination of NO• is calculated to require only 0.08 eV. Rearrangement of the nitro substituent is calculated to be the rate limiting step in the formation of C<sub>6</sub>H<sub>4</sub>O<sub>2</sub>•<sup>-</sup>. Loss of NO• is spontaneous following the rearrangement of the substituent.

Additional pathways were calculated for the fragment ions C<sub>6</sub>H<sub>4</sub>O•<sup>-</sup> and NO<sub>2</sub><sup>-</sup>. The loss of NO<sub>2</sub>• to produce C<sub>6</sub>H<sub>4</sub>O•<sup>-</sup> is calculated to require 3.48 eV. The loss of NO<sub>2</sub><sup>-</sup> requires 3.46 eV. The formation of these fragment ions occurs through a bond cleavage with a competition between the two fragments for the excess electron. The relative branching ratios for the two products should be similar. The neutral product formed after the loss of NO<sub>2</sub><sup>-</sup> is unstable and rearranges from a six-membered ring to a five-membered ring. This rearrangement is due to the zwitterionic nature of the neutral product generated by heterolytic bond cleavage. Zwitterionic species are generally unfavorable in the gas phase; therefore the theoretical prediction of a rearrangement to a non-zwitterionic structure is reasonable.

The formation of the two minor fragments  $C_5H_4O^{\bullet-}$  and  $C_5H_4^{\bullet-}$ , from the loss of CO and  $CO_2$  respectively, were also calculated. Dissociation of aromatic ions with CO bonds is known to produce these characteristic fragments.<sup>85,118-120</sup> The structures calculated for the minor fragments are in agreement with previously proposed structures for  $C_5H_4O^{\bullet-}$  and  $C_5H_4^{\bullet-}$ . The low relative intensities of these secondary fragments suggest the rates of formation for these ions are slow. It is also possible these ions form from multiple collisions. These secondary fragments were not further studied.

The potential energy diagram for *m*-nitrophenoxide is shown in Figure 6.4. The  $NO_2/ONO$  rearrangement barrier is calculated to be 2.48 eV. A similar barrier was calculated for *o*-nitrophenoxide. This barrier also corresponds to the formation of the lowest energy product,  $C_6H_4O_2^{\bullet-}$ , from the elimination of  $NO^{\bullet}$ . The optimized nitrite structure is calculated to be 0.29 eV higher in energy than the precursor ion, but is still significantly below the calculated isomerization barrier. The predicted energy for the formation of  $NO_2^-$  is 3.42 eV, whereas the energy for the formation of  $C_6H_4O^{\bullet-}$  is 3.29 eV. Both energies are similar to those calculated for *o*-nitrophenoxide.

Figure 6.5 is the potential energy diagram for the *p*-nitrophenoxide isomer. The barrier for the nitro-to-nitrite rearrangement is calculated to be 2.86 eV. The formation of  $NO_2^-$  is predicted to require 3.85 eV, whereas the formation of  $C_6H_4O^{\bullet-}$  is predicted to require 4.00 eV. The theoretical dissociation energies for *p*-nitrophenoxide are consistently higher than the energies calculated for similar reactions for *o*-nitrophenoxide and *m*-nitrophenoxide.

# *o*-Nitrophenoxide

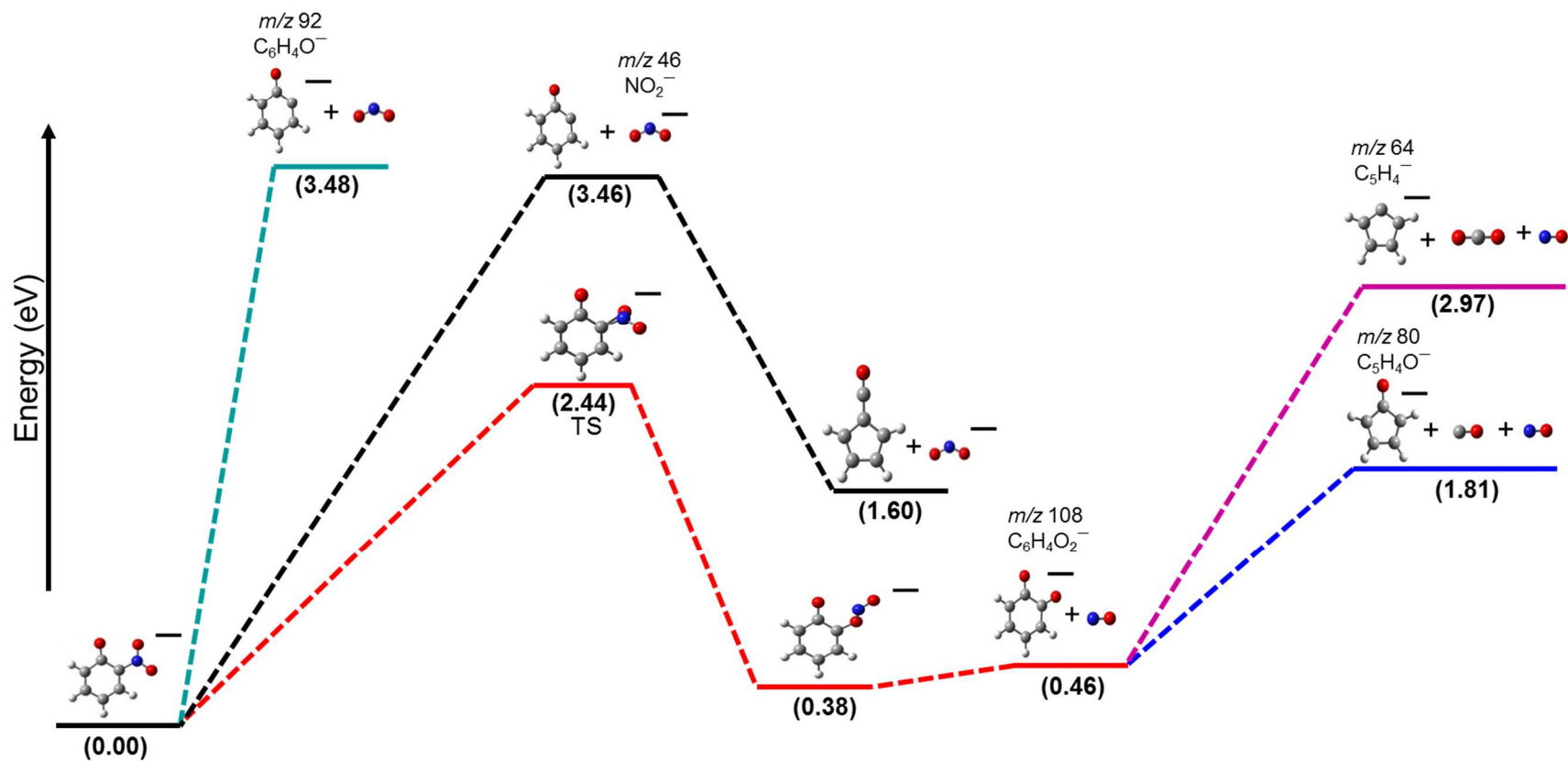


Figure 6.3: Calculated potential energy diagram for the dissociation of *o*-nitrophenoxide anion at the B3LYP/aug-cc-pVDZ level of theory. The cyan pathway corresponds to loss of  $NO_2^\bullet$ . The black pathway corresponds to loss of  $NO_2^-$ . The red pathway corresponds to the rearrangement of the nitro group followed by the loss of  $NO^\bullet$ . Minor fragmentation pathways are reported in magenta and blue.

## *m*-Nitrophenoxide

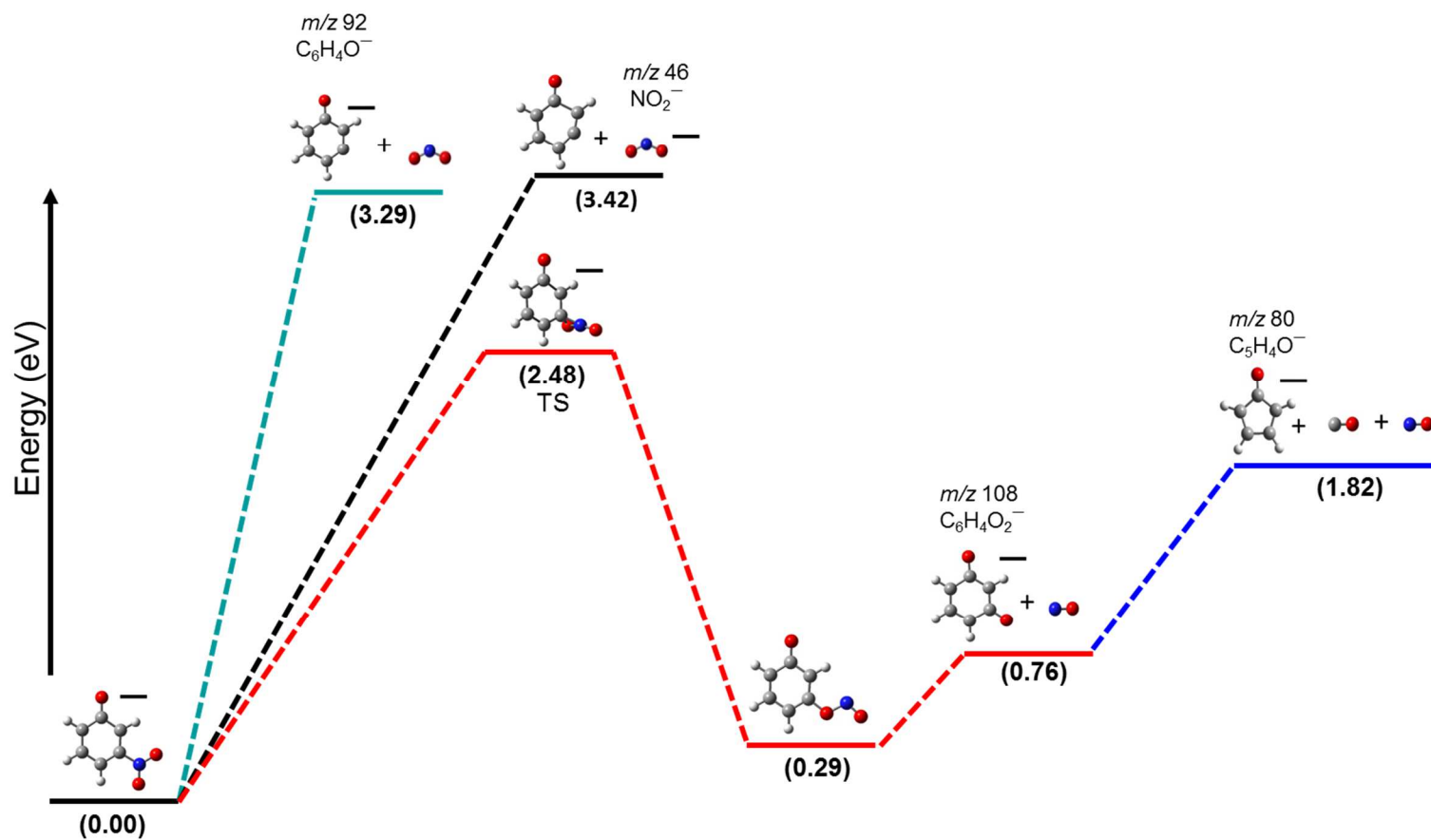


Figure 6.4: Calculated potential energy diagram for the dissociation of *m*-nitrophenoxide anion at the B3LYP/aug-cc-pVDZ level of theory. The cyan pathway corresponds to loss of  $\text{NO}_2^\bullet$ . The black pathway corresponds to loss of  $\text{NO}_2^-$ . The red pathway corresponds to the rearrangement of the nitro group followed by the loss of  $\text{NO}^\bullet$ .

## *p*-Nitrophenoxide

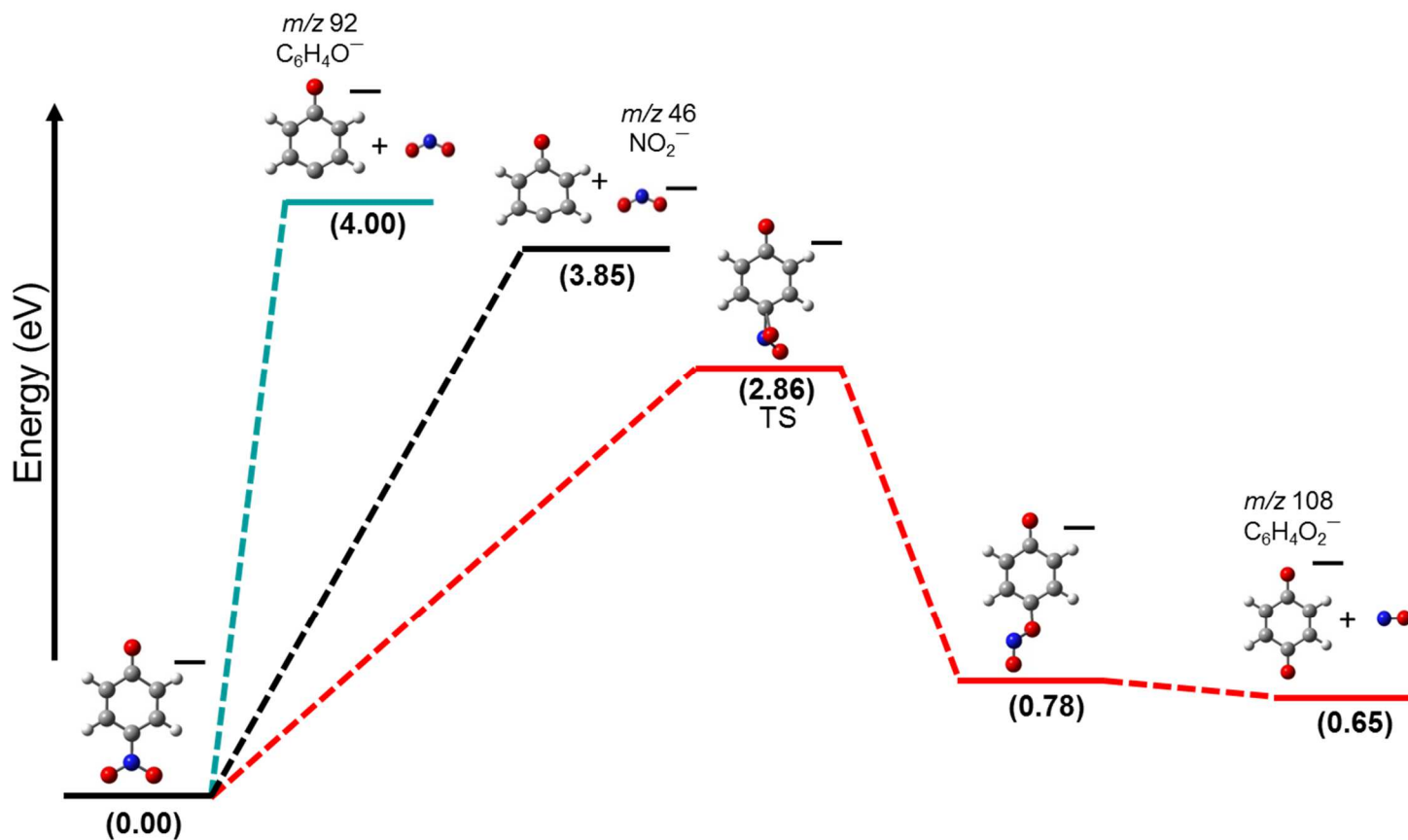


Figure 6.5: Calculated potential energy diagram for the dissociation of *p*-nitrophenoxide anion at the B3LYP/aug-cc-pVDZ level of theory. The cyan pathway corresponds to loss of  $\text{NO}_2^\bullet$ . The black pathway corresponds to loss of  $\text{NO}_2^-$ . The red pathway corresponds to the rearrangement of the nitro group followed by the loss of  $\text{NO}^\bullet$ .

#### 6.3.4 Experimental and Theoretical Comparison

Theory predicts the formation of  $C_6H_4O_2^{\bullet-}$ , resulting from the loss of  $NO_2^{\bullet}$ , will be the lowest energy dissociation pathway in deprotonated *o*-nitrophenol. The experimental appearance energy of  $C_6H_4O_2^{\bullet-}$ , 2 - 2.5 eV, and the barrier height for the formation of  $C_6H_4O_2^{\bullet-}$ , 2.44 eV, calculated in Figure 5.3 are in good agreement. Similar agreement is found for the appearance energy of  $NO_2^-$ , 3 - 3.5 eV, and the theoretical dissociation energy of 3.46 eV. This is significantly different than the dissociation energies observed for nitrotoluene radical anions.<sup>2</sup> According to theoretical calculations, the rearrangement barrier for the nitrotoluene radical cations is higher than C-N bond dissociation energies. Additionally, the loss of  $NO^{\bullet}$  is predicted to be unfavorable for the nitrotoluene species due to a tight transition state. Competitive loss of  $NO^{\bullet}$  and  $NO_2^-/NO_2^{\bullet}$  was observed in this study. The rearrangement process resulting in loss of  $NO^{\bullet}$  is favored at low collision energies, whereas the loss of  $NO_2^-/NO_2^{\bullet}$  is favored at higher collision energies due to the loose transition state. Good agreement is also found between the appearance energy, 3 - 3.5 eV and the theoretical dissociation energy, 3.48 eV, for the third most intense fragment,  $C_6H_4O^{\bullet-}$ .

Similar agreement between experiment and theory are found for both *m*-nitrophenoxide and *p*-nitrophenoxide. The major discrepancies for *m*-nitrophenoxide are in regards to  $C_5H_4O^{\bullet-}$  and  $C_6H_4O^{\bullet-}$ . The relatively high intensity of  $C_5H_4O^{\bullet-}$  is attributed to secondary fragmentation, meaning it could arise from multiple processes including a second collision with the target gas or sequential dissociation from an internally excited fragment. This makes comparison between the experimental appearance energy and the calculated relative energy of the product invalid. Theoretical calculations predict  $C_6H_4O^{\bullet-}$  has a lower dissociation energy than  $NO_2^-$ . Therefore,  $C_6H_4O^{\bullet-}$  would be expected to have a larger relative intensity than  $NO_2^-$ , especially since both

products form as a result of C-N dissociation with a loose transition state. However,  $\text{NO}_2^-$  is significantly more intense. No secondary products were observed for  $\text{C}_6\text{H}_4\text{O}^{\bullet-}$  to account for the low intensity of the fragment. One possible explanation for this discrepancy could be an error in the theoretical energies as a result of using a single determinant wavefunction to describe open-shell species. Decay into a dark channel could also explain the low intensity of the  $\text{C}_6\text{H}_4\text{O}^{\bullet-}$  fragment. For example, spontaneous electron emission could occur if  $\text{C}_6\text{H}_4\text{O}^{\bullet-}$  has a low electron binding energy. The resulting neutral formation could explain the low intensity of the  $\text{C}_6\text{H}_4\text{O}^{\bullet-}$  fragment. Experimental values for the electron binding energy of  $\text{C}_6\text{H}_4\text{O}^{\bullet-}$  are not currently available. However, to explore this avenue theoretical electron binding energies were calculated for  $\text{C}_6\text{H}_4\text{O}^{\bullet-}$ . For electron detachment from  $\text{C}_6\text{H}_4\text{O}^{\bullet-}$ , DFT theory predicts the triplet state is the lowest energy form of each neutral isomer. Electron affinities calculated at the B3LYP/aug-cc-pVDZ level of theory predict the electron affinity of the *meta*- isomer to be 1.6 eV, whereas the electron affinities for the *ortho*- and *para*- isomers were predicted to be 2.3 eV and 2.2 eV, respectively. It is important to note the predicted electron affinity of the *meta*- isomer is lower, however, the difference is not sufficient to account for the difference in observed ion intensity.

Good agreement is observed between experiment and DFT calculations for the fragmentation of *p*-nitrophenoxide. In comparison to the *ortho*- and *meta*- isomers, small increases in the appearance energies for the major fragments were observed. Theoretical calculations predicted an increase of similar magnitude in the dissociation energies. Overall, good agreement between the observed appearance energies and theoretical dissociation energies was obtained for all three nitrophenoxide isomers. In general, experiment and theory show the loss of  $\text{NO}^\bullet$  is the lowest energy fragmentation reaction for all three nitrophenoxide ions even though the reaction involves a tight transition state.

### 6.3.5. Analysis of C-N Dissociation Energies

The discussion of this work is concluded by a brief comparison to the previous study concerning the dissociation of nitrotoluene radical anions.<sup>2</sup> According to both experiment and theory, the C-N dissociation energy to produce  $\text{NO}_2^-$  is approximately 3 – 4 eV for all three nitrophenoxide isomers.<sup>1</sup> The relative substituent position appears to have no significant influence on these dissociation energies. This is expected because the C-N bond is a  $\sigma$  bond, which is independent of relative substituent position. Inductive effects could occur, but this work suggests these effects are minor. These findings are consistent with the previous study of nitrotoluene and nitrotoluene radical anions, discussed in Chapter 4. The reported C-N bond dissociation energies for the nitrotoluene species were all identical, approximately 2 eV.<sup>2</sup> It appears within a similar class of nitroaromatic compounds, the C-N bond energies are independent of substituent position. However, the relative magnitude of C-N bond energies is influenced by the type of substituent. This could have an important effect on the lowest energy fragmentation pathway – rearrangement or direct bond cleavage. The lowest energy fragmentation product is the greatest difference in the fragmentation of the nitrophenoxides compared to the nitrotoluene radical anions. The lowest energy product for nitrotoluene radical anions is  $\text{NO}_2^-$  as a result of C-N bond cleavage, whereas loss of  $\text{NO}^\bullet$  after rearrangement is the lowest energy product for the nitrophenoxides.

The differences in magnitude of the C-N bond energies for the nitrophenoxides compared to nitrotoluene anions can be attributed to two effects. Firstly, the excess electron occupies a  $\pi^*$  orbital in the nitrotoluene radical anions. This results in partial destabilization of the molecule. The excess electron is localized on the nitro group and the position of this charge weakens the nearby C-N bond compared to neutral nitrotoluene. In the nitrophenoxides, the excess electron

resides primarily on the oxygen atom, but can be delocalized through the  $\pi$  system as shown in Figure 6.6. Structure A is the dominant nitrophenoxide resonance structure. In this structure, the excess electron occupies a non-bonding  $\pi$  orbital. Due to the delocalization of the excess electron in a non-bonding  $\pi$  orbital, the C-N bond dissociation energies are not expected to decrease as a result of deprotonation. C-N bond energies are not available for direct comparison to experimental energies for the neutral nitrophenoxide compounds. To address this issue, DFT calculations were carried out on the neutral nitrophenoxides. A slight increase in the dissociation energy was noted for the deprotonated nitrophenol anions in comparison to the neutral nitrophenol compounds. In the nitrotoluene radical anions the C-N dissociation energies decrease compared to the neutral nitrotoluenes. These results are reported in Table 6.1. The increase in the C-N dissociation energies for the nitrophenoxide anions can be attributed to the resonance stabilization of the excess electron in the  $\pi$  system, Figure 6.6 structure (b), which results in stronger  $\pi$ -bonding between the C-N atoms in the anion relative to the neutral nitrophenols. Arguments could also be made that the increased ionic character, Figure 6.6 structure (c), of the nitrophenoxide is responsible for the increased C-N dissociation energy of the anion compared to the neutral. The resonance structures in Figure 6.6 provide a means to rationalize the increased C-N bond energies; however, analysis of these resonance structures is beyond the scope of this work.

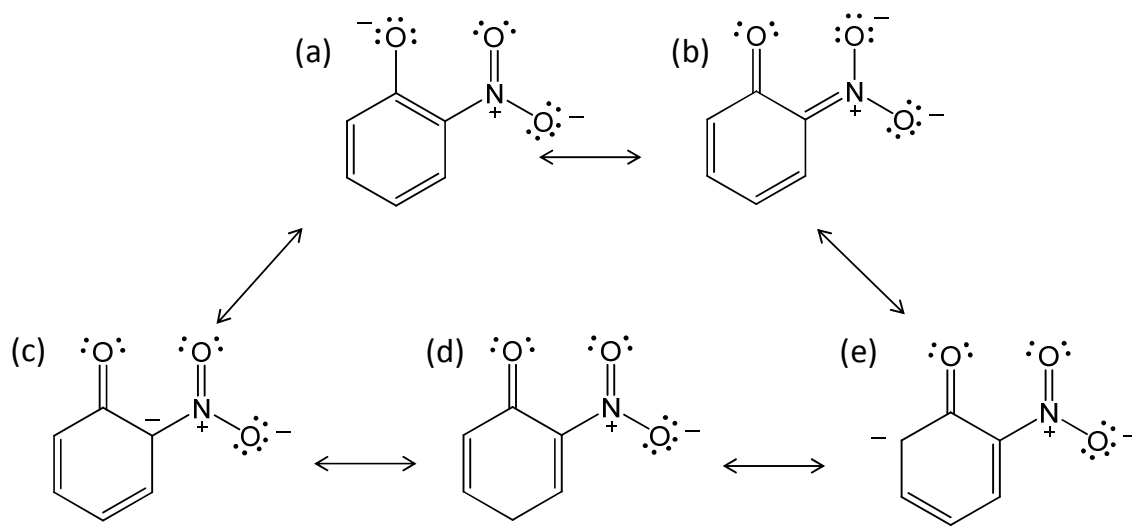


Figure 6.6: Resonance structures of *o*-nitrophenoxide illustrating resonance stabilization of the excess electron.

Table 6.1: Theoretical dissociation energies for the elimination of  $\text{NO}_2^-$  from neutral nitrophenols (NP), deprotonated nitrophenols (NP-H<sup>-</sup>), and nitrobenzene (NB) or nitrotoluene (NT) neutrals and anions calculated at the B3LYP/aug-cc-pVDZ level of theory.

Anions	C-N Dissociation Energy (eV)	Neutrals	C-N Dissociation Energy (eV)
<i>o</i> -[NP-H] <sup>-</sup>	3.46	<i>o</i> -NP	2.72
<i>m</i> -[NP-H] <sup>-</sup>	3.42	<i>m</i> -NP	2.87
<i>p</i> -[NP-H] <sup>-</sup>	3.85	<i>p</i> -NP	3.00
NB <sup>•-</sup>	1.87	NB	2.89
<i>o</i> -NT <sup>•-</sup>	1.68	<i>o</i> -NT	2.79
<i>m</i> -NT <sup>•-</sup>	1.84	<i>m</i> -NT	2.90
<i>p</i> -NT <sup>•-</sup>	1.85	<i>p</i> -NT	2.94

A different explanation involves using the potential energy diagram in Figure 6.7, which shows the relationship between C-N bond energies ( $D_0$ ) and electron affinities of the nitroaromatics ( $X\text{-NO}_2$ ) ( $X$  = substituted nitroaromatic). The  $D_0$  values have not been experimentally determined for the neutral nitrophenoxyl radicals. However, using the negative ion thermochemical cycle the difference in the bond energy can be determined from the difference in EA of  $\text{NO}_2^\bullet$  and the corresponding nitroaromatic compound. This is summarized in Eq. (6.2)

$$\Delta D_0 = D_0(X - \text{NO}_2) - D_0(X - \text{NO}_2^-) = EA(\text{NO}_2) - EA(X - \text{NO}_2) \quad (6.2)$$

where  $\Delta D_0$  is the difference in bond energy,  $D_0(X - \text{NO}_2)$  is the bond dissociation energy of the neutral compound,  $D_0(X - \text{NO}_2^-)$  is the bond dissociation energy of the anion,  $EA(\text{NO}_2)$  is the electron affinity of  $\text{NO}_2^\bullet$ , and  $EA(X)$  is the electron affinity of the corresponding nitroaromatic. This relationship shows the change in the C-N bond energy can be related to the difference of the two electron affinities. These values are included in Table 6.2. Examination of Eq. (6.2) reveals if the electron affinity of the aromatic ion is lower than the electron affinity of  $\text{NO}_2^\bullet$ , the  $D_0$  of the anion will be lower than the corresponding neutral. If the aromatic fragment has a higher electron affinity than the  $\text{NO}_2^\bullet$  fragment, the anion will have a larger  $D_0$  than the neutral. Examination of Table 6.2 shows the nitrophenoxides have significantly larger electron affinities compared to  $\text{NO}_2^\bullet$ , whereas the nitrotoluenes have lower electron affinities. According to Eq. (6.2), the C-N bond dissociation energies for the nitrophenoxides are expected to be larger than the  $D_0$  values of the corresponding neutral nitrophenoxyl radicals. It is important to note these radical species do not have an H atom at the alcohol position, therefore these are not the same as the nitrophenols reported in Table 6.1. For the nitrotoluenes, the electron affinities of the

nitrotoluenes are lower than the  $\text{NO}_2^\bullet$ . This implies the C-N bond dissociation energy of the anion is lower than the neutral nitrotoluene compounds. This is in agreement with experiment and theory. The large electron affinity of nitrophenoxide is responsible for the increased C-N bond energy. The anion stability is a result of the additional electronegative oxygen atom and charge delocalization in a non-bonding  $\pi$  orbital. This can be seen in Figure 6.6. As a result of the increased C-N bond strength, the lowest energy decomposition pathway for the nitrophenoxides is rearrangement and loss of  $\text{NO}^\bullet$ .

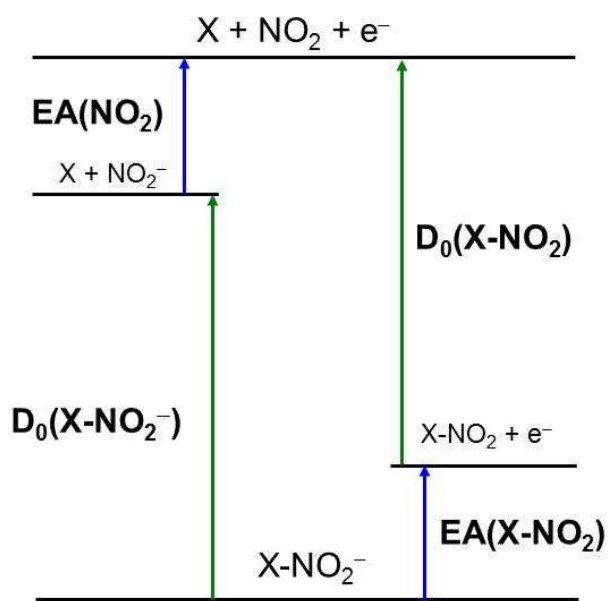


Figure 6.7: Potential energy diagram illustrating the relationship between C-N bond dissociation energies ( $D_0$ ) and electron affinities (EA) of a nitroaromatic ( $X - \text{NO}_2$ ) and its corresponding anion ( $X - \text{NO}_2^-$ ).

Table 6.2: Electron affinities of nitrotoluenes (NT), nitrophenoxyl radicals (NP-H), and NO<sub>2</sub>.

Species	Electron Affinity (eV)	Reference
<i>o</i> -NT	0.92 ± 0.10	90
<i>m</i> -NT	0.95 ± 0.10	90
<i>p</i> -NT	0.99 ± 0.10	90
<i>o</i> -[NP-H]	unknown	
<i>m</i> -[NP-H]	3.15 ± 0.12	121
<i>p</i> -[NP-H]	3.49 ± 0.12	121
NO <sub>2</sub>	2.273 ± 0.005	92

## 6.4 Conclusions

CID and ERMS studies were conducted on the deprotonated nitrophenol anions. Three common fragments (C<sub>6</sub>H<sub>4</sub>O<sup>•-</sup>, NO<sub>2</sub><sup>-</sup>, and C<sub>6</sub>H<sub>4</sub>O<sub>2</sub><sup>•-</sup>) were observed in the CID spectra of the *ortho*-, *meta*-, and *para*- isomers of nitrophenoxide. The *ortho*- and *meta*- isomers also showed another common fragment, C<sub>5</sub>H<sub>4</sub>O<sup>•-</sup>. The ERMS spectra showed the lowest energy fragment for each isomer was C<sub>6</sub>H<sub>4</sub>O<sub>2</sub><sup>•-</sup> with an appearance energy between 2.5 eV and 3 eV. Good agreement was found between the theoretical calculations of the nitro-to-nitrite isomerization barrier and the measured appearance energies. The appearance energy for C<sub>6</sub>H<sub>4</sub>O<sup>•-</sup> was between 3 eV and 4 eV for all isomers. For the *ortho*- and *meta*- isomers, NO<sub>2</sub><sup>-</sup> and C<sub>5</sub>H<sub>4</sub>O<sup>•-</sup> appeared between 3 eV and 3.5 eV. These fragments appeared around 4 eV for *p*-nitrophenoxide. Theory agrees well with the experimental dissociation energies. In conclusion, C-N bond dissociation energies of nitrophenoxide anions were compared to the corresponding neutral compounds, nitrotoluene radical anions, and nitrotoluene neutrals. Stabilization of the deprotonated anion results in an increase in the C-N bond energy for the nitrophenoxide anions.

## CHAPTER 7

### THE DECOMPOSITION OF COPPER NITRATE CLUSTER ANIONS

#### 7.1 Introduction

Electrospray ionization (ESI) can be used to synthesize inorganic species, such as metal-nitrate anion clusters, in the gas phase.<sup>122-125</sup> Anion clusters are formed by the electrostatic attraction between the positively charged metal center and an extra polyatomic anion ligand. Transfer of an electron or atomic ion from the ligand to the metal is known to occur in these anion clusters.<sup>122,123,125,126</sup> This makes metal-nitrate anion clusters interesting model systems to study oxidation and reduction reactions.<sup>127</sup> The first gas phase study on metal nitrate anion fragmentation was completed by Li *et al.* using a tandem quadrupole mass spectrometer.<sup>123</sup> Frański *et al.* reinvestigated these initial experiments using a quadrupole-TOF mass spectrometer for collision induced dissociation.<sup>122</sup> According to both studies, the primary decomposition pathways for many transition metal nitrate cluster anions were the loss of  $\text{NO}_3^-$ ,  $\text{NO}_3^\bullet$ , and  $\text{NO}_2^\bullet$ . The charge of the metal affected the specific types of reactions observed in the clusters. While the results were similar, different explanations were proposed for the variation in reactivity. Both groups attributed loss of  $\text{NO}_3^\bullet$  to the reduction of the metal charge *via* electron transfer. Li *et al.* proposed  $\text{O}^-$  atom abstraction resulted in the loss of  $\text{NO}_2^\bullet$  leaving the oxidation state of the metal and oxygen anion unaffected by the formation of the metal oxide fragment.<sup>123</sup> Li argued the low collision energies used in the experiments were not sufficiently energetic to oxidize metal cations

due to the reported high ionization energies (2<sup>nd</sup>, 3<sup>rd</sup>, 4<sup>th</sup>, etc.). Frański suggested oxidation of the metal does occur upon O<sup>-</sup> abstraction based on the observations of secondary fragments with formulas that agree with well-known metal oxides in high oxidation states, such as MnO<sub>4</sub><sup>-</sup>, FeO<sub>3</sub><sup>-</sup>, and CuO<sub>2</sub><sup>-</sup>.<sup>122</sup> Recently, the UV photodissociation spectrum of Cu(NO<sub>3</sub>)<sub>3</sub><sup>-</sup> was reported by Kaufman.<sup>125</sup> Results showed the formation of Cu(NO<sub>3</sub>)<sub>2</sub><sup>-</sup> and loss of NO<sub>3</sub><sup>•</sup> resulting from electron transfer from a nitrate ligand to the metal center. Loss of NO<sub>3</sub><sup>-</sup> was not reported in the photofragmentation study.

Our work reports on the decomposition of copper nitrate anion clusters using a triple quadrupole mass spectrometer. The 3*d* subshell of copper is completely filled or nearly filled depending on the oxidation state of the metal. This simplifies the electronic structure of the metal in comparison to many other transition metal ions, thusly making copper an appealing system to investigate the fundamental processes involved in the previously reported fragmentation pathways.

## 7.2 Methods

Copper (II) nitrate was purchased and used without further purification from VWR Scientific. Solutions were made with a concentrations ranging from 0.1 mM to 1.0 mM using HPLC grade methanol (25% vol.) and deionized water (75% vol.). The deionized water had a resistance of 18.2 MΩ. A syringe pump was used to introduce solution into the ESI source at a flow rate of 10 μL/min.

The experiments in this chapter were carried out using the mass spectrometer described in Chapter 2. Nitrogen at 60 psi was used as the nebulizing gas. The ESI source voltage was maintained at -4 kV with a current of 1 μA. The ions generated in the ESI source passed through

the heated capillary, held at 200°C, before entering the medium vacuum chamber. A skimmer and electrostatic lenses focused the ions into a collimated beam before the ions entered the high vacuum chamber. CID and ERMS experiments were carried out in accordance with the procedures outlined in Chapter 2. Due to large experimental uncertainties, the ERMS studies are not intended to measure accurate bond energies in this work. However, the energetic information obtained from these studies is useful because relative differences in the appearance energies are frequently related to relative differences and provide insight into fragmentation dynamics.<sup>122,123</sup>

The theoretical calculations in this work were carried out using the Gaussian 09 suite of programs.<sup>75,76</sup> Density Functional Theory (DFT) with the B3LYP exchange-correlation functional<sup>77,78</sup> with the 6-311+G(3df)<sup>75</sup> basis set was used for structure optimization calculations. The unrestricted wave function was used in open-shell species. No imaginary frequencies were found in the vibrational frequency calculations of each structure. This ensured each optimized structure corresponds to a local minimum. The natural population analysis (NPA) method was used to calculate charges and electron configurations.<sup>128</sup>

## 7.3 Results

### 7.3.1 *Mass Spectra*

A representative ESI mass spectrum of the copper nitrate solution is shown in Figure 7.1. The major peaks are  $\text{NO}_3^-$ ,  $\text{H}(\text{NO}_3)_2^-$ ,  $\text{Cu}(\text{NO}_3)_2^-$ , and  $\text{Cu}(\text{NO}_3)_3^-$ . The most intense peak is  $\text{Cu}(\text{NO}_3)_3^-$ . The isotope pattern of a species containing a single copper atom is shown in the inset in the upper-left corner of Figure 7.1. Charge reduction of the copper atom during generation of the gas phase ion complexes occurs to form the second most intense product,  $\text{Cu}(\text{NO}_3)_2^-$ . Oxidation and reduction reactions have been reported in electrospray ionization.<sup>129-136</sup>

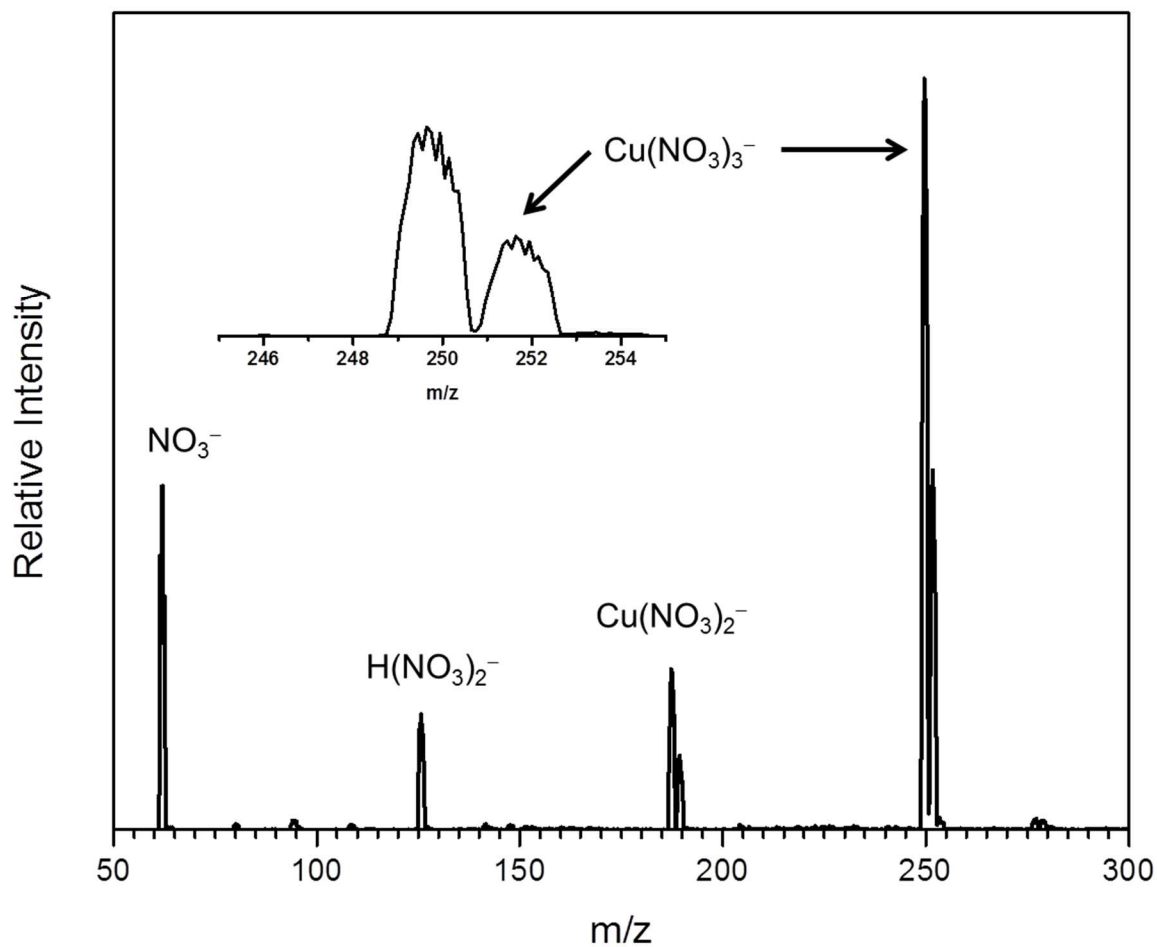


Figure 7.1 Mass spectrum of 0.1 mM copper (II) nitrate solution in 25/75 (%v/v) methanol/water solvent. The upper left inset shows the isotopic pattern for  $\text{Cu}(\text{NO}_3)_3^-$ .

### 7.3.2 Collision Induced Dissociation

The CID spectra of  $\text{Cu}(\text{NO}_3)_2^-$  and  $\text{Cu}(\text{NO}_3)_3^-$  are shown in Figure 7.2. The  $^{63}\text{Cu}$  isotope was used to record the CID spectra because of its greater relative abundance. CID spectra from  $^{65}\text{Cu}$  were also collected and are analogous to the spectra shown here. Examination of Figure 7.2 shows similar results to those reported by Li and Frański.<sup>122,123</sup> A typical CID mass spectrum for  $\text{Cu}(\text{NO}_3)_3^-$  is shown in Figure 7.2(a). The major products correspond to  $\text{NO}_3^-$  and  $\text{Cu}(\text{NO}_3)_2^-$ . The loss of  $\text{NO}_3^-$  produces a neutral copper (II) nitrate cluster. The metal is reduced to copper (I) upon the loss of  $\text{NO}_3^\bullet$  to form  $\text{Cu}(\text{NO}_3)_2^-$ . A weak peak, corresponding to  $\text{CuO}(\text{NO}_3)^-$ , forms from  $\text{Cu}(\text{NO}_3)_2^-$ .

The CID spectrum of  $\text{Cu}(\text{NO}_3)_2^-$  is shown in Figure 7.2(b). The major products observed are  $\text{NO}_3^-$  and  $\text{CuO}(\text{NO}_3)^-$ . The loss of  $\text{NO}_3^-$  results in a neutral copper (I) nitrate cluster. Formation of  $\text{CuO}(\text{NO}_3)^-$  from  $\text{Cu}(\text{NO}_3)_2^-$  confirms this species is a secondary fragment in Figure 7.2(a). Intracluster dissociation of a NO bond in a nitrate ligand results in the formation of a Cu-O bond and loss of  $\text{NO}_2^\bullet$ .  $\text{CuO}(\text{NO}_3)^-$  is formed as a fragment from this process. A second  $\text{O}^-$  abstractions from the intact nitrate ligand on  $\text{CuO}(\text{NO}_3)^-$  produces the low intensity fragment,  $\text{CuO}_2^-$ .

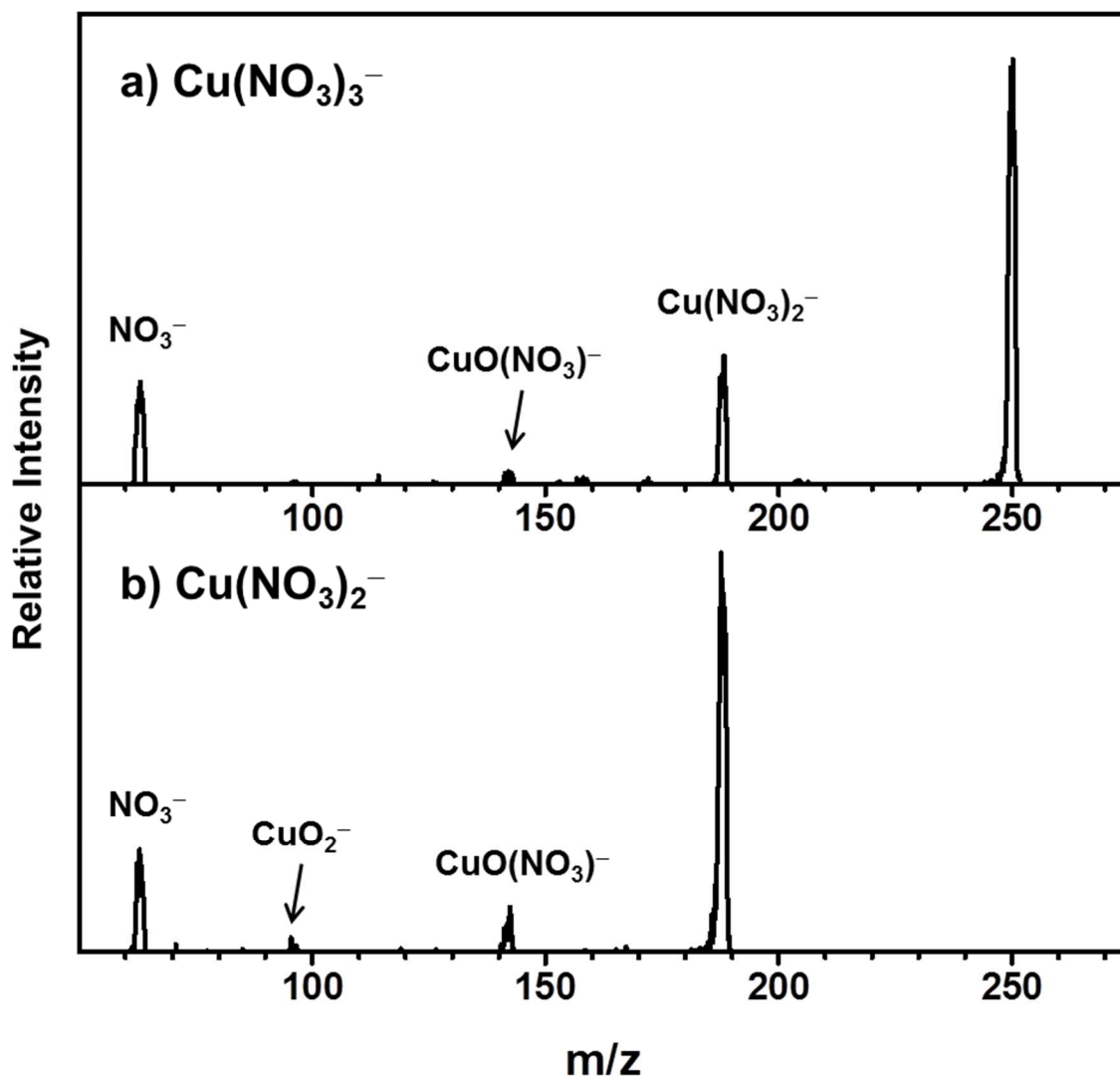


Figure 7.2: Collision induced dissociation mass spectra of (a)  $\text{Cu}(\text{NO}_3)_3^-$  and (b)  $\text{Cu}(\text{NO}_3)_2^-$  at  $30 \text{ eV}_{\text{lab}}$  collision energy with  $0.50 \text{ mTorr}$  Ar collision gas.

### 7.3.3 Energy Resolved Mass Spectrometry

The energy dependent fragmentation of  $\text{Cu}(\text{NO}_3)_3^-$  is shown in Figure 7.3(a). At low collision energies, the most intense fragment is  $\text{NO}_3^-$ , with an appearance energy of 1.2 – 1.3 eV. It is difficult to assign an exact appearance energy due the broad onset of the signal.  $\text{Cu}(\text{NO}_3)_2^-$  has a slightly higher appearance energy at 1.5 – 1.7 eV. At approximately 4.5 eV  $\text{Cu}(\text{NO}_3)_2^-$  becomes the most intense product.  $\text{CuO}(\text{NO}_3)^-$  has the highest appearance energy at 3.5 – 4 eV. The intensity of  $\text{CuO}(\text{NO}_3)^-$  remains low at all collision energies because it is a secondary fragment.

The energy dependent fragmentation of  $\text{Cu}(\text{NO}_3)_2^-$  is shown in Figure 7.3(b). At all collision energies  $\text{NO}_3^-$  is the most intense fragment. The appearance energy of  $\text{NO}_3^-$  is 1.4 – 1.6 eV.  $\text{CuO}(\text{NO}_3)^-$  has a similar appearance energy of about 1.4 – 1.6 eV, but remains less intense than  $\text{NO}_3^-$ . The relative intensity of  $\text{CuO}(\text{NO}_3)^-$  is about half the intensity of  $\text{NO}_3^-$  at higher collision energies. Energy dependent fragmentation spectra of  $\text{CuO}_2^-$  was not measured due to the low intensity of the fragment at the reduced pressure of the collision gas in this portion of the experiment.

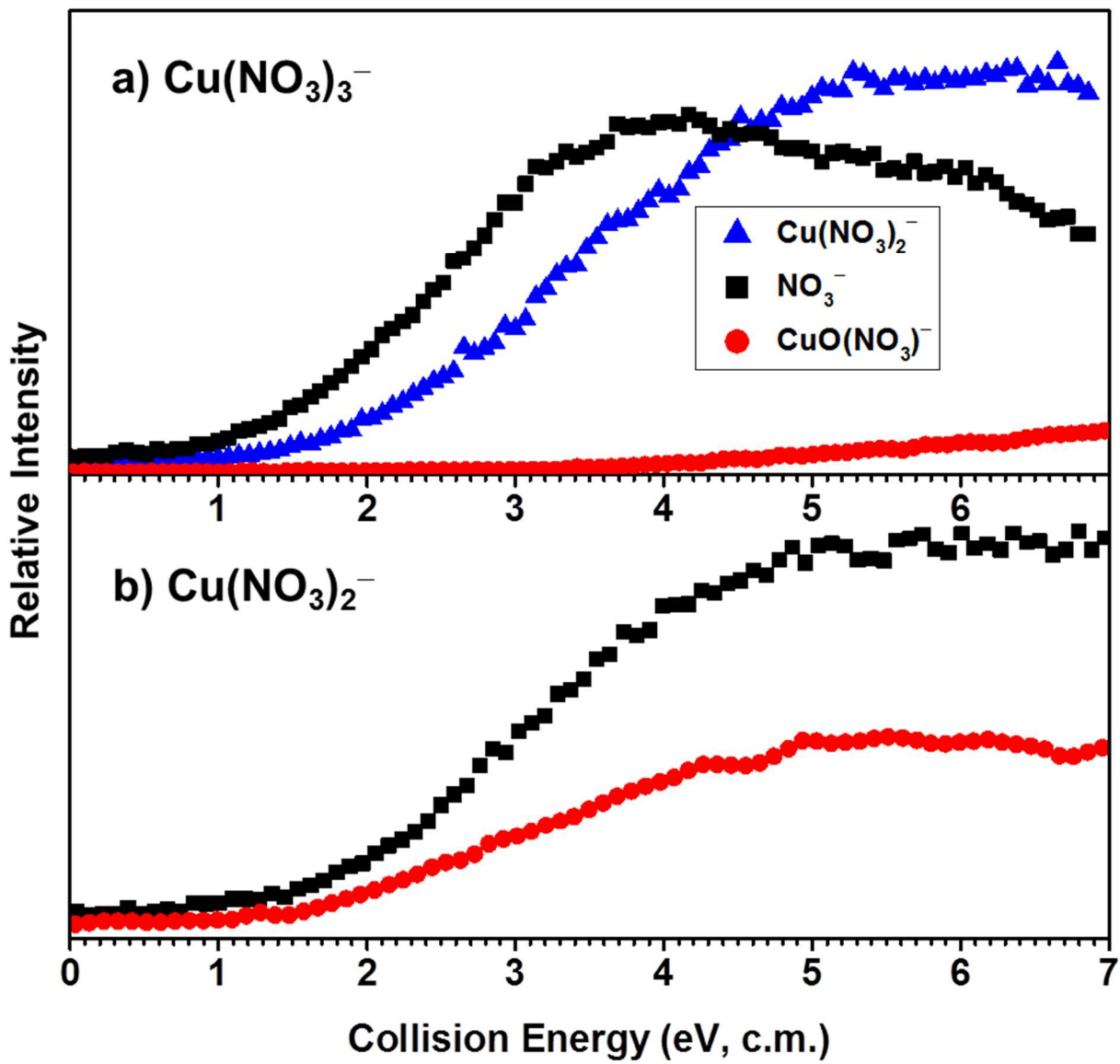
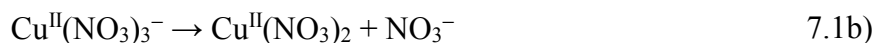
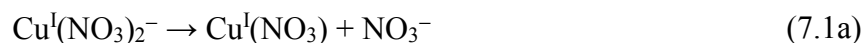


Figure 7.3: Energy resolved mass spectra for the fragmentation of (a)  $\text{Cu}(\text{NO}_3)_2^-$  and (b)  $\text{Cu}(\text{NO}_3)_3^-$ .

## 7.4 Discussion

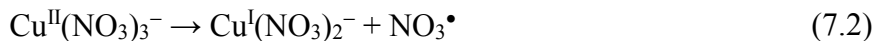
### 7.4.1 Cluster Fragmentation

Several interesting processes were observed in the fragmentation of  $\text{Cu}(\text{NO}_3)_3^-$  and  $\text{Cu}(\text{NO}_3)_2^-$ . The first process is the loss of  $\text{NO}_3^-$ . Equation (7.1) relates the binding affinity of a nitrate anion to the neutral salt.



The Roman numerals indicate the formal oxidation state of the metal. The appearance energy of  $\text{NO}_3^-$  is approximately 1.3 eV for  $\text{Cu}^{\text{II}}(\text{NO}_3)_3^-$  and 1.4 – 1.6 eV for  $\text{Cu}^{\text{I}}(\text{NO}_3)_2^-$ . The similarity of these two binding energies suggest the increased electrostatic attraction of  $\text{NO}_3^-$  to the copper (II) in  $\text{Cu}^{\text{II}}(\text{NO}_3)_3^-$ , compared to copper (I) in  $\text{Cu}^{\text{I}}(\text{NO}_3)_2^-$ , is offset by the additional repulsive forces from the extra nitrate ligand.

The second process observed is the loss of  $\text{NO}_3^\bullet$ . This process is the result of electron transfer from a nitrate group to the copper atom, which only occurs in the dissociation of  $\text{Cu}^{\text{II}}(\text{NO}_3)_3^-$ . Equation (7.2) describes the dissociation process.



The electrostatic force of the positive charge on the copper atom induces the electron transfer.

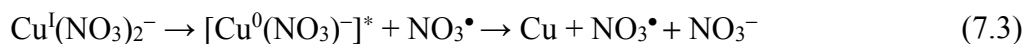
Previous work determined the electron detachment energy of  $\text{NO}_3^-$  to be  $3.937 \pm 0.0014$  eV.<sup>137</sup>

Our work shows nitrate anions in copper clusters have an electron detachment energy around 1.5 – 1.6 eV. The ERMS spectrum in Figure 7.3a shows a competition between the  $\text{NO}_3$  and

$\text{Cu}(\text{NO}_3)_2$  fragment for the excess electron. At low collision energies  $\text{NO}_3^-$  is the dominant fragment; however, at higher collision energies  $\text{Cu}(\text{NO}_3)_2^-$  is the dominant fragment.

This suggests the higher collision energies are capable of overcoming the large electron binding energy of  $\text{NO}_3^-$ , leading to an increased rate of electron transfer to form  $\text{Cu}^{\text{I}}(\text{NO}_3)_2^-$ .

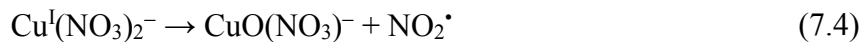
The electron transfer observed in  $\text{Cu}^{\text{II}}(\text{NO}_3)_3^-$  results in the formation of the reduced cluster  $\text{Cu}^{\text{I}}(\text{NO}_3)_2^-$ . The strong electrostatic attraction between the metal cation and the remaining  $\text{NO}_3^-$  ligands bind the cluster together through ionic bonds. A second electron transfer reaction would result in the reduction of the copper metal and loss of  $\text{NO}_3^\bullet$ . Fragmentation of  $\text{Cu}^{\text{I}}(\text{NO}_3)_2^-$  did not show the loss of  $\text{NO}_3^\bullet$ . The reduction of  $\text{Cu}^{\text{I}}(\text{NO}_3)_2^-$  is most likely indistinguishable from the loss of  $\text{NO}_3^-$  due to the weak binding energy in  $\text{Cu}^0(\text{NO}_3)^-$ . Equation (7.3) describes the fast, secondary dissociation of this cluster to produce  $\text{NO}_3^-$ .



Another explanation for why the loss of  $\text{NO}_3^\bullet$  is only observed for  $\text{Cu}^{\text{II}}(\text{NO}_3)_3^-$  is the metal ion electronic structure. In  $\text{Cu}^{\text{I}}(\text{NO}_3)_2^-$  the metal ion has a  $3d^{10}$  electron configuration. Electron transfer would result in the extra electron being placed in the higher energy  $4s$  orbital. The energy associated with occupation of the  $4s$  orbital makes this process less competitive with other fragmentation processes. In comparison,  $\text{Cu}^{\text{II}}(\text{NO}_3)_3^-$  has a  $3d^9$  electron configuration. This configuration allows for an additional electron to be readily accepted to complete the subshell.

The most interesting process observed in the decomposition of the copper nitrate cluster anions is the loss of  $\text{NO}_2^\bullet$ . Figure 7.2 shows sequential loss of  $\text{NO}_2^\bullet$  was observed in the dissociation of  $\text{Cu}^{\text{I}}(\text{NO}_3)_2^-$ , but was not observed in the dissociation of  $\text{Cu}^{\text{II}}(\text{NO}_3)_3^-$ . This process

requires the transfer of an O<sup>-</sup> atom from a nitrate ligand and the formation of a Cu–O bond, described in Eq. (7.4).



The loss of NO<sub>2</sub><sup>•</sup> requires a covalent NO bond to break. The bond energy required to break the O<sub>2</sub>N–O<sup>-</sup> bond is calculated to be 4.69 eV.<sup>121</sup> From our work, the appearance energy for the O<sup>-</sup> transfer is about 1.4 – 1.6 eV. The difference between the calculated bond energy and the measured appearance energy suggests the copper ion helps to facilitate the decomposition of the covalent NO<sub>3</sub><sup>-</sup> compound. Since this process was only observed in the Cu<sup>I</sup>(NO<sub>3</sub>)<sub>2</sub><sup>-</sup> clusters, it is likely fragmentation is controlled by the oxidation state of the copper atom.

Frański recently argued metals with high charge density are more likely to undergo charged particle transfer<sup>122</sup>; however, our work on copper nitrate anion clusters challenges this argument. Cu<sup>II</sup>(NO<sub>3</sub>)<sub>3</sub><sup>-</sup> does not undergo O<sup>-</sup> abstraction, whereas Cu<sup>I</sup>(NO<sub>3</sub>)<sub>2</sub><sup>-</sup> does. Our work shows the probability for O<sup>-</sup> abstraction depends on the charge density of the metal as well as the electronic structure of the metal ion. Cu<sup>I</sup> containing clusters are more likely to undergo O<sup>-</sup> abstraction due to the ability of the unoccupied 4*s* orbital to readily accept a pair of electrons from oxygen, which results in a strong ionic bond. Cu<sup>II</sup> containing clusters are more likely to undergo reduction to fill the lower energy 3*d* subshell.

O<sup>-</sup> abstraction was also observed from the fragmentation of CuO(NO<sub>3</sub>)<sup>-</sup>. The reactions in Eq. (7.2) and Eq. (7.4) suggests O<sup>-</sup> abstraction only occurs if copper is in the +1 oxidation state. The secondary O<sup>-</sup> abstraction from CuO(NO<sub>3</sub>)<sup>-</sup> is consistent with this observation. The loss of NO<sub>3</sub><sup>•</sup>, as a result of electron transfer, would be observed if Cu was in the 2+ oxidation state. However, the corresponding CuO<sup>-</sup> fragment does not appear in Figure 7.2b. The lack of CuO<sup>-</sup>

signal could be due to the low electron binding energy of the fragment,  $1.7810 \pm 0.0014$  eV, which is limited by competitive loss of  $\text{NO}_3^-$ .<sup>138</sup>

An alternative explanation focuses on the formation of the CuO core from  $\text{Cu}^+$  and  $\text{O}^-$  within the  $\text{CuO}(\text{NO}_3)^-$  anion. Figure 7.4 shows a qualitative molecular orbital diagram for CuO. High-level theoretical studies have shown an accurate description of the Cu-O bond is theoretically challenging.<sup>139-143</sup> The relative atomic orbital energies are based on calculations of the isolated atoms. The core orbitals have been omitted in the orbital numbering scheme. The qualitative orbital diagram makes the assumption the relative energies of the copper  $3d$  orbitals are well below the  $4s$  orbital due to increased nuclear charge.<sup>144</sup> Bond formation occurs through interaction between the unoccupied copper  $4s$  orbital with a lone pair of electrons from the  $2p_z$  oxygen orbital. This is in good agreement with studies which predict CuO has considerable  $\text{Cu}^+(3d^{10})\text{O}^-(2p^5)$  character in its electronic ground state.<sup>140,141,145-147</sup> Figure 7.4 does not agree with the oxidation state previously assigned for  $\text{CuO}(\text{NO}_3)^-$ .<sup>122</sup> The electron configuration of  $\text{CuO}(\text{NO}_3)^-$  assumed a copper  $3d^{10}$  electron was transferred to an oxygen atom, resulting in a  $\text{Cu}^{2+}(3d^9)\text{O}^{2-}(2p^6)$  electron configuration. This electron configuration would only be possible if the energies of the copper  $3d$  orbitals were above the oxygen orbitals. To better understand the fragmentation reactions and electronic structure of copper nitrate cluster anions, a more advanced theoretical analysis, beyond the scope of this work, is required.

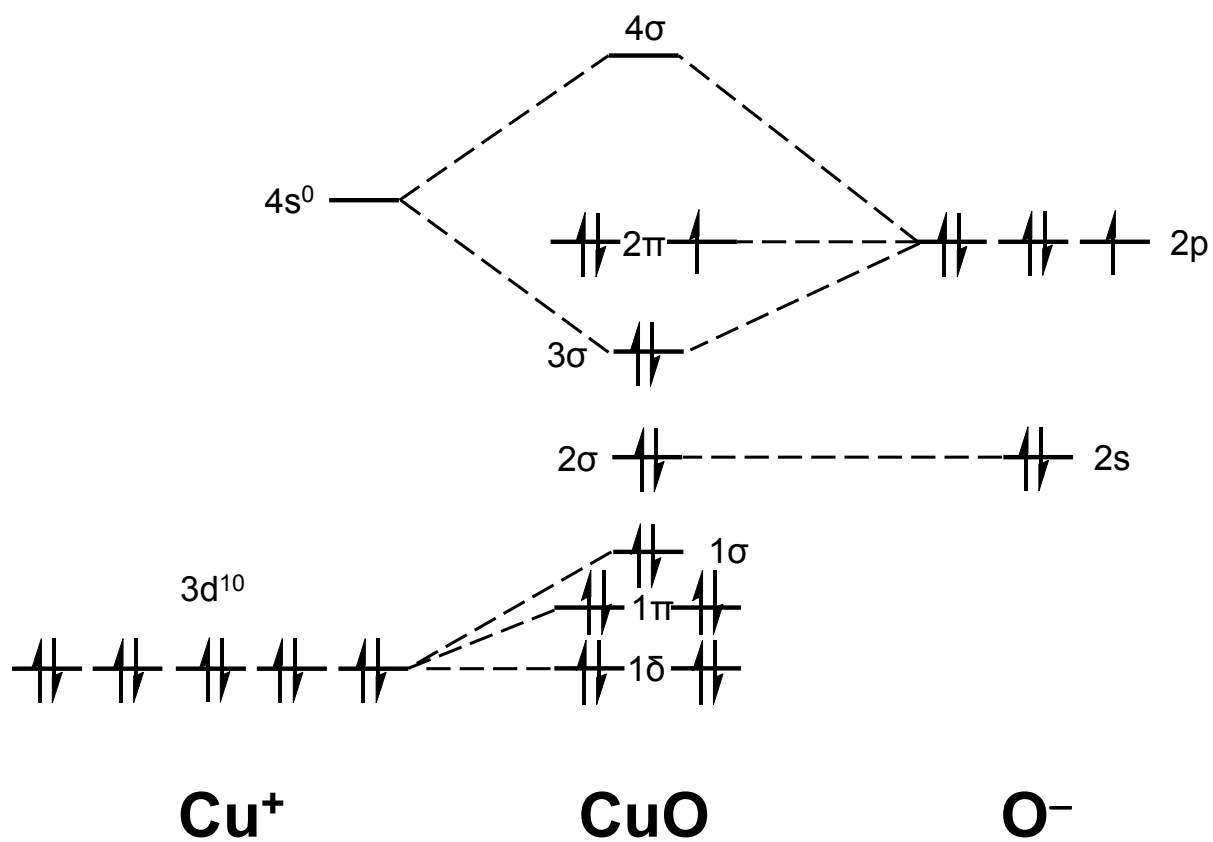


Figure 7.4: Hypothetical molecular orbital diagram for the formation of  $\text{CuO}$  from  $\text{Cu}^+$  and  $\text{O}^-$ . The relative orbital energies suggest the copper atom is not oxidized upon bond formation with oxygen and the unpaired electron remains on the oxygen atom.

### 7.4.2 Optimized Structures

Optimized structures for  $\text{Cu}(\text{NO}_3)_3^-$ ,  $\text{Cu}(\text{NO}_3)_2^-$ ,  $\text{CuO}(\text{NO}_3)^-$ , and  $\text{CuO}_2^-$  at the B3LYP/6-311+G(3df) level of theory are shown in Figure 7.5. The Roman numerals indicating the hypothetical oxidation state of copper have been dropped for the remainder of the discussion. In order to maximize the electrostatic forces between the electronegative oxygen and the positive metal center, each nitrate group in  $\text{Cu}(\text{NO}_3)_3^-$  binds through a bidentate fashion with two oxygen atoms pointing towards the metal ion. The three equivalent nitrate groups adopt a roughly trigonal planar arrangement due to the mutual repulsion of the ligands. The average Cu-O distance of 2.17 Å with each nitrate group partially rotated out of plane.

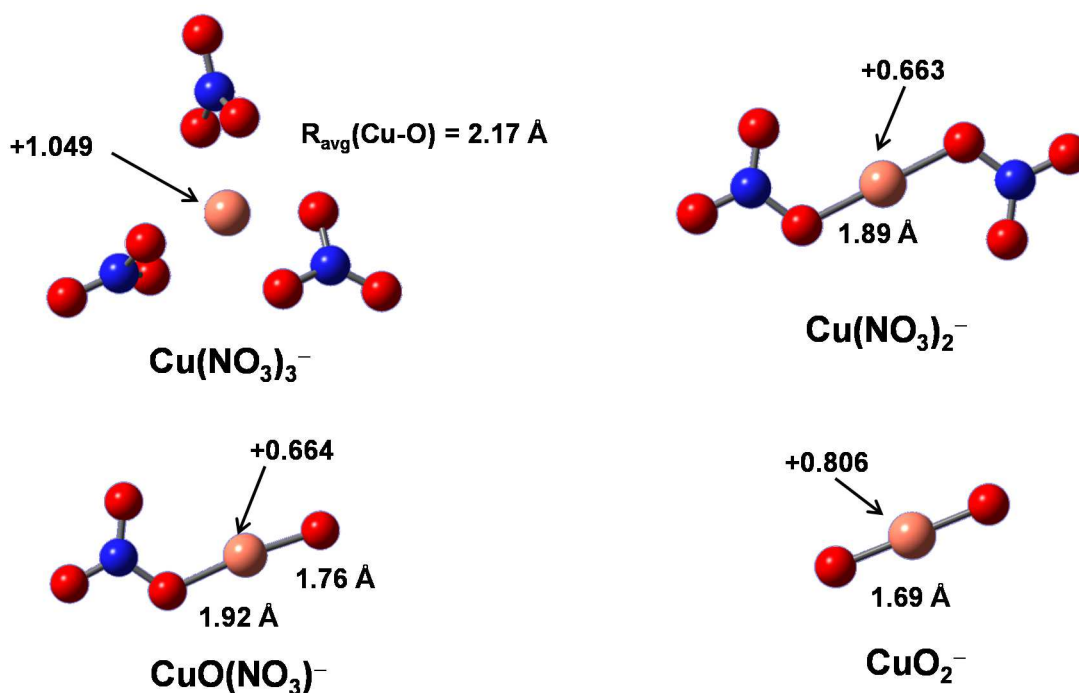


Figure 7.5: Optimized copper anion cluster structures calculated at the B3LYP/6-311+G(3df) level of theory. Atomic charges were calculated for each cluster using the natural population analysis method.

$\text{Cu}(\text{NO}_3)_2^-$  adopts a quasi-linear (actually  $C_{2h}$ ) structure. The nitrate groups are on opposite sides of the metal in order to minimize the ligand-ligand repulsive forces. Both ligands are in the plane of the molecule, with a single oxygen atom from each nitrate group interacting strongly with the copper ion. The Cu–O distance is 1.89 Å. The calculated structure for  $\text{CuO}(\text{NO}_3)^-$  is similar to the structure for  $\text{Cu}(\text{NO}_3)_2$  with a  $\text{NO}_2$  group removed. The Cu–O bond distance, 1.92 Å, is essentially unchanged for the remaining nitrate group. However, the bond distance of the lone Cu–O bond is shortened to 1.76 Å.  $\text{CuO}_2^-$  has a linear structure, with a Cu–O bond distances of 1.69 Å. The optimized structures reported in this work are in good agreement with those reported for  $\text{Cu}(\text{NO}_3)_3^-$  and  $\text{Cu}(\text{NO}_3)_2^-$  at the PBE0/def2-TVZP level of theory.<sup>125</sup>

Figure 7.6 shows the corresponding neutral structures for  $\text{Cu}(\text{NO}_3)_2$ ,  $\text{Cu}(\text{NO}_3)$  and  $\text{CuO}$ . The clusters are highly symmetric and planar. The neutral clusters have bidentate bonding in the ligand groups with equivalent Cu–O bond distances.  $\text{Cu}(\text{NO}_3)_2$  has Cu–O bond distances of 1.97 Å, whereas  $\text{Cu}(\text{NO}_3)$  has Cu–O bond distances of 2.06 Å. The difference in the relative bond distances reflects the role of the copper oxidation state on the ionic bond strength. The addition of a nitrate group to  $\text{Cu}(\text{NO}_3)_2$  to form  $\text{Cu}(\text{NO}_3)_3^-$  results in an increase in electrostatic repulsion. This results in longer Cu–O bond distances. A change in ligand binding from bidentate to monodentate occurs as a result of the addition of a nitrate group to  $\text{Cu}(\text{NO}_3)$  to form  $\text{Cu}(\text{NO}_3)_2^-$ . The monodentate bond is made by strongly bound oxygen atoms in  $\text{Cu}(\text{NO}_3)_2^-$ . These stronger bonds result in the shorter Cu–O bond distances in  $\text{Cu}(\text{NO}_3)_2^-$  compared to  $\text{Cu}(\text{NO}_3)$ .

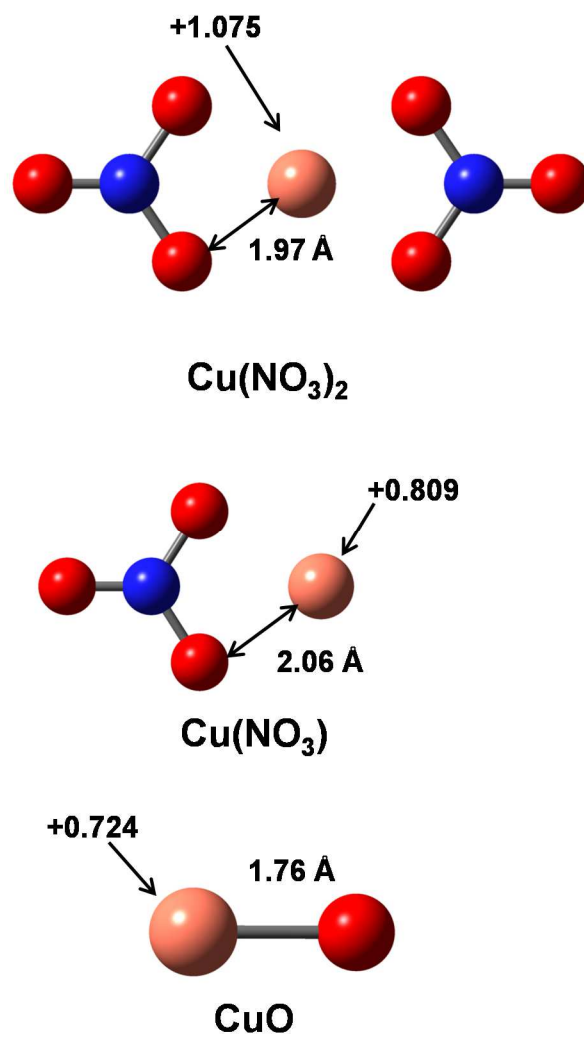


Figure 7.6: Optimized neutral copper cluster structures calculated at the B3LYP/6-311+G(3df) level of theory. Atomic charges were calculated using the natural population analysis method.

### 7.4.3 Energetics

Table 7.1 contains the calculated dissociation energies (electronic and zero point energy differences) of the copper nitrate cluster anions. The loss of  $\text{NO}_3^-$  from  $\text{Cu}(\text{NO}_3)_3^-$  has a calculated energy of 1.90 eV, whereas the loss of  $\text{NO}_3^\bullet$  is calculated to require 2.10 eV. For  $\text{Cu}(\text{NO}_3)_2^-$ , the loss of  $\text{NO}_3^-$  is calculated to be 2.67 eV. The loss of  $\text{NO}_2^\bullet$  is calculated to be 2.69 eV. These energies are in good agreement with the order of the experimental appearance energies in Figure 7.3. However, the theoretical energies are larger than the reported experimental values. It is important to note the *relative* differences are in reasonable agreement with experiment. For example, the appearance energies for the loss of  $\text{NO}_3^-$  and  $\text{NO}_2^\bullet$  from  $\text{Cu}(\text{NO}_3)_2^-$  are nearly identical. The difference in the calculated energies is only 0.02 eV. Various sources of error could contribute to the disagreement between the experimental and theoretical values. The theoretical energy differences reported in Table 7.1 do not account for transition state geometries or possible energy barriers to dissociation. The calculated energy differences do not account for relativistic and spin-orbit effects. Additionally, the open-shell species are expected to have multi-reference character.<sup>148,149</sup> The single determinant methods used in this work can only be expected to provide qualitative energetic information. Experimental sources of error also contribute to the disagreement. The internal energy distribution is unknown for the ions generated in the source. Lowered appearance energies relative to theoretical dissociation energies can occur from additional internal energy carried by the precursor ion. Other possible sources of error have been previously discussed.

The appearance energy  $\text{CuO}(\text{NO}_3)^- \rightarrow \text{CuO}_2^- + \text{NO}_2^\bullet$  was not measured. However, calculations predict this reaction requires 3.58 eV. This reaction energy is consistent with the low relative intensity observed for this secondary product in Figure 3.3b.

Table 7.1: Calculated energy differences (including zero point energy corrections) for dissociation reactions of copper nitrate anions at the B3LYP/6-311+G(3df) level of theory.

Reaction	Energy (eV)
$\text{Cu}(\text{NO}_3)_3^- \rightarrow \text{Cu}(\text{NO}_3)_2 + \text{NO}_3^-$	1.90
$\text{Cu}(\text{NO}_3)_3^- \rightarrow \text{Cu}(\text{NO}_3)_2^- + \text{NO}_3^\bullet$	2.10
$\text{Cu}(\text{NO}_3)_2^- \rightarrow \text{Cu}(\text{NO}_3)_2 + \text{NO}_3^-$	2.67
$\text{Cu}(\text{NO}_3)_2^- \rightarrow \text{CuO}(\text{NO}_3)^- + \text{NO}_2^\bullet$	2.69
$\text{CuO}(\text{NO}_3)^- \rightarrow \text{CuO}_2^- + \text{NO}_2^\bullet$	3.58

Table 7.2: Calculated charges and electron configurations for copper atoms at the B3LYP/6-311+G(3df) level of theory using a natural population analysis.

Species	Charge on copper atom (e.s.u.)	Copper atom electron configuration	Change in number of 3d electrons <sup>1</sup>
$\text{Cu}(\text{NO}_3)_3^-$	+1.049	$[\text{Ar}] 4s^{0.31}3d^{9.30}4p^{0.33}$	0
$\text{Cu}(\text{NO}_3)_2^-$	+0.663	$[\text{Ar}] 4s^{0.45}3d^{9.78}4p^{0.10}$	+0.48
$\text{CuO}(\text{NO}_3)^-$	+0.664	$[\text{Ar}] 4s^{0.54}3d^{9.65}4p^{0.15}$	-0.14
$\text{CuO}_2^-$	+0.806	$[\text{Ar}] 4s^{0.56}3d^{9.33}4p^{0.30}$	-0.31
$\text{Cu}(\text{NO}_3)_2$	+1.075	$[\text{Ar}] 4s^{0.32}3d^{9.35}4p^{0.25}$	0
$\text{CuNO}_3$	+0.809	$[\text{Ar}] 4s^{0.17}3d^{9.94}4p^{0.08}$	+0.60
$\text{CuO}$	+0.724	$[\text{Ar}] 4s^{0.46}3d^{9.76}4p^{0.05}$	-0.18

<sup>1</sup> change is calculated relative to the number of electrons in the previously listed species in the table

#### 7.4.4 Metal Oxidation State

Of particular interest to this study is the oxidation state of the copper atoms, particularly in the  $\text{CuO}(\text{NO}_3)^-$  and  $\text{CuO}_2^-$  fragments.<sup>127</sup> To determine the relationship between calculated charges and oxidation state, theoretical atomic charges were used. The NPA method was used to calculate the charges on the atoms in each cluster. Similar trends were observed for the Mulliken charges. The NPA charge of each copper atom is listed in Figure 3.5. Calculated charges are all lower than the expected formal oxidation state for each copper atom. These charges are summarized in Table 7.2. The formal charge of copper in  $\text{Cu}(\text{NO}_3)_3^-$  is expected to be 2+. The calculated charge is +1.049. The copper atom is expected to have a +1 oxidation state in  $\text{Cu}(\text{NO}_3)_2^-$ , but the calculations predict a charge of +0.663. This shows the calculated charges are approximately one half the magnitude of the expected formal charges assigned to the ionic compounds. Electron density donated by the  $\text{NO}_3^-$  ligands can account for the differences between the formal and calculated charges. The calculated charges for neutral copper nitrate clusters are also included in Table 7.2. For  $\text{Cu}(\text{NO}_3)_2$  the calculated charge on the copper atom is +1.075. The calculated charge is +0.809 for  $\text{Cu}(\text{NO}_3)$ . The assigned oxidation state and calculated charges are similar in magnitude. The values act as guides for the oxidation state assignments in other clusters. The largest difference between the neutral and anion clusters is the charge for  $\text{Cu}(\text{NO}_3)$  versus  $\text{Cu}(\text{NO}_3)_2^-$ . Ligand bonding is responsible for the lower calculated charge on the copper atom in the anion cluster. More favorable electron donation to the metal is possible due to the shorter Cu-O bonds in  $\text{Cu}(\text{NO}_3)_2^-$ . This allows for a smaller net charge.

Examination of the copper atom charges in  $\text{Cu}(\text{NO}_3)_3^-$  and  $\text{Cu}(\text{NO}_3)_2^-$  shows the charge on the copper atom decreases. This is consistent with reduction following the loss of  $\text{NO}_3^\bullet$ . The calculated charges are nearly identical, +0.664, for the copper atom in  $\text{CuO}(\text{NO}_3)^-$  and

$\text{Cu}(\text{NO}_3)_2^-$ . This suggests copper is not oxidized in the reaction  $\text{Cu}(\text{NO}_3)_2^- \rightarrow \text{CuO}(\text{NO}_3)^- + \text{NO}_2^\bullet$ . This is in agreement with predictions based on Figure 7.4.  $\text{CuO}(\text{NO}_3)^-$  is expected to undergo oxidation upon a second  $\text{O}^-$  abstraction and loss of  $\text{NO}_2^\bullet$ . The calculations show an increase in the positive charge on the copper atom to +0.806, which is consistent with metal oxidation. In comparison to  $\text{Cu}(\text{NO}_3)_3^-$ , a similar copper (II) compound,  $\text{CuO}_2^-$ , has a smaller calculated charge for the copper atom. The difference in the calculated charges for these two species can be attributed to the electron density donated by oxygen atoms in  $\text{CuO}_2^-$  as a result of the significantly shorter Cu–O bond distances.

NPA calculations were also used to obtain the electron configuration of the copper atoms in  $\text{Cu}(\text{NO}_3)_3^-$ ,  $\text{Cu}(\text{NO}_3)_2^-$ ,  $\text{CuO}(\text{NO}_3)^-$ , and  $\text{CuO}_2^-$ . An inconsistent degree of electron donation from the ligands leads to some ambiguity in comparing the calculated charges to the expected oxidation states. Table 7.2 contains the calculated electron configurations. Nearly identical results were obtained for several clusters using various levels of theory and basis sets. Of particular interest to this work is the number of electrons occupying the  $3d$  subshell for each species. Electrons in the  $4s$  and  $4p$  valence orbitals are sensitive to electron density donated by the nitrate ligands or oxygen atoms during bond formation. Calculations predict a  $3d^{9.35}$  electron configuration for the  $3d$  subshell of copper in  $\text{Cu}(\text{NO}_3)_2$ . This is in good agreement with the hypothetical configuration of  $3d^9$ . In the formal charge limit,  $\text{Cu}(\text{NO}_3)_3^-$  is expected to have a  $3d^9$  electron configuration. Calculations predict a  $3d^{9.30}$  configuration.  $\text{Cu}(\text{NO}_3)$  and  $\text{Cu}(\text{NO}_3)_2^-$  have hypothetical  $3d^{10}$  electron configurations with a  $\text{Cu}^+$  cation. Calculations assign a  $3d^{9.94}$  and  $3d^{9.78}$  configuration, respectively, for each cluster. These calculations suggest the addition of a nitrate group to  $\text{CuNO}_3$  partially oxidizes the copper atom due to the short Cu–O bond in  $\text{Cu}(\text{NO}_3)^-$ . The

formal charge limit is similar to the expected configuration for both the anion and neutral clusters.

The electron configuration for  $\text{CuO}(\text{NO}_3)^-$  is calculated to be  $3d^{9.65}$ , 0.13 electrons less than  $\text{Cu}(\text{NO}_3)_2^-$ . This indicates the copper atom is not fully oxidized as a result of the first  $\text{O}^-$  abstraction. The electron configuration of  $\text{CuO}_2^-$ , produced from  $\text{Cu}(\text{NO}_3)_2^-$  after the second  $\text{O}^-$  abstraction, is  $3d^{9.33}$ . These calculations show the metal ion in  $\text{CuO}(\text{NO}_3)^-$  has an electronic configuration similar to  $\text{Cu}^+$ , whereas the copper ion in  $\text{CuO}_2^-$  has an electronic configuration similar to  $\text{Cu}^{2+}$ .

Comparison between the electronic configurations of the copper atom from the  $\text{O}^-$  abstraction in neutral  $\text{CuNO}_3 \rightarrow \text{CuO} + \text{NO}_2^\bullet$  and  $\text{O}^-$  abstraction in  $\text{Cu}(\text{NO}_3)_2^-$  were also explored. The influence of the nitrate ligand on the electronic structure and reactivity of CuO within the  $\text{CuO}(\text{NO}_3)^-$  cluster can be estimated from  $\text{O}^-$  abstraction of  $\text{CuNO}_3$ . This generates CuO without an additional nitrate anion. The copper ion charge is reduced from +0.809 in  $\text{CuNO}_3$  to +0.724 in CuO. This is opposite the expected change for oxidation. However, the difference can be attributed to the bonding electrons from oxygen interacting with the  $4s$  orbital of the copper. A slight decrease in the number of calculated  $3d$  electrons from  $3d^{9.94}$  in  $\text{Cu}(\text{NO}_3)$  to  $3d^{9.76}$  in CuO is predicted. This result indicates full oxidation of the copper ion is not expected upon  $\text{O}^-$  abstraction.

Table 7.3 summarizes the findings of this work. The loss of  $\text{NO}_3^\bullet$  from  $\text{Cu}(\text{NO}_3)_3^-$  results in the reduction of copper. However, the metal is not effectively oxidized after the first  $\text{O}^-$  abstraction and loss of  $\text{NO}_2^\bullet$  in  $\text{Cu}(\text{NO}_3)_2^-$ . Oxidation is expected upon the second  $\text{O}^-$  abstraction. Previously both  $\text{O}^-$  abstraction reactions were expected to oxidize the metal. This would require the copper atom in  $\text{CuO}(\text{NO}_3)^-$  to have a  $3d^9$  electron configuration. The copper atom in  $\text{CuO}_2^-$

would then have to have a +3 oxidation state.<sup>122</sup> This is contradictory to our calculations and observed reactivity. Reduction of  $\text{CuO}(\text{NO}_3)^-$  by electron transfer was not observed, but is expected if the metal has a  $3d^9$  configuration. Theoretical calculations predict the electron configuration of copper in  $\text{CuO}(\text{NO}_3)^-$  to be a  $3d^{10}$ , corresponding to  $\text{Cu}^+$ . The theoretical electron configuration for the copper atom in  $\text{CuO}_2^-$  is characteristic of a  $3d^9$  metal, meaning the copper atom is expected to be in the 2+ oxidation state.

Table 7.3: Summary of the decomposition reactions of copper nitrate anion clusters and the oxidation state of the metal in the reactant and product according to theoretical calculations.

Reaction	Type	Copper atom oxidation state	
		Reactant	Product
$\text{Cu}(\text{NO}_3)_3^- \rightarrow \text{Cu}(\text{NO}_3)_2^- + \text{NO}_3^\bullet$	Reduction	+2	+1
$\text{Cu}(\text{NO}_3)_2^- \rightarrow \text{CuO}(\text{NO}_3)^- + \text{NO}_2^\bullet$	--	+1	+1
$\text{CuO}(\text{NO}_3)^- \rightarrow \text{CuO}_2^- + \text{NO}_2^\bullet$	Oxidation	+1	+2

## 7.5 Conclusions

Three fragmentation reactions were observed in the decomposition of copper nitrate cluster anions: the loss of  $\text{NO}_3^-$ ,  $\text{NO}_3^\bullet$ , and  $\text{NO}_2^\bullet$ . It was determined the metal oxidation state dictates the preferred fragmentation reaction for each cluster. Loss of  $\text{NO}_3^\bullet$  was observed for  $\text{Cu}(\text{NO}_3)_3^-$ , whereas loss of  $\text{NO}_2^\bullet$  was observed for  $\text{Cu}(\text{NO}_3)_2^-$ . The difference in reactivity for each cluster was attributed to the metal ion electronic structure. The preferential loss of  $\text{NO}_3^\bullet$  results from electron transfer, which fills the  $3d$  subshell of copper in  $\text{Cu}(\text{NO}_3)_3^-$ .  $\text{O}^-$  abstraction, resulting in the loss of  $\text{NO}_2^\bullet$ , is observed in  $\text{Cu}(\text{NO}_3)_2^-$ . This is attributed to the completely filled  $3d$  subshell of copper in  $\text{Cu}(\text{NO}_3)_2^-$ . Theoretical calculations predicted copper is not fully oxidized upon  $\text{O}^-$

abstraction from  $\text{Cu}(\text{NO}_3)_2^-$ . However, oxidation is expected as a result of the dissociation of  $\text{CuO}(\text{NO}_3)^-$  into  $\text{CuO}_2^-$ . Theoretical analysis indicates reduction, oxidation, or no change in oxidation state may occur in the decomposition of metal-nitrate cluster anions. The type of reaction observed in a cluster is governed by the metal ion charge and electronic structure.

## CHAPTER 8

### CONCLUSIONS

#### 8.1 Summary of Dissertation

This dissertation has focused on making energetic measurements on gas-phase nitro containing anions. These fundamental measurements can be utilized in the design and development of new energetic materials. Two techniques were employed in this dissertation to accomplish this objective. Mass spectrometry was utilized to measure bond dissociation energies for a number of anionic species ranging from copper nitrate clusters to the three isomers of deprotonated nitrophenol. Photoelectron imaging was used to determine vertical detachment energies, electron affinities, as well as solvation energies. Individually, these two techniques provide key pieces of information needed to complete the negative-ion thermochemical cycle. This has been demonstrated through the work discussed in this dissertation.

#### 8.2 Conclusions from Photoelectron Imaging Studies

Chapter 3 describes the first study conducted using the homebuilt negative ion photoelectron imaging spectrometer described in Chapter 2. This study focused on  $\text{CH}^-$ . Photoelectron images were collected from 410 nm to 600 nm. Two electronic transitions,  $X^2\Pi \leftarrow X^3\Sigma^-$  and  $^4\Sigma^- \leftarrow X^3\Sigma^-$  were observed in the photoelectron spectra. These transitions were assigned to the removal of an electron from the  $1\pi$  and  $3\sigma$  orbitals of  $\text{CH}^-$ , respectively. The photoelectron angular distributions were analyzed using the qualitative  $s$  and  $p$  model and the quantitative mixed  $sp$  model. The  $s$  and  $p$  model did not accurately predict the sign of the anisotropy

parameter for detachment from the  $3\sigma$  orbital of  $\text{CH}^-$ . The mixed  $sp$  model did not accurately model the PAD corresponding to electron detachment from the  $3\sigma$  orbital. Further analysis shows the disagreement between experiment and the mixed  $sp$  model is the result of a temporary anion state. The temporary state has a lifetime sufficiently long to allow for molecular rotation before the electron is ejected, resulting in an isotropic distribution at low electron kinetic energies. This work provides evidence for a temporary anion excited state of  $\text{CH}^-$  not previously observed or predicted.

Chapter 4 contains the results of the second study using the negative photoelectron imaging spectrometer. In this work, the solvation effects, as well as ion energetic properties, were investigated for nitromethane and nitromethane cluster anions. These anions include the dimer and trimer clusters and hydrated nitromethane anion. Vertical detachment energies and estimated electron affinities were obtained from the photoelectron spectra. Differences in the vertical detachment energies were used to approximate the solvation energies of the clusters. The broad, featureless bands observed in the photoelectron spectra does not allow for direct assignment of the cluster structures. However, theoretical calculations were used to investigate the possible cluster geometries. The calculated structures agree well with experimental vertical detachment energies and estimated electron affinities. Using differences in the detachment energies, tentative structure assignments were made for the dimer and trimer cluster anions. Vibrational spectroscopy experiments are needed to confirm these assignments. Study of the calculated structures suggests the clusters are formed from a single nitromethane anion solvated by neutral nitromethane molecules through  $\text{O}\cdots\text{H}-\text{C}$  interactions.

### 8.3 Conclusions from Mass Spectrometry Studies

Chapter 5 focused on observing the fragmentation reactions of nitrobenzene and nitrotoluene radical anions. Additionally, this study was concerned with determining the C-N bond dissociation energies in nitrobenzene and nitrotoluene radical anions. CID spectra showed each nitroaromatic anion produced a single fragment,  $\text{NO}_2^-$ , under all experimental conditions. This shows other common decomposition reactions, such as nitro-to-nitrite rearrangement and loss of  $\text{NO}^\bullet$ , only occur in the neutral and cationic forms of the compounds studied. The C-N bond dissociation energies of each nitroaromatic radical anion were determined from the appearance energies of the  $\text{NO}_2^-$  fragment. Accurate energies were determined by modeling the threshold curves using CRUNCH4D. The dissociation energies were all determined to be approximately 2 eV. This work shows the position of the nitro substituent has a negligible influence on the strength of the C-N bond in nitrobenzene and the three nitrotoluene isomers. The anions were reported to have lower dissociation energies than the neutral species. This is attributed to the addition of the excess electron to the  $\pi^*$  orbital of the aromatic compound.

Chapter 6 discusses the results from CID and ERMS studies on the three isomers of deprotonated nitrophenol. From the CID studies, three common fragments were observed for each anion. These three fragments correspond to  $\text{C}_6\text{H}_4\text{O}^{\bullet-}$ ,  $\text{NO}_2^-$ , and  $\text{C}_6\text{H}_4\text{O}_2^{\bullet-}$ . An additional common fragment,  $\text{C}_5\text{H}_4\text{O}^{\bullet-}$ , was identified in the CID spectra of the *ortho* and *meta* isomers of deprotonated nitrophenol. ERMS spectra show the lowest energy fragment for each isomer is  $\text{C}_6\text{H}_4\text{O}_2^{\bullet-}$ . This fragment has an appearance energy between 2.5 eV and 3 eV. The  $\text{C}_6\text{H}_4\text{O}^{\bullet-}$  fragment appears between 3 eV and 4 eV for all compounds in this work. Good agreement was found between the theoretical calculations of the nitro-to-nitrite isomerization barrier and the measured appearance energies. The appearance energies for the  $\text{NO}_2^-$  and  $\text{C}_5\text{H}_4\text{O}^{\bullet-}$  fragments are

between 3 and 3.5 eV for the *ortho* and *meta* isomers. The appearance energy for these fragments is approximately 4 eV for the *para* isomer. In general, there is good agreement between the experimental dissociation energies and theoretical calculations. The C-N bond dissociation energies of the deprotonated nitrophenol anions were compared to the corresponding neutrals and nitrotoluene neutral and radical anions. These results show the C-N bond energy increases for the deprotonated nitrophenol anions. This is attributed to the stabilization of the nitrophenoxide anion.

Chapter 7 explored the fragmentation reactions of copper nitrate anion clusters using tandem mass spectrometry. The results from this work show the oxidation state of the metal determine the fragmentation reactions each cluster anion undergoes. Clusters containing copper (II) underwent the loss of  $\text{NO}_3^\bullet$  but not loss  $\text{NO}_2^\bullet$ . Copper (I) containing clusters undergo the loss of  $\text{NO}_2^\bullet$  but not the loss of  $\text{NO}_3^\bullet$ . This difference was attributed to the reactivity of the *3d* subshell of the copper ion. In  $\text{Cu}(\text{NO}_3)_3^-$  the *3d* subshell is filled upon electron transfer, resulting in the preferential loss of  $\text{NO}_3^\bullet$ . During this process the copper atom is reduced. In the case of  $\text{Cu}(\text{NO}_3)_2$  clusters, the completely filled copper *3d* subshell causes a different reaction to occur. The nitrate ligand donates an electron from an oxygen lone pair into the empty Cu *4s* orbital. This causes  $\text{O}^-$  abstraction and formation of a metal oxide bond. Theoretical calculations suggests the copper atom is not oxidized upon  $\text{O}^-$  abstraction for the from  $\text{Cu}(\text{NO}_3)_2^-$  to produce  $\text{CuO}(\text{NO}_3)$ . However, oxidation is expected to occur in the dissociation of  $\text{CuO}(\text{NO}_3)^-$  to form  $\text{CuO}_2^-$ . The major conclusion from this work suggests the type of fragmentation reaction observed in a cluster is dependent on the charge and the electronic structure of the metal ion.

## REFERENCES

1. Pruitt, C. J. M.; Benham, K.; Bandyopadhyay, B.; Goebbert, D. J., Fragmentation of deprotonated nitrophenol anions. *Chem. Phys. Lett.* **2014**, *614*, 192.
2. Pruitt, C. J. M.; Goebbert, D. J., The C–N dissociation energies of nitrobenzene and nitrotoluene radical anions and neutrals. *Chem. Phys. Lett.* **2013**, *580*, 21.
3. Wang, Q.; Wang, J.; Larranaga, M., Simple relationship for predicting onset temperatures of nitro compounds in thermal explosions. *J. Therm. Anal. Calorim.* **2013**, *111*, 1033.
4. Song, X.-S.; Cheng, X.-L.; Yang, X.-D.; He, B., Relationship between the Bond Dissociation Energies and Impact Sensitivities of Some Nitro-Explosives. *Propell., Explos., Pyrot.* **2006**, *31*, 306.
5. *German Explosive Ordnance*, Department of the Army and the Air Force, 1953.
6. *Hearings Before the Electronic Battlefield Subcommittee of the Preparedness Investigating Subcommittee of the Committee on Armed Services*, United States Senate, 1971.
7. *Military Explosives*, Department of the Army, 1984.
8. Krzmarzick, M. J.; Khatiwada, R.; Olivares, C. I.; Abrell, L.; Sierra-Alvarez, R.; Chorover, J.; Field, J. A., Biotransformation and Degradation of the Insensitive Munitions Compound, 3-Nitro-1,2,4-triazol-5-one, by Soil Bacterial Communities. *Environ. Sci. Technol.* **2015**, *49*, 5681.
9. Felt, D.; Johnson, J. L.; Larson, S.; Hubbard, B.; Henry, K.; Nestler, C.; Ballard, J. H. *Evaluation of Treatment Technologies for Wastewater from Insensitive Munitions Production*, US Army Corps of Engineers, 2013.
10. Cohen, R.; Zeiri, Y.; Wurzburg, E.; Kosloff, R., Mechanism of Thermal Unimolecular Decomposition of TNT(2,4,6-Trinitrotoluene): A DFT Study. *J. Phys. Chem. A* **2007**, *111*, 11074.
11. Hause, M. L.; Herath, N.; Zhu, R.; Lin, M. C.; Suits, A. G., Roaming-mediated isomerization in the photodissociation of nitrobenzene. *Nat. Chem.* **2011**, *3*, 932.
12. Rice, B. M.; Sahu, S.; Owens, F. J., Density functional calculations of bond dissociation energies for NO<sub>2</sub> scission in some nitroaromatic molecules. *J. Mol. Struct.: THEOCHEM* **2002**, *583*, 69.

13. Fried, L. E.; Ruggiero, A. J., Energy Transfer Rates in Primary, Secondary, and Insensitive Explosives. *J. Phys. Chem.* **1994**, *98*, 9786.
14. McNesby, K. L.; Coffey, C. S., Spectroscopic Determination of Impact Sensitivities of Explosives. *J. Phys. Chem. B* **1997**, *101*, 3097.
15. Mullan, J., A Relationship between Impact Sensitivity and Molecular Electronegativity. *Propell., Explos., Pyrot.* **1987**, *12*, 60.
16. Mullan, J., Relationships between Impact Sensitivity and Molecular Electronic Structure. *Propell., Explos., Pyrot.* **1987**, *12*, 121.
17. Vaullerain, M.; Espagnacq, A.; Morin-Allory, L., Prediction of Explosives Impact Sensitivity. *Propellants, Explos., Pyrotech.* **1998**, *23*, 237.
18. Delpuech, A.; Cherville, J., Relation entre la Structure Electronique et la Sensibilité au Choc des Explosifs Secondaires Nitrés-Critère Moléculaire de Sensibilité. I. Cas des Nitroaromatiques et des Nitramines. *Propell., Explos., Pyrot.* **1978**, *3*, 169.
19. Delpuech, A.; Cherville, J., Relation entre La Structure Electronique et la Sensibilité au Choc des Explosifs Secondaires Nitrés. Critère Moléculaire de Sensibilité II. Cas des esters nitriques. *Propell., Explos., Pyrot.* **1979**, *4*, 121.
20. Delpuech, A.; Cherville, J., Relation entre La Structure Electronique et la Sensibilité au Choc des Explosifs Secondaires Nitrés. III. Influence de l'environnement cristallin. *Propell., Explos., Pyrot.* **1979**, *4*, 61.
21. Armentrout, P. B., Mass spectrometry—not just a structural tool: the use of guided ion beam tandem mass spectrometry to determine thermochemistry. *J. Am. Soc. Mass Spectrom.* **2002**, *13*, 419.
22. Ervin, K. M.; Lineberger, W. C. *Advances in Gas Phase Ion Chemistry*, 1992.
23. Chandler, D. W.; Houston, P. L., Two-Dimensional Imaging of State-Selected Photodissociation Products Detected by Multiphoton Ionization. *J. Chem. Phys.* **1987**, *87*, 1445.
24. Eppink, A.; Parker, D. H., Velocity map imaging of ions and electrons using electrostatic lenses: Application in photoelectron and photofragment ion imaging of molecular oxygen. *Rev. Sci. Instrum.* **1997**, *68*, 3477.
25. Surber, E.; Mabbs, R.; Sanov, A., Probing the electronic structure of small molecular anions by photoelectron imaging. *J. Phys. Chem. A* **2003**, *107*, 8215.
26. Wiley, W. C.; McLaren, I. H., Time-of-Flight Mass Spectrometer with Improved Resolution. *Rev. Sci. Instrum.* **1955**, *26*, 1150.

27. Johnson, M. A.; Lineberger, W. C. In *Techniques for the Study of Ion Molecule Reactions*; Farrar, J. M., Saunders, W. H., Eds.; Wiley: New York, 1988, p 591.
28. Heck, A. J. R.; Chandler, D. W., Imaging Techniques For the Study of Chemical-Reaction Dynamics. *Annu. Rev. Phys. Chem.* **1995**, *46*, 335.
29. Dribinski, V.; Ossadtchi, A.; Mandelshtam, V. A.; Reisler, H., Reconstruction of Abel-transformable images: The Gaussian basis-set expansion Abel transform method. *Rev. Sci. Instrum.* **2002**, *73*, 2634.
30. Cooper, J.; Zare, R. N. In *Atomic collision processes*; Geltman, S., Mahanthappa, K. T., Brittin, W. E., Eds.; Gordon and Breach, Science Publishers: New York, London, Paris, 1968; Vol. XI-C, p 317.
31. Cooper, J.; Zare, R. N., Angular Distributions in Atomic Anion Photodetachment (Erratum). *J. Chem. Phys.* **1968**, *49*, 4252.
32. Fenn, J. B.; Mann, M.; Meng, C. K.; Wong, S. F.; Whitehouse, C. M., Electrospray ionization for mass-spectrometry of large biomolecules. *Science* **1989**, *246*, 64.
33. Carroll, D. I.; Dzidic, I.; Stillwell, R. N.; Horning, M. G.; Horning, E. C., Subpicogram detection system for gas phase analysis based upon atmospheric pressure ionization (API) mass spectrometry. *Anal. Chem.* **1974**, *46*, 706.
34. Taylor, G. *Disintegration of Water Drops in an Electric Field*, 1964; Vol. 280.
35. Muntean, F.; Armentrout, P. B., Guided ion beam study of collision-induced dissociation dynamics: integral and differential cross sections. *J. Chem. Phys.* **2001**, *115*, 1213.
36. Ervin, K. M.; Armentrout, P. B., Translational energy dependence of  $\text{Ar}^+ + \text{XY} \rightarrow \text{ArX}^+ + \text{Y}$  ( $\text{XY} = \text{H}_2, \text{D}_2, \text{HD}$ ) from thermal to 30 eV c.m. *J. Chem. Phys.* **1985**, *83*, 166.
37. Lambert, D. L., The abundances of the elements in the solar photosphere - VIII. Revised abundances of carbon, nitrogen, and oxygen. *Mon. Not. R. Astr. Soc.* **1978**, *182*, 249.
38. Rydbeck, O. E. H.; Ellder, J.; Irvine, W. M., Radio Detection of Interstellar CH. *Nature* **1973**, *246*, 466.
39. Turner, B. E.; Zuckerman, B., Microwave Detection of Interstellar CH. *Astrophys. J. Lett.* **1974**, *187*, L59.
40. Loris, M.; Susan, Z.; Dame, T. M.; Ben, E., CH 3GHz Observations of the Galactic Center. *Astrophys. J.* **2006**, *636*, 267.
41. Bleekrode, R.; Nieuwpoort, W. C., Absorption and Emission Measurements of  $\text{C}_2$  and CH Electronic Bands in Low-Pressure Oxyacetylene Flames. *J. Chem. Phys.* **1965**, *43*, 3680.

42. Barnard, J. A.; Bradley, J. N. *Flame and Combustion*; Chapman & Hall: London, UK, 1985.
43. Feldmann, D., Photodetachment of electrons in some stable negative ions. *Z. Naturforsch.* **1970**, *25 A*, 621.
44. Kasdan, A.; Herbst, E.; Lineberger, W. C., Laser Photoelectron spectrometry of  $\text{CH}^-$ . *Chem. Phys. Lett.* **1975**, *31*, 78.
45. Okumura, M.; Yeh, L. I.; Normand, D.; Lee, Y. T., The lifetimes for spontaneous emission from the  $X^3\Sigma^-(v=1)$  and a  $^1\Delta$  states of  $\text{CH}^-$ . *J. Chem. Phys.* **1986**, *85*, 1971.
46. Bandyopadhyay, B.; Pruitt, C. J. M.; Goebbert, D. J., Communication: Photoelectron angular distributions of  $\text{CH}^-$  reveal a temporary anion state. *J. Chem. Phys.* **2013**, *138*, 201101.
47. Cavanagh, S. J.; Gibson, S. T.; Gale, M. N.; Dedman, C. J.; Roberts, E. H.; Lewis, B. R., High-resolution velocity-map-imaging photoelectron spectroscopy of the  $\text{O}^-$  photodetachment fine-structure transitions. *Phys Rev A* **2007**, *76*, 052708.
48. Neumark, D. M.; Lykke, K. R.; Andersen, T.; Lineberger, W. C., Laser Photodetachment Measurement of the Electron-Affinity of Atomic Oxygen. *Phys Rev A* **1985**, *32*, 1890.
49. Goebbert, D. J., Photoelectron imaging of  $\text{CH}^-$ . *Chem. Phys. Lett.* **2012**, *551*, 19.
50. Sanov, A.; Grumbling, E. R.; Goebbert, D. J.; Culberson, L. M., Photodetachment anisotropy for mixed s-p states: 8/3 and other fractions. *J. Chem. Phys.* **2013**, *138*, 054311.
51. Goebbert, D. J.; Khuseynov, D.; Sanov, A., Photodissociation of nitromethane cluster anions. *J. Chem. Phys.* **2010**, *133*.
52. Bethe, H. A., *Handbuch der Physik* **1933**, *24*, 483.
53. Hanstorp, D.; Bengtsson, C.; Larson, D. J., Angular distributions in photodetachment from  $\text{O}^-$ . *Phys Rev A* **1989**, *40*, 670.
54. Grumbling, E. R.; Sanov, A., Photoelectron angular distributions in negative-ion photodetachment from mixed sp states. *J. Chem. Phys.* **2011**, *135*, 164302.
55. Grumbling, E. R. PhD, The University of Arizona, 2010.
56. Goebbert, D. J.; Sanov, A., Photodetachment, photofragmentation and fragment autodetachment of  $[\text{O}_{2n}(\text{H}_2\text{O})_m]^-$  clusters, core-anion structures and fragment energy partitioning. *J. Chem. Phys.* **2009**, *131*, 104308.
57. Khuseynov, D.; Goebbert, D. J.; Sanov, A., Oxygen cluster anions revisited: Solvent-mediated dissociation of the core  $\text{O}_4^-$  anion. *J. Chem. Phys.* **2012**, *136*, 094312.

58. Mbaiwa, F.; Wei, J.; Van Duzor, M.; Mabbs, R., Threshold effects in  $\Gamma\cdot\text{CH}_3\text{CN}$  and  $\Gamma\cdot\text{H}_2\text{O}$  cluster anion detachment: The angular distribution as an indicator of electronic autodetachment. *J. Chem. Phys.* **2010**, *132*, 134304.
59. Runjun, L.; Hanold, K. A.; Garner, M. C.; Luong, A. K.; Continetti, R. E., Excited state dynamics in clusters of oxygen. *Faraday Discuss.* **1997**, *108*, 115.
60. Alizadeh, E.; Ferreira da Silva, F.; Zappa, F.; Mauracher, A.; Probst, M.; Denfil, S.; A, B.; Maerk, T. D.; Limao-Viera, P.; Scheier, P., Dissociative electron attachment to nitromethane. *Int. J. Mass Spectrom. and Ion Processes* **2008**, *271*, 15.
61. Compton, R. N.; Carman, H. S.; Desfrancois, C.; Abdoul-Carime, H.; Schermann, J. P.; Hendricks, J. H.; Lyapustina, S. A.; Bowen, K. H., On the binding of electrons to nitromethane: Dipole and valence bound anions. *J. Chem. Phys.* **1996**, *105*, 3472.
62. Stockdale, J. A.; Davis, F. J.; Compton, R. N.; Klots, C. E., Production of negative ions from  $\text{CH}_3\text{X}$  molecules ( $\text{CH}_3\text{NO}_2$ ,  $\text{CH}_3\text{CN}$ ,  $\text{CH}_3\text{I}$ ,  $\text{CH}_3\text{Br}$ ) by electron impact and by collisions with atoms in excited Rydberg states. *J. Chem. Phys.* **1974**, *60*, 4279.
63. Lobo, R. F. M.; Moutinho, A. M. C.; Lacmann, K.; Los, J., Excitation of the Nitro-Group in Nitromethane by Electron-Transfer. *J. Chem. Phys.* **1991**, *95*, 166.
64. Brooks, P. R.; Harland, P. W.; Harris, S. A.; Kennair, T.; Redden, C.; Tate, J. F., Steric effects in electron transfer from potassium to pi-bonded oriented molecules  $\text{CH}_3\text{CN}$ ,  $\text{CH}_3\text{NC}$ , and  $\text{CCl}_3\text{CN}$ . *J. Am. Chem. Soc.* **2007**, *129*, 15572.
65. Brooks, P. R.; Harland, P. W.; Redden, C. E., Electron transfer from sodium to oriented nitromethane,  $\text{CH}_3\text{NO}_2$ : Probing the spatial extent of unoccupied orbitals. *J. Am. Chem. Soc.* **2006**, *128*, 4773.
66. Brooks, P. R.; Harland, P. W.; Redden, C. E., Steric asymmetry in electron transfer from potassium atoms to oriented nitromethane ( $\text{CH}_3\text{NO}_2$ ) molecules. *J. Phys. Chem. A* **2006**, *110*, 4697.
67. Adams, C. L.; Schneider, H.; Ervin, K. M.; Weber, J. M., Low-energy photoelectron imaging spectroscopy of nitromethane anions: Electron affinity, vibrational features, anisotropies, and the dipole-bound state. *J. Chem. Phys.* **2009**, *130*, 074307.
68. Goebbert, D. J.; Pichugin, K.; Sanov, A., Low-lying electronic states of  $\text{CH}_3\text{NO}_2$  via photoelectron imaging of the nitromethane anion. *J. Chem. Phys.* **2009**, *131*, 164308.
69. Marcum, J. C.; Weber, J. M., Microhydration of Nitromethane Anions from Both a Solute and Solvent Perspective. *J. Phys. Chem. A* **2010**, *114*, 8933.

70. Schneider, H.; Vogelhuber, K. M.; Schinle, F.; Stanton, J. F.; Weber, J. M., Vibrational spectroscopy of nitroalkane chains using electron autodetachment and Ar predissociation. *J. Phys. Chem. A* **2008**, *112*, 7498.
71. Robertson, W. H.; Price, E.; Weber, J. M.; Shin, J.-W.; Weddle, G. M.; Johnson, M. A., Infrared Signatures of a Water Molecule Attached to Triatomic Domains of Molecular Anions: Evolution of the H-bonding Configuration with Domain Length. *J. Phys. Chem. A* **2003**, *107*, 6527.
72. Weber, J. M.; Kelley, J. A.; Robertson, W. H.; Johnson, M. A., Hydration of a structured excess charge distribution: Infrared spectroscopy of the  $\text{O}_2^{\bullet-}(\text{H}_2\text{O})_n$ , ( $1 \leq n \leq 5$ ) clusters. *J. Chem. Phys.* **2001**, *114*, 2698.
73. Motegi, H.; Takayanagi, T.; Tsuneda, T.; Yagi, K.; Nakanishi, R.; Nagata, T., Theoretical Study on the Excess Electron Binding Mechanism in the  $[\text{CH}_3\text{NO}_2 \cdot (\text{H}_2\text{O})_n]^-$  ( $n = 1-6$ ) Anion Clusters. *J. Phys. Chem. A* **2010**, *114*, 8939.
74. Nakanishi, R.; Nagata, T., Formation and photodestruction of dual dipole-bound anion  $(\text{H}_2\text{O})_6\{\text{e}^-\}\text{CH}_3\text{NO}_2$ . *J. Chem. Phys.* **2009**, *130*, 224309.
75. Frisch, M. J.; Pople, J. A.; Binkley, J. S., Self-consistent molecular orbital methods 25. Supplementary functions for Gaussian basis sets. *J. Chem. Phys.* **1984**, *80*, 3265.
76. Frisch, M. J.; Trucks, G. W.; Schlegel, H. B.; Scuseria, G. E.; Robb, M. A.; Cheeseman, J. R.; Scalmani, G.; Barone, V.; Mennucci, B.; Petersson, G. A.; Nakatsuji, H.; Caricato, M.; Li, X.; Hratchian, H. P.; Izmaylov, A. F.; Bloino, J.; Zheng, G.; Sonnenberg, J. L.; Hada, M.; Ehara, M.; Toyota, K.; Fukuda, R.; Hasegawa, J.; Ishida, M.; Nakajima, T.; Honda, Y.; Kitao, O.; Nakai, H.; Vreven, T.; Montgomery, J., J. A.; Peralta, J. E.; Ogliaro, F.; Bearpark, M.; Heyd, J. J.; Brothers, E.; Kudin, K. N.; Staroverov, V. N.; Kobayashi, R.; Normand, J.; Raghavachari, K.; Rendell, A.; Burant, J. C.; Iyengar, S. S.; Tomasi, J.; Cossi, M.; Rega, N.; Millam, N. J.; Klene, M.; Knox, J. E.; Cross, J. B.; Bakken, V.; Adamo, C.; Jaramillo, J.; Gomperts, R.; Stratmann, R. E.; Yazyev, O.; Austin, A. J.; Cammi, R.; Pomelli, C.; Ochterski, J. W.; Martin, R. L.; Morokuma, K.; Zakrzewski, V. G.; Voth, G. A.; Salvador, P.; Dannenberg, J. J.; Dapprich, S.; Daniels, A. D.; Farkas, Ö.; Foresman, J. B.; Ortiz, J. V.; Cioslowski, J.; Fox, D. J., Gaussian 09, Revision C.01. **2010**.
77. Becke, A. D., Density-Functional Exchange-Energy Approximation with Correct Asymptotic-Behavior. *Phys Rev A* **1988**, *38*, 3098.
78. Becke, A. D., Density-Functional Thermochemistry .3. The Role of Exact Exchange. *J. Chem. Phys.* **1993**, *98*, 5648.
79. Ditchfield, R.; Hehre, W. J.; Pople, J. A., Self-Consistent Molecular-Orbital Methods. IX. An Extended Gaussian-Type Basis for Molecular-Orbital Studies of Organic Molecules. *J. Chem. Phys.* **1971**, *54*, 724.

80. Clark, T.; Chandrasekhar, J.; Spitnagel, G. W.; Schleyer, P. v. R., Efficient diffuse function-augmented basis sets for anion calculations. III. The 3-21+G basis set for the first-row elements, Li-F. *J. Comput. Chem.* **1983**, *4*, 294.
81. Kendall, R. A.; Dunning, T. H.; Harrison, R. J., Electron affinities of the first-row atoms revisited. Systematic basis sets and wave functions. *J. Chem. Phys.* **1992**, *96*, 6796.
82. Grumblin, E. R.; Sanov, A., Solvation effects on angular distributions in  $\text{H}^-(\text{NH}_3)_n$  and  $\text{NH}_2^-(\text{NH}_3)_n$  photodetachment: Role of solute electronic structure. *J. Chem. Phys.* **2011**, *135*, 164301.
83. Myshakin, E. M.; Jordan, K. D.; Robertson, W. H.; Weddle, G. H.; Johnson, M. A., Dominant structural motifs of  $\text{NO}^-\bullet(\text{H}_2\text{O})_n$  complexes: Infrared spectroscopic and ab initio studies. *J. Chem. Phys.* **2003**, *118*, 4945.
84. Wincel, H., Gas-phase solvation of  $\text{Cl}^-$ ,  $\text{NO}_2^-$ ,  $\text{CH}_2\text{NO}_2^-$ ,  $\text{CH}_3\text{NO}_2^-$  and  $\text{CH}_3\text{NO}_4^-$  by  $\text{CH}_3\text{NO}_2$ . *Int. J. Mass Spec.* **2003**, *226*, 341.
85. Brill, T. B.; James, K. J.; Chawla, R.; Nicol, G.; Shukla, A.; Futrell, J. H., Influence of the substituent on the major decomposition channels of the  $\text{NO}_2$  group in para-substituted nitrobenzenes: a tandem mass spectrometric study. *J. Phys. Org. Chem.* **1999**, *12*, 819.
86. Nguyen, V. S.; Vinckier, C.; Hue, T. T.; Nguyen, M. T., Decomposition Mechanism of the Anions Generated by Atmospheric Pressure Chemical Ionization of Nitroanilines. *J. Phys. Chem. A* **2005**, *109*, 10954.
87. Gonzalez, A. C.; Larson, C. W.; McMillen, D. F.; Golden, D. M., Mechanism of Decomposition of Nitroaromatics. Laser-Powered Homogeneous Pyrolysis of Substituted Nitrobenzenes. *J. Phys. Chem.* **1985**, *89*, 4809.
88. Fayet, G.; Joubert, L.; Rotureau, P.; Adamo, C., A Theoretical Study of the Decomposition Mechanisms in Substituted o-Nitrotoluenes. *J. Phys. Chem. A* **2009**, *113*, 13621.
89. Tsang, W.; Robaugh, D.; Mallard, W. G., Single-pulse shock-tube studies on C- $\text{NO}_2$  bond cleavage during the decomposition of some nitro aromatic compounds. *J. Phys. Chem.* **1986**, *90*, 5968.
90. Chowdhury, S.; Heinis, T.; Grimsrud, E. P.; Kebarle, P., Entropy changes and electron affinities from gas-phase electron-transfer equilibria:  $\text{A}^- + \text{B} = \text{A} + \text{B}$ . *J. Phys. Chem.* **1986**, *90*, 2747.
91. Chowdhury, S.; Kishi, H.; Dillow, G. W.; Kebarle, P., Electron affinities of substituted nitrobenzenes. *Can. J. Chem.* **1989**, *67*, 603.
92. Ervin, K. M.; Ho, J.; Lineberger, W. C., Ultraviolet Photoelectron-Spectrum of  $\text{NO}_2^-$ . *J. Phys. Chem.* **1988**, *92*, 5405.

93. McMillen, D. F.; Golden, D. M., Hydrocarbon Bond Dissociation Energies. *Annu. Rev. Phys. Chem.* **1982**, *33*, 493.
94. Steill, J. D.; Oomens, J., Spectroscopically resolved competition between dissociation and detachment from nitrobenzene radical anion. *Int. J. Mass Spectrom.* **2011**, *308*, 239.
95. Desfrancois, C.; Periquet, V.; Lyapustina, S. A.; Lippa, T. P.; Robinson, D. W.; Bowen, K. H.; Nonaka, H.; Compton, R. N., Electron binding to valence and multipole states of molecules: Nitrobenzene, para- and meta-dinitrobenzenes. *J. Chem. Phys.* **1999**, *111*, 4569.
96. Batz, M. L.; Garland, P. M.; Reiter, R. C.; Sanborn, M. D.; Stevenson, C. D., Explosion and Ion Association Chemistry of the Anion Radicals of 2,4,6-Trinitrotoluene, 2,6-Dinitrotoluene, and Trinitrobenzene. *J. Org. Chem.* **1997**, *62*, 2045.
97. Godovikova, T. I.; Karpenko, N. F.; Vozchikova, S. A.; Ignat'eva, E. L., Mass Spectrometric Study of Substituted 5- or 4-Nitro-1,2,3-triazole 1-Oxides. *Chem. Heterocycl. Compd.* **2002**, *38*, 1475.
98. Cassady, C. J.; McElvany, S. W., Collision-induced dissociation and photodissociation of nitroaromatic molecular ions: A unique isomerization for p-nitrotoluene and p-ethylnitrobenzene ions. *Org. Mass Spectrom.* **1993**, *28*, 1650.
99. Asfandiarov, N. L.; Pshenichnyuk, S. A.; Lukin, V. G.; Pshenichnyuk, I. A.; Modelli, A.; Matejčík, Š., Temporary anion states and dissociative electron attachment to nitrobenzene derivatives. *Int. J. Mass Spectrom.* **2007**, *264*, 22.
100. Edtbauer, A.; Sulzer, P.; Mauracher, A.; Mitterdorfer, C.; Ferreira da Silva, F.; Denifl, S.; Märk, T. D.; Probst, M.; Nunes, Y.; Limão-Vieira, P.; Scheier, P., Dissociative electron attachment to pentaerythritol tetranitrate: Significant fragmentation near 0 eV. *J. Chem. Phys.* **2010**, *132*, 134305.
101. Sulzer, P.; Mauracher, A.; Denifl, S.; Probst, M.; Märk, T. D.; Scheier, P.; Illenberger, E., Probing di-nitrobenzene by low energy electrons: Identification of isomers via resonances in dissociative electron attachment. *Int. J. Mass Spectrom.* **2007**, *266*, 138.
102. Sulzer, P.; Mauracher, A.; Ferreira da Silva, F.; Denifl, S.; Märk, T. D.; Probst, M.; Limão-Vieira, P.; Scheier, P., Probing royal demolition explosive (1,3,5-trinitro-1,3,5-triazocyclohexane) by low-energy electrons: Strong dissociative electron attachment near 0 eV. *J. Chem. Phys.* **2009**, *131*, 144304.
103. Sulzer, P.; Rondino, F.; Ptasinska, S.; Illenberger, E.; Märk, T. D.; Scheier, P., Probing trinitrotoluene (TNT) by low-energy electrons: Strong fragmentation following attachment of electrons near 0 eV. *Int. J. Mass Spectrom.* **2008**, *272*, 149.
104. Modelli, A.; Venuti, M., Empty level structure and dissociative electron attachment in gas-phase nitro derivatives. *Int. J. Mass Spectrom.* **2001**, *205*, 7.

105. Pelc, A.; Scheier, P.; Märk, T. D., Low-energy electron interaction with nitrobenzene:  $C_6H_5NO_2$ . *Vacuum* **2007**, *81*, 1180.
106. Muftakhov, M. V.; Khatymov, R. V.; Shchukin, P. V.; Pogulay, A. V.; Mazunov, V. A., Rearrangement and predissociation processes in negative molecular ions of nitrobenzenes. *J. Mass Spectrom.* **2010**, *45*, 82.
107. Hammad, L. A.; Wenthold, P. G., Triradical Thermochemistry from Collision-Induced Dissociation Threshold Energy Measurements. The Heat of Formation of 1,3,5-Trimethylenebenzene. *J. Am. Chem. Soc.* **2001**, *123*, 12311.
108. Fayet, G.; Joubert, L.; Rotureau, P.; Adamo, C., Theoretical study of the decomposition reactions in substituted nitrobenzenes. *J. Phys. Chem. A* **2008**, *112*, 4054.
109. Shao, Y. H.; Head-Gordon, M.; Krylov, A. I., The spin-flip approach within time-dependent density functional theory: Theory and applications to diradicals. *J. Chem. Phys.* **2003**, *118*, 4807.
110. Tan, B.; Long, X.; Peng, R.; Li, H.; Jin, B.; Chu, S.; Dong, H., Two important factors influencing shock sensitivity of nitro compounds: Bond dissociation energy of X-NO<sub>2</sub> (X=C, N, O) and Mulliken charges of nitro group. *J. Hazard. Mater.* **2010**, *183*, 908.
111. Li, J., A quantitative relationship for the shock sensitivities of energetic compounds based on X-NO<sub>2</sub> (X = C, N, O) bond dissociation energy. *J. Hazard. Mater.* **2010**, *180*, 768.
112. Li, J., A multivariate relationship for the impact sensitivities of energetic N-nitrocompounds based on bond dissociation energy. *J. Hazard. Mater.* **2010**, *174*, 728.
113. Dacons, J. C.; Adolph, H. G.; Kamlet, M. J., Some Novel Observations Concerning the Thermal Decomposition of 2,4,6-Trinitrotoluene. *J. Phys. Chem.* **1970**, *74*, 3035.
114. Brill, T. B.; James, K. J., Kinetics and Mechanisms of Thermal Decomposition of Nitroaromatic Explosives. *Chem. Rev.* **1993**, *93*, 2667.
115. Rogers, R. N.; Janney, J. L.; Ebinger, M. H., Kinetic-Isotope Effects in Thermal Explosions. *Thermochim. Acta* **1982**, *59*, 287.
116. Collins, L. W.; Haws, L. D., The Thermochemistry of Explosives. *Thermochim. Acta* **1977**, *21*, 1.
117. Rogers, R. N., Thermochemistry of Explosives. *Thermochim. Acta* **1975**, *11*, 131.
118. Bunn, T. L.; Richard, A. M.; Baer, T., Photodissociation of the energy selected nitrobenzene ion. *J. Chem. Phys.* **1986**, *84*, 1424.
119. Nishimura, T.; Das, P. R.; Meisels, G. G., On the dissociation dynamics of energy-selected nitrobenzene ion. *J. Chem. Phys.* **1986**, *84*, 6190.

120. Osterheld, T. H.; Baer, T.; Brauman, J. I., Infrared multiple-photon dissociation of the nitrobenzene radical cation. A paradigm for competitive reactions. *J. Am. Chem. Soc.* **1993**, *115*, 6284.
121. Bartmess, J. E. In *NIST Chemistry WebBook, NIST Standard Reference Database Number 69*; Linstrom, P. J., Mallard, W. G., Eds.; National Institute of Standards and Technology: Gaithersburg MD, 20899, <http://webbook.nist.gov> (retrieved February 5, 2015), 2015.
122. Frański, R.; Sobieszczuk, K.; Gierczyk, B., Mass spectrometric decomposition of  $[M^{n+}(\text{NO}_3^-)_{n+1}]^-$  anions originating from metal nitrates  $M(\text{NO}_3)_n$ . *Int. J. Mass Spectrom.* **2014**, *369*, 98.
123. Li, F.; Byers, M.; Houk, R. S., Tandem mass spectrometry of metal nitrate negative ions produced by electrospray ionization. *J. Am. Soc. Mass Spectrom.* **2003**, *14*, 671.
124. Schröder, D.; de Jong, K. P.; Roithová, J., Gas-Phase Model Studies Relevant to the Decomposition of Transition-Metal Nitrates  $M(\text{NO}_3)_2$  ( $M = \text{Co}, \text{Ni}$ ) into Metal–Oxo Species. *Eur. J. Inorg. Chem.* **2009**, *2009*, 2121.
125. Kaufman, S. H.; Weber, J. M., Photodissociation Spectroscopy of the Anionic Copper Nitrate Association Complex  $\text{Cu}(\text{NO}_3)_3^-$ . *J. Phys. Chem. A* **2014**, *118*, 9687.
126. Hathaway, B. J.; Underhill, A. E., 433. The ultraviolet and visible spectra of some anhydrous copper(II) salts in organic solvents. *J. Chem. Soc.* **1962**, 2257.
127. Pruitt, C. J. M.; Goebbert, D. J., Experimental and Theoretical Study of the Decomposition of Copper Nitrate Cluster Anions. *J. Phys. Chem. A* **2015**, *119*, 4755.
128. Reed, A. E.; Weinstock, R. B.; Weinhold, F., Natural population analysis. *J. Chem. Phys.* **1985**, *83*, 735.
129. Hongo, Y.; Li, B.; Suzuki, K.; Nakamura, T., An unexpected  $[M+I]^+$  ion formation in phosphasilene compounds detection by electrospray ionization mass spectrometry. *J. Mass Spectrom.* **2011**, *46*, 956.
130. Liu, P.; Lanekoff, I. T.; Laskin, J.; Dewald, H. D.; Chen, H., Study of Electrochemical Reactions Using Nanospray Desorption Electrospray Ionization Mass Spectrometry. *Anal. Chem.* **2012**, *84*, 5737.
131. Boys, B. L.; Kuprowski, M. C.; Noël, J. J.; Konermann, L., Protein Oxidative Modifications During Electrospray Ionization: Solution Phase Electrochemistry or Corona Discharge-Induced Radical Attack? *Anal. Chem.* **2009**, *81*, 4027.
132. Gatlin, C. L.; Turecek, F.; Vaisar, T., Determination of Soluble Cu(I) and Cu(II) Species in Jet Fuel by Electrospray Ionization Mass Spectrometry. *Anal. Chem.* **1994**, *66*, 3950.

133. Vaisar, T.; Gatlin, C. L.; Tureček, F., Metal-ligand redox reactions in gas-phase quaternary peptide-metal complexes by electrospray ionization mass spectrometry. *Int. J. Mass Spectrom. and Ion Processes* **1997**, *162*, 77.
134. Vaisar, T.; Gatlin, C. L.; Tureček, F., Oxidation of Peptide–Copper Complexes by Alkali Metal Cations in the Gas Phase. *J. Am. Chem. Soc.* **1996**, *118*, 5314.
135. Blades, A. T.; Jayaweera, P.; Ikononou, M. G.; Kebarle, P., Ion-molecule clusters involving doubly charged metal ions ( $M^{2+}$ ). *Int. J. Mass Spectrom. and Ion Processes* **1990**, *102*, 251.
136. Lavanant, H.; Virelizier, H.; Hoppilliard, Y., Reduction of copper(II) complexes by electron capture in an electrospray ionization source. *J. Am. Soc. Mass Spectrom.* **1998**, *9*, 1217.
137. Weaver, A.; Arnold, D. W.; Bradforth, S. E.; Neumark, D. M., Examination of the  ${}^2A'_2$  and  ${}^2E'$  states of  $NO_3$  by ultraviolet photoelectron spectroscopy of  $NO_3^-$ . *J. Chem. Phys.* **1991**, *94*, 1740.
138. Wu, H.; Desai, S. R.; Wang, L.-S., Chemical Bonding between Cu and Oxygen – Copper Oxides vs  $O_2$  Complexes: A Study of  $CuO_x$  ( $x = 0-6$ ) Species by Anion Photoelectron Spectroscopy. *J. Phys. Chem. A* **1997**, *101*, 2103.
139. Mahé, L.; Boughdiri, S. F.; Barthelat, J.-C., Electronic Structures and Energetics in the  $CuX$  and  $Cu_2X$  Series ( $X = O, S, Se, Te, Po$ ). *J. Phys. Chem. A* **1997**, *101*, 4224.
140. Madhavan, P. V.; Newton, M. D., Electronic states of  $CuO$ . *J. Chem. Phys.* **1985**, *83*, 2337.
141. Bagus, P. S.; Nelin, C. J.; Bauschlicher, C. W., On the low-lying states of  $CuO$ . *J. Chem. Phys.* **1983**, *79*, 2975.
142. Igel, G.; Wedig, U.; Dolg, M.; Fuentealba, P.; Preuss, H.; Stoll, H.; Frey, R., Cu and Ag as one-valence-electron atoms: Pseudopotential CI results for  $CuO$  and  $AgO$ . *J. Chem. Phys.* **1984**, *81*, 2737.
143. Hippe, D.; Peyerimhoff, S. D., Theoretical spectroscopy of copper monoxide. *Molecular Physics* **1992**, *76*, 293.
144. Wu, H.; Desai, S. R.; Wang, L. S., Two isomers of  $CuO_2$ : The  $Cu(O_2)$  complex and the copper dioxide. *J. Chem. Phys.* **1995**, *103*, 4363.
145. Steimle, T. C.; Azuma, Y., An intermodulated fluorescence study of the  $A^2\Sigma^- - X^2\Pi_i$  band system of copper monoxide. *J. Mol. Spectrosc.* **1986**, *118*, 237.
146. Langhoff, S. R.; Bauschlicher Jr, C. W., Theoretical study of the  $X^2\Pi$  and  $A^2\Sigma^+$  states of  $CuO$  and  $CuS$ . *Chem. Phys. Lett.* **1986**, *124*, 241.

147. Polak, M. L.; Gilles, M. K.; Ho, J.; Lineberger, W. C., Photoelectron spectroscopy of  $\text{CuO}^-$ . *J. Phys. Chem.* **1991**, *95*, 3460.
148. Schultz, N. E.; Zhao, Y.; Truhlar, D. G., Density Functionals for Inorganometallic and Organometallic Chemistry. *J. Phys. Chem. A* **2005**, *109*, 11127.
149. Niu, S.; Huang, D.-L.; Dau, P. D.; Liu, H.-T.; Wang, L.-S.; Ichiye, T., Assessment of Quantum Mechanical Methods for Copper and Iron Complexes by Photoelectron Spectroscopy. *J. Chem. Theor. Comput.* **2014**, *10*, 1283.